

THE SPUTTERING OF HIGH ENERGY PARTICLES



By

STEVEN DZIOBA, B.Sc.

A Thesis

Submitted to the School of Graduate Studies
in Partial Fulfilment of the Requirements

for the Degree

Doctor of Philosophy

McMaster University

February 1980

DOCTOR of PHILOSOPHY (1980)
(Materials Science)

MCMASTER UNIVERSITY
Hamilton, Ontario
Canada

TITLE: The Sputtering of High Energy Particles

AUTHOR: Steven Dzioba, B.Sc. (McMaster University)

SUPERVISOR: Professor R. Kelly

NUMBER OF PAGES: xii, 140

ABSTRACT

The sputtering of high velocity particles is investigated through analysis by secondary photon emission. During a sputtering event a fraction of the particles emitted from the target are in varying degrees of excitation. These excited states have a finite probability of radiatively decaying back to the ground state. The emitted photon wavelength and intensity is recorded. In addition, the monochromator can be locked onto one particular wavelength and its intensity observed as a function of distance from the target surface. Such intensity distributions are measured for several group IA and IIA metals and fluorides. Their spatial extent, for the most part, is shown to be governed by the atomic transition probability of the excited state under observation.

A model is developed to describe the intensity distribution based on the premise that the sputtered particles are distributed in energy and we further propose that excitation in a sputtering event is a threshold process. From the experimental intensity distributions this proposed threshold energy is deduced and is found to be $10^1 - 10^3$ eV. These relatively high kinetic energies, along with the large sizes of excited states, indicate that their creation involves large energy transfers at or very near the surface. Such events as recoil sputtering may lead to the production of excited states.

To this end, calculations on recoil sputtering yields and mean energies are reported which justify the observed high energies

and low yields. Further, a comparison, based upon fractional yields, of recoil sputtered atoms and high energy cascade sputtered atoms show that the recoil source provides a larger number of high energy atoms available for excitation. Results relating to recoil implantation yields are also presented. In addition, recoil phenomena is used to explain some preferential effects observed in sputtering and transient effects in secondary photon emission.

Finally, the fate of the implanted primary ion is discussed with emphasis on its diffusion behavior in both damaged and undamaged ambient surroundings.

ACKNOWLEDGEMENTS

The kid from Barton Street does good - "with a little help from my friends".

This written document, the experimentation and theory is dedicated to my father who struggled, sweated and died trying. No ones efforts and support could possibly match his unfailing confidence in this author.

To Dr. Kelly, mien fürher, I acknowledge the opportunity he has given me to do research. His guidance has been an inspiration. His fortitude remarkable. His moral character as abominable as mine! My sincerest thanks to Roger. Sp

To Dr. J.D. Embury, who knew all too well why this work was undertaken and whose personal help will never be forgotten, thank you.

To Dr. J.S. Kirkaldy, my nemesis, who kicked me in the rear when I needed it and who pointed out that the world is often a lie; I raise my glass in gratitude.

To C.A. Sergnese, who stuck through it all, my warmest and grateful thanks.

To K. da Silva, whose remarkable typing skills brought this thesis to its conclusion, I am indebted.

Thanks are also due to the Department of Metallurgy and Materials Science for financial support, the Phoenix Pub for social support and a special acknowledgement to my lab mates - Jean, Krishna

and Mahamoud.

Finally, this work was supported through grants from the
National Research Council to Dr. R. Kelly.

TABLE OF CONTENTS

	PAGE
CHAPTER 1. INTRODUCTION	1
REFERENCES	11
CHAPTER 2. DETECTION AND ANALYSIS OF HIGH-ENERGY SPUTTERED SPECIES	12
2.1 INTRODUCTION AND BACKGROUND	12
2.1.1 Sputtering	12
2.1.2 Origins of Secondary Photons	16
2.2 EXPERIMENTAL	19
2.2.1 The Accelerator Chamber	19
2.2.2 Typical Spectra	21
2.2.3 Intensity Distributions	32
2.3 ANALYSIS AND DISCUSSION OF INTENSITY DISTRIBUTIONS	38
2.3.1 Intensity Distribution Functions	38
2.3.2 Discussion	51
2.4 CONCLUSIONS	67
APPENDIX 2.1	68
APPENDIX 2.2	69
REFERENCES	73
CHAPTER 3. THE THEORY OF RECOIL IMPLANTATION AND SPUTTERING	75
3.1 INTRODUCTION	75
3.2 THE FIRST GENERATION PROBLEM	77
3.3 THE SECOND GENERATION PROBLEM	85
3.3.1 Recoil Distribution Functions - Thin Sources	85

	PAGE
3.3.2 Recoil Distribution Functions - Moderately Thick Sources	91
3.3.3 Recoil Sputtered Energies	94
3.4 CONCLUSIONS	99
REFERENCES	100
CHAPTER 4. APPLICATIONS OF RECOIL IMPLANTATION AND SPUTTERING	101
4.1 INTRODUCTION	101
4.2 RECOIL SPUTTERING	101
4.3 RECOIL IMPLANTATION	108
4.4 PREFERENTIAL EFFECTS	111
4.5 CONCLUSIONS	113
REFERENCES	116
CHAPTER 5. FATE OF THE PRIMARY ION	117
5.1 INTRODUCTION	117
5.2 DIFFUSION PROFILES	118
5.3 CUMULATIVE RELEASE	124
5.4 CONCLUSIONS	133
REFERENCES	136
CHAPTER 6. OVERVIEW	137

LIST OF ILLUSTRATIONS

FIGURE NO.	CAPTION	PAGE
1.1	Schematic illustration of secondary-photon emission. The decay of the excited sputtered atom, B^* is by way of radiating a photon, $h\nu$.	3
1.2	Recoil phenomena during ion impact.	5
1.3	The photon response to the presence of oxygen during bombardment of Al.	7
1.4	Recoil implantation effects of Mo into various targets.	9
2.1	The sputtering process as defined through a time sequence.	13
2.2	Potential-energy curves for a Li-Li collision showing several curve crossing points.	17
2.3	Schematic of collision chamber showing the target and differentiating slit along with a point source used to align the latter with the target surface.	20
2.4	Relative system efficiency curve used in photon detection.	22
2.5	Grotrian Diagram for Li.	24
2.6a,b,c	Extracted electronic transitions resulting from bombardment of Li.	26,27 28
2.7	Semi-logarithmic plot of photon intensity versus principal quantum number n , for several LiI transitions.	29
2.8	Vibrational transition of the BH molecule.	31
2.9	Photon signal from Be in the pure state and an oxidized alloy.	33
2.10	As obtained photon intensity distribution from BeI.	35

		PAGE
2.11a,b	Photon intensity distribution from LiI for three transitions.	36,37
2.12	Electronic transitions involved in photon emission.	39
2.13	Calculated intensity distribution functions in differential form for four cases for P(E).	49
2.14	Schematic illustrations for the four cases for finding an atom in an excited state given it has kinetic energy E.	50
2.15	Linearization plots for some LiI transitions.	52
2.16	As in 2.15 except for some NaI transitions.	53
2.17	Intensity distribution for several sputtered excited ions.	59
2.18	Linearization plot for Mg transitions showing a cascade effect for the MgI 383.5 nm line.	64
2.19	Grotrian diagram for Mg.	65
2.20	Intensity distributions for Mg illustrating the effect of the decay rate constant.	66
A.2.1	Internal and external energy balance.	71
3.1	Power law approximations to the screening function.	79
3.2	Schematic representation of ion implantation, defined in this work as the first generation problem.	81
3.3	Schematic representation of recoil implantation, defined in this work as the second generation problem. Also shown are the statistical variables.	86
3.4	Recoil implantation integral evaluated by computer for $m_{12} = m_{23} = 1/3$ as given by eq. 3.18b.	92
3.5	Recoil sputtering integral as given by eq. 3.19b.	93
3.6	Recoil implantation integral as given by eq. 3.20b.	95
3.7	Recoil sputtering integral as given by eq. 3.21b.	96

	PAGE
4.1 Recoil sputtering yields of oxygen from aluminum.	102
4.2 Computer simulation of the energy spectra of sputtered atoms.	107
4.3 Recoil implantation distribution of oxygen in tungsten for three ion energies.	109
4.4 The effect of ion mass on the recoil implantation distribution of oxygen in tungsten.	110
4.5 Transient secondary ion yields from SiO ₂ .	112
5.1 Experimental profiles of 30 keV Kr in V compared to the predicted distribution.	119
5.2 Integral diffusion profiles of Kr in V.	121
5.3 Solution to the diffusion equation.	123
5.4 The effect of damage removal on the diffusion behavior of Kr in V.	125
5.5 The effect of damage removal on the cumulative release of implanted Kr.	126
5.6 Activation energy versus temperature at which maximum release rate occurs.	129
5.7 Release rate spectrum from Al.	130
5.8 Release rate spectrum from V.	131
5.9 Effect of prior annealing on the release rate spectrum.	134

LIST OF TABLES

TABLE NO.	CAPTION	PAGE
2.1	Observed LiI transitions as a result of 12 keV Kr ⁺ bombardment.	25
2.2	Sputtered excited atoms from Li and Na.	55
2.3	Transitions, decay rate constants for Group IIA fluorides.	57
2.4	Characteristic energies for Group IIA fluorides.	58
2.5	Previous measurements of energies of secondary ions.	61
3.1	Coefficients $A_{(1)} \ln$ for $m = 1/3$ for various mass ratios for range calculations.	82
3.2	Coefficients $A_{(1)} \ln$ for $m = 1/3$ for various mass ratios for deposited energy calculations.	83
3.3	Summation coefficients f_{23} , g_{23} and h_{23} as defined through eq. 3.6 for range and deposited energy.	88
3.4	Recoil sputtering integral $I_s^{(2A)}(0, M_3/M_2)$ for $m = 1/3$.	98
4.1	Thick source recoil integrals evaluated at the surface for $m = 1/3$.	104
4.2	Calculated recoil sputtered energies for 12 keV Kr ⁺ bombardments.	105
4.3	Numerical examples of recoil implantation and sputtering.	114
5.1	Activation energy data for pure metals.	132

CHAPTER 1

INTRODUCTION

The advent of "particle" accelerators, coupled with high and ultrahigh vacuum science, has given birth to a whole host of techniques involving particle-surface interactions which are now routinely used in fields varying from integrated circuit technology to surface analytical chemistry. Indeed, the field of surface science is plagued by the fact that, whereas God can be presumed to have made bulk solids, only the devil could have created surfaces. However, with the new tools available, surface scientists are making some headway, though it is often true that there are perhaps as many models for a particular effect as there are researchers. The wide and varied opinions concerning particle-surface interactions is even more acute in the investigation of inelastic particle-surface effects. This specialized branch is the youngest of the whole field, the first meeting of researchers being held at the Bell Laboratories in 1976 (1) followed by a workshop at McMaster University in 1978 (2). This relative youth, of course, means that new frontiers are being explored but with a good deal of stumbling along the way.

It is the purpose of this thesis to explore a particular inelastic effect: secondary photon emission, due to sputtered atoms which are electronically excited and subsequently radiate above a target surface. The work will be based in part on experiment and in part on theory.

We believe this investigation to be a "state of the art" study and, in the writer's opinion, to be the first work which rigorously models the distribution of light in front of a bombarded target from which information concerning the sputtered kinetic energies can be obtained. Further, we would suggest that the results obtained could constitute the basis for further investigations concerning sputtered excited particles.

Secondary-photon emission is the result of excited sputtered atoms which decay radiatively in the vacuum above a bombarded target. Since the volume from which these particles originate is on an atomic scale, these secondary photons can in principle give valuable information on the chemical composition of the extreme outer surface as illustrated in Fig. 1.1. For example, since the frequency of the emitted photon is characteristic of the atomic energy levels of the sputtered atom, it is possible to identify trace impurities on the surface to an estimated accuracy ranging from 1 ppm to 10^3 ppm (3), depending on the element. Though as yet not as quantitative as other techniques, White et al. (4) used SCANIIR (Surface Composition by Analysis of Neutral and Ion Impact Radiation) in chemical investigations of blood plasma and volcanic rock. Also, Braun et al. (5) have recently used secondary photon emission in depth profiling Al which was implanted into Ag and Shehata (6) has used a similar technique to profile anodic oxide films.

It will be shown that the kinetic energies of these sputtered excited atoms are relatively high, leading us to believe that their origins lie in collisions involving large energy transfers. In so far

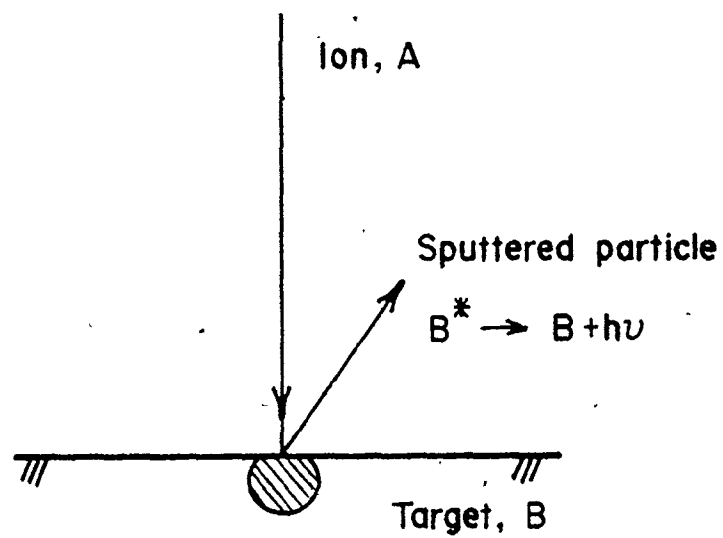


Figure 1.1 Schematic illustration of secondary-photon emission. The decay of the excited sputtered atom, B^* is by way of radiating a photon, $h\nu$.

as this is the case, we then develop a model for recoil sputtering. Unlike cascade sputtering, where energies are quite low (1-20 eV), recoil phenomena have been inferred to occur in several situations involving energetic particle-surface interactions.

Conventional collisional sputtering is based upon a cascade model (cf. section 2.1.1), however, we will develop (Chapter 3) a formalism for sputtering yields due to recoil effects and in addition estimate the sputtered particle energy through evaluation of the integral, $\int E d\phi$, which gives the average sputtered energy. Briefly put, the primary ion transfers an energy to a surface atom (recoil) which subsequently collides with other atoms and finally may escape the solid. This is illustrated in Fig. 1.2a. As we will show, whereas the yield of sputtered recoils is approximately 10% of the cascade yield, their average energies are relatively high, namely, much greater than the surface binding energy. We will propose that a possible, though by no means unique, reason for the sputtered excited atoms having high velocities is that they are formed by recoil sputtering rather than cascade sputtering.

Having introduced recoil sputtering, it is natural to use the same formalism to discuss recoil implantation. This has practical applications not only to secondary photon emission but to doping processes in general.

The relation of recoil implantation to secondary photon emission is illustrated in Fig. 1.3. Here Kelly and Kerkdijk (7) have monitored the photon signal from pure Al under various background pressures of oxygen. Their work shows long time transients in the photon

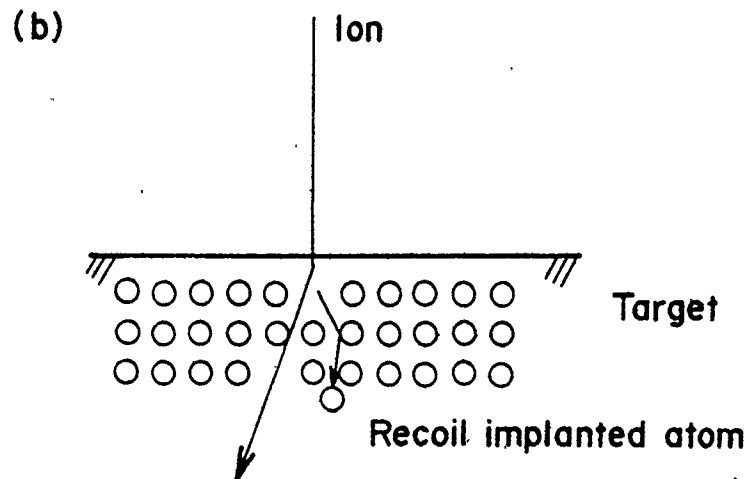
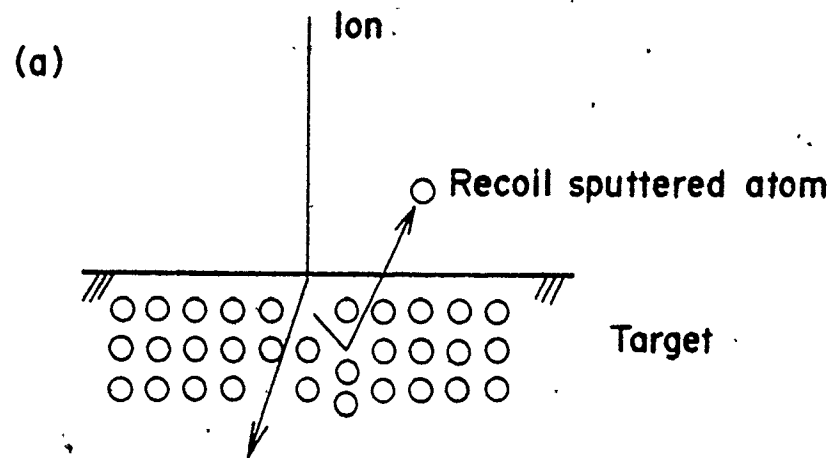


Figure 1.2 Recoil phenomena during ion impact.

signals as if oxygen were being recoil implanted into the target.

The relation to doping in general is based on the fact that the Silicon industries have boomed as a result of the ability to dope Si with various impurities in order to alter its electrical behavior. Early doping methods involved diffusing the species into Si at high temperatures. However, the high temperature in principle facilitates diffusion of undesired impurities as well as diffusion along dislocations, rendering the process not fully effective. Alternatively, as demonstrated by for instance, Seidel (8), one could ion implant B into Si, thus avoiding the high temperature problems. This method, in addition, gives a wider and more flexible range of depths to which the dopant can be introduced simply through the variation of the ion energy, and gives a wider choice of concentrations since thermodynamics need not be obeyed. The drawback to such a process lies in the fact that, especially for heavy ions, a good deal of radiation damage is introduced. This damage can take the form of point defects (9), dislocation loops (10), voids (11) or even total disorder, i.e., amorphization. The removal of these defects can be obtained through thermal annealing (12) or, more recently through laser annealing (13). Temperatures of the order of 700°C are required, thus substantially below those for diffusion.

As an alternative to direct implantation, it will be shown in this work that it is possible to recoil implant various dopants provided the dopant can be deposited on the substrate in thin film form. The process is shown in Fig. 1.2b. The primary ion, usually an inert gas, transfers energy to a struck recoil-source atom which subsequently

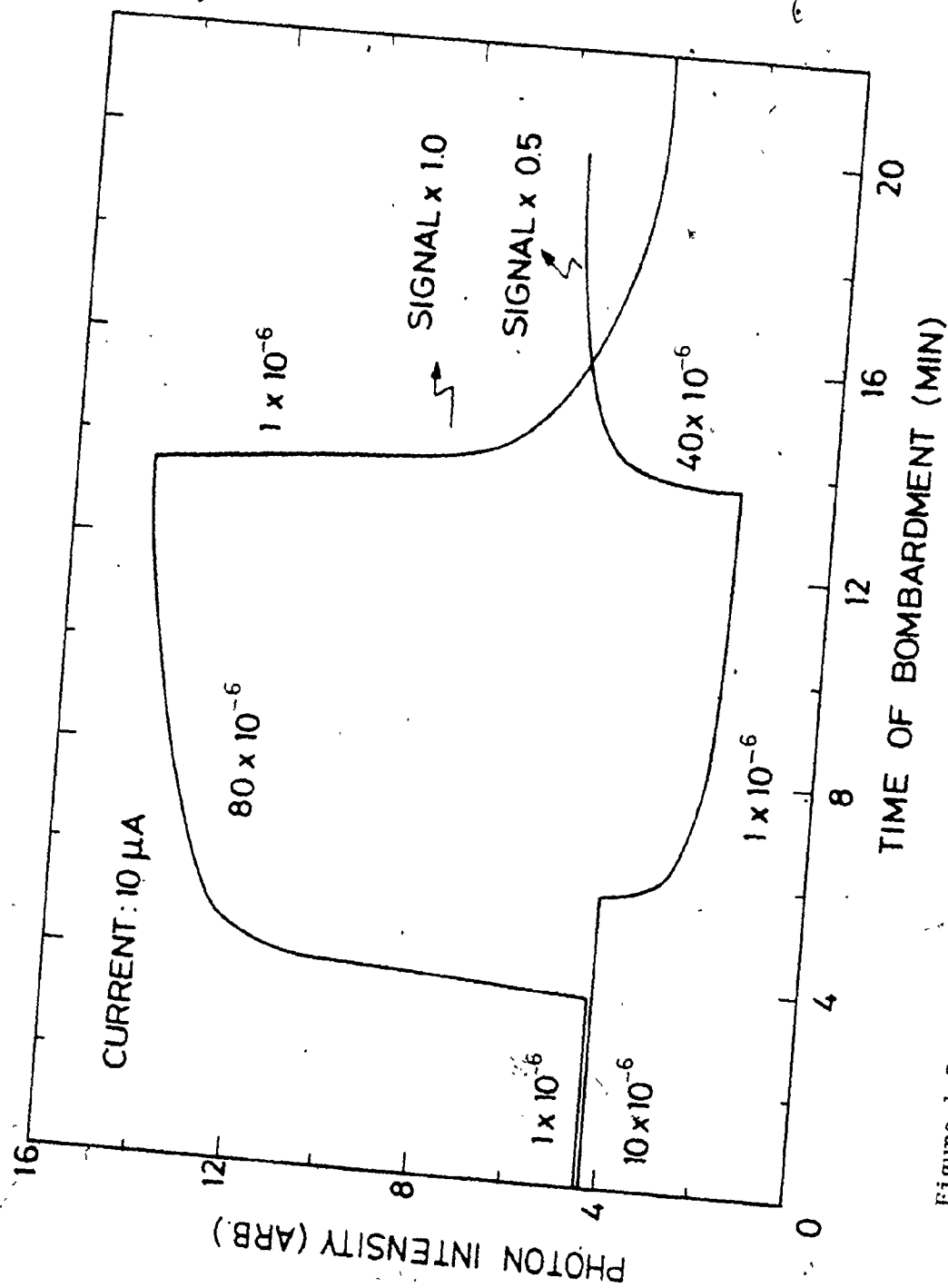


Figure 1.3 The photon response to the presence of oxygen during bombardment of Al. From ref. 7.

implants into the substrate. This process avoids the use of complicated ion sources and achieves a monotonically decreasing dopant distribution lying very close to the surface. Our contribution to this subject will be mainly to develop analytical expressions and computer solutions for implantation profiles from thin and moderately thick sources. This effect along with its corollary is discussed at length in Chapters 3 and 4 namely, recoil sputtering.

A further realm of application of the ideas of recoil sputtering and implantation is to surface analysis. These processes may play a role in altering the surface composition of bombarded compound targets. For example, it is known that an initial alloy, $\text{Ag}_{0.75}\text{Au}_{0.25}$ changes to $\text{Ag}_{0.54}\text{Au}_{0.45}$ after high dose bombardment with Ar ions. That is, an enrichment of the heavier component has occurred. We will show that this effect may, in part, relate to recoil sputtering, where the lighter component is preferentially sputtered.

As further evidence for recoil effects, Tarn and Wehner (14) have deposited Mo films on various targets, as reproduced in Fig. 1.4. They found that Mo on an Al target was removed only very slowly when the system was bombarded with 200 eV Ar^+ whereas Mo on W was easily removed. We tentatively interpret this effect as being due to recoil effects which are mass dependent. It should be pointed out that, if there exists a mass correlation in recoil effects, then caution must be taken in interpreting data from surface analytical techniques such as Auger Electron Spectroscopy, which employs a heavy inert-gas ion beam to sputter the surface.

However, effects of surface alteration during ion bombardment,

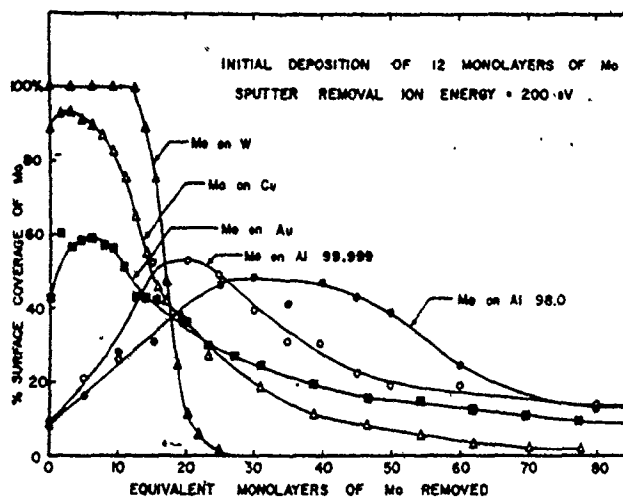


Figure 1.4 Recoil implantation effects
of Mo into various targets.
From ref. 14.

in principle, may have many origins, among them surface binding energy effects, chemical effects, abundance effects and diffusion effects. It is not the purpose of this work to test or evaluate these models but rather simply to add to this list a mass-dependent effect.

Finally, we discuss, in Chapter 5, the fate of the primary ion as effected by thermal annealing. This study, through diffusion techniques, illustrates the effect of radiation damage on the implanted species. This is of importance in reactor fuel claddings or first wall materials in proposed fusion devices where a portion of the nuclear reactants are inert gases. For instance, the release of gas from the first wall in fusion containers is expected to cool the plasma, thus decreasing the fusion efficiency. We have employed isochronal anneals along with release rate experimentation to investigate the diffusive behavior of implanted ions with the result that there is a biased outward motion of the ions in the presence of a damaged region. Removal of this damaged zone, returns the diffusion behavior to a normal process.

REFERENCES TO CHAPTER 1

1. Inelastic Ion-Surface Collisions, ed., N.H. Tolk, J.C. Tully, W. Heiland and C.W. White, Academic Press, New York, 1977.
2. Workshop on Inelastic Ion-Surface Collisions, Surface Sci., 90 (1979), ed. R. Kelly.
3. I.S.T. Tsong and N.A. Yusuf, Appl. Phys. Lett., 33 (1978) 999.
4. C.W. White, D.L. Simms and N.H. Tolk, Science, 177 (1972) 481.
5. M. Braun, B. Emmoth and R. Buchta, Rad. Effects, 28 (1976) 77.
6. M.T. Shehata and R. Kelly, J. Elec. Soc., 122 (1975) 1359.
7. R. Kelly and C.B. Kerkdijk, Surface Sci., 46 (1974) 537.
8. T.W. Seidel, in Second International Conference on Ion Implantation in Semiconductors, eds., I. Ruge and J. Graul, Springer-Verlag, New York, 1971.
9. D. Edwards and E.V. Kornelson, Rad. Effects, 26 (1975) 155.
10. M.K. Hossain and L.M. Brown, Rad. Effects, 31 (1977) 203.
11. C. Cawthorne and E.J. Fulton, Nature, 216 (1967) 575.
12. D.J. Welford, R.E. Anderson and B.G. Streetman, J. Appl. Phys., 48 (1977) 2442.
13. G.K. Cellar, J.M. Poate, G.A. Rozgonyi and T.T. Sheng, J. Appl. Phys., 50 (1979) 7264.
14. M.L. Tarng and G.K. Wehner, J. Appl. Phys., 43 (1972) 2268.

CHAPTER 2

2. DETECTION AND ANALYSIS OF HIGH-ENERGY SPUTTERED SPECIES

2.1 INTRODUCTION AND BACKGROUND

It has been experimentally well established that the deposition of energy from a primary accelerated particle, usually a heavy ion, gives rise to the expulsion of target atoms (1,2), a phenomena known as sputtering. In this chapter, focus is placed on the production of secondary photons resulting from that fraction of target atoms sputtered in an excited state. In particular, analysis is directed towards the kinetic energy of these excited sputtered atoms. In order to do justice to this process, a brief summary of the sputtering event will be given and a mention made as to possible mechanisms for the creation of an excited species during the sputtering event.

2.1.1 Sputtering

The sputtering phenomenon is most basically described as the ejection of target atoms as the result of a deposition of energy near the surface of a solid. Consider a primary accelerated ion which strikes a target, as schematically shown in Fig. 2.1. At energies of the order of a few keV most of the primary particles' energy is deposited in nuclear or elastic collisions (3), which gives rise to recoiling target atoms, for example, the atom labelled 2 in Fig. 2.1. These recoiling atoms then set up further recoils, for example, the

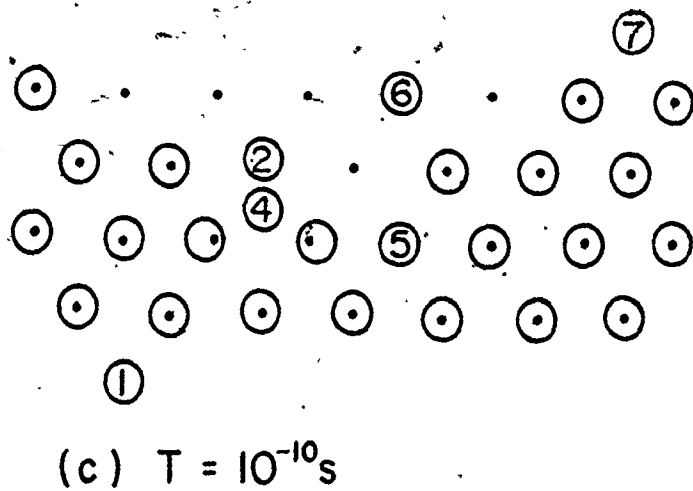
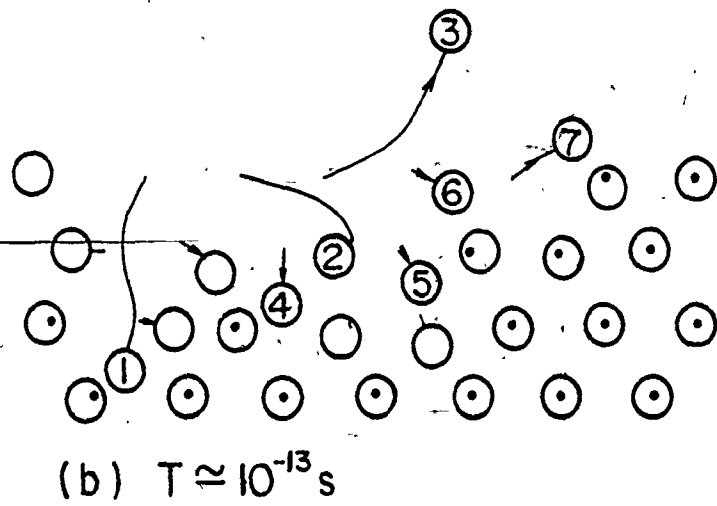
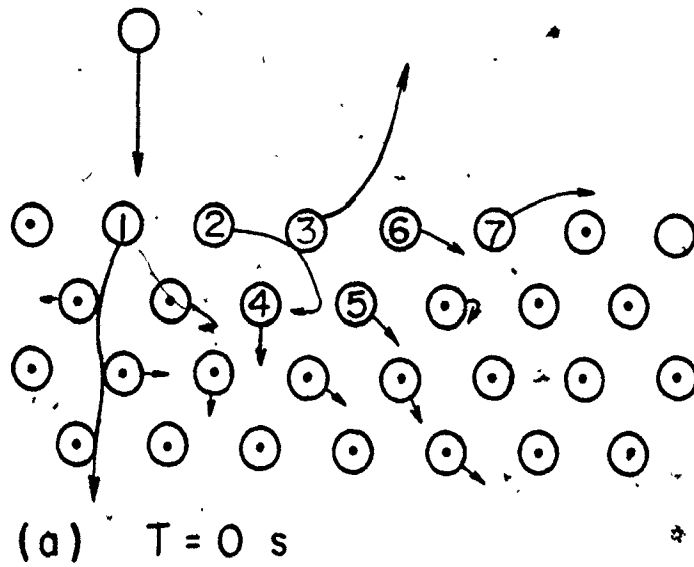


Figure 2.1. The sputtering process as defined through a time sequence.

atoms labelled 3, 4 and 5 until a rather large "collision cascade" is developed which intersects the surface. Should the target recoil atom reach or be created at the surface with energy exceeding the surface binding energy, E_b (of the order of 1-10 eV), it will be expelled from the solid. In other words, if the transport of energy from the cascade to the surface is greater than E_b then atoms are sputtered. This model of sputtering, due to collisions, has been quantitatively developed by Sigmund (4) though earlier treatments of this process date back to the late 1950's (5,6). According to Sigmund (4) the yield of sputtered atoms is given by

$$S \propto \frac{E_1 C_D(0)}{E_b} \text{ atoms/ion,} \quad (2.1)$$

where E_1 is the primary ion energy, E_b the surface binding energy and $C_D(0)$ the deposited energy at the surface, $x = 0$. Typical values of S range from 1 to 10 atoms per incident ion in the keV region (7). Of particular interest in Fig. 2.1 is the collision between the primary ion and atom labelled 1. In this special case, a large fraction of the primary energy is transferred, however, the momentum is directed into the solid leading to recoil implantation of the struck atom. Analogously, atom 3 undergoes a similar effect in the "backward" sense leading to recoil sputtering. The treatment of this special case will be extensively investigated in chapters 3 and 4.

A second model of sputtering concerns the thermal energy associated with the atoms in the solid after atomic motion has ceased, typically after 10^{-12} s, so called thermal sputtering. Developed

quantitatively by Kelly (8), this phenomenon is based on a hot zone such that atoms on the surface are vaporized due to an elevated temperature over a localized region. In addition to atom ejection, this hot zone may contribute to crystallization (or amorphization, depending upon the particular system) (9) and excitation or ionization via a Saha-type process (10).

One salient feature of sputtering apropos to this investigation, is the energy distribution of these sputtered atoms, $dN(E)/dE$. In the case of cascade sputtering, Thompson (11) has shown that this distribution can be given, in normalized form*, as

$$dN(E)/dE = \frac{2EE_b}{(E + E_b)^3}, \quad (2.2)$$

where E_b is the surface binding energy or a generalized planar surface potential barrier. It is often convenient to consider cases where $E \gg E_b$ and hence use a more analytically tractable form of equation 2, namely, $dN(E)/dE \propto E^{-2}$. In addition it should be pointed out that the maximum in this flux occurs at $\frac{1}{2}E_b$, typically 1-5 eV. Further, it is useful to use this value as a reference for distinguishing high-energy events ($E \gg E_b$) and low energy events ($E \leq E_b$).

For the case of thermal sputtering, it has been proposed that the sputtered energy distribution follows the form

* See Appendices 2.1 and 2.2 for details.

$$dN(E)/dE \propto E \exp(-E/kT) , \quad (2.3)$$

where T , the temperature of the sputtering zone, is a rapidly varying function of time. In this model the maximum in the distribution is much less than E_b . In any case, the total yield of sputtered atoms is of course the sum of collisional and thermal effects.

The total flux of ejected atoms is actually comprised of several species ranging from ground-state neutral atoms and ions to excited atoms, ions, and molecules (12,13), to extended clusters of atoms (14). Clusters from bombarded tungsten of the type W_n^+ with n up to 13 were confirmed by Staudenmeir (14). The interest in this work is on those atoms sputtered in excited states.

2.1.2 Origins of Secondary Photons

That fraction of sputtered atoms ejected in excited states has a finite probability of escaping the solid in an excited state and eventually decaying back to the ground state by emitting a photon characteristic of the electronic structure of the atom. This photon is called a secondary photon and, in the light of the previous section, two basic approaches to photon emission can be taken, namely, collisional and thermal.

For collisional sputtering, we expect atoms to undergo collisions whereby the internuclear separation deviates substantially from the equilibrium case. Figure 2.2 illustrates calculated interatomic potentials for two ground state Li atoms, $^1\Sigma_g^+$ or $^3\Sigma_u^+$. During a collision of two ground-state atoms, their relative kinetic energy is converted to potential energy as the two partners collide and travel up

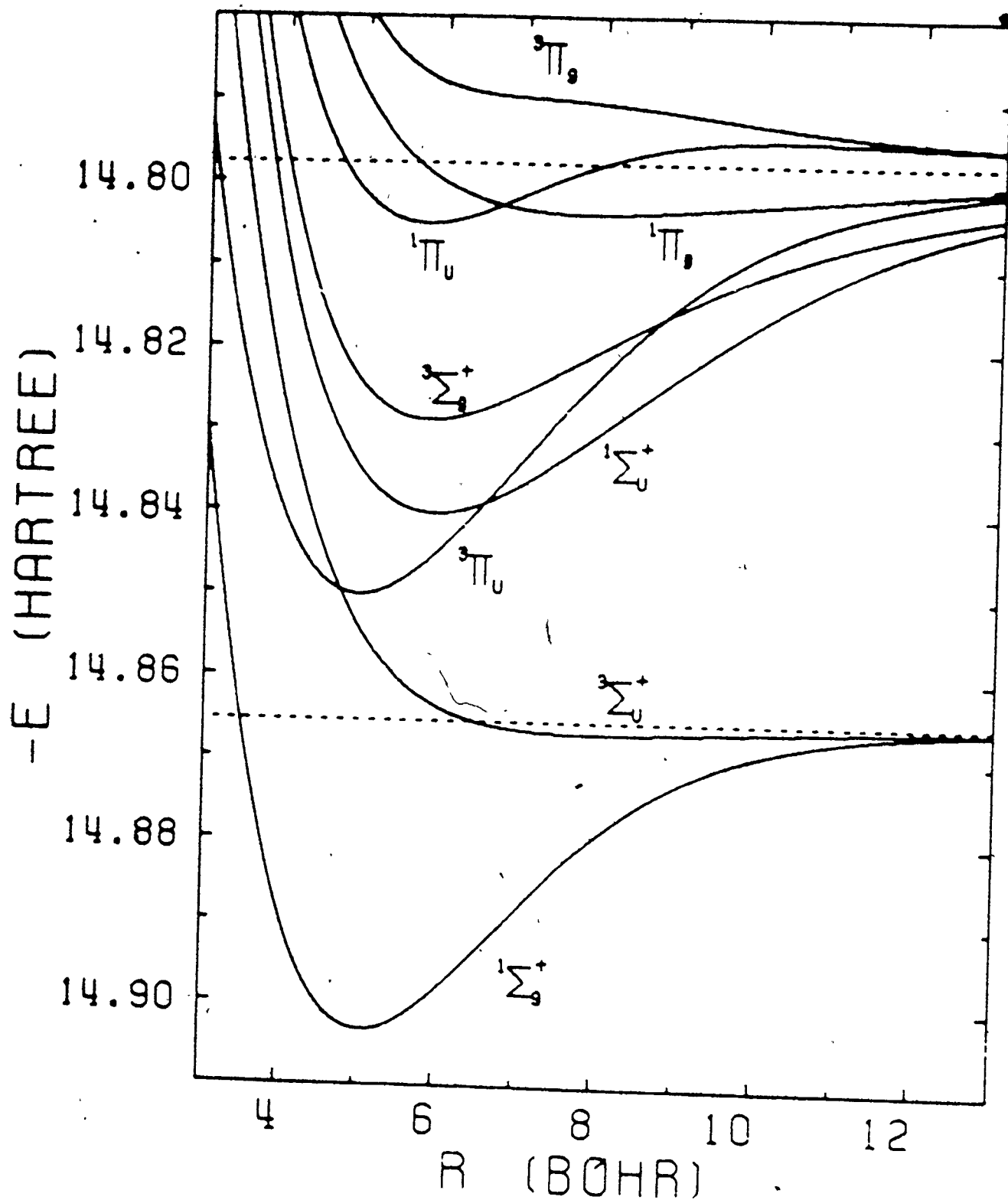


Figure 2.2. Potential-energy curves for a Li-Li collision showing several curve crossing points. From ref. 15.

the repulsive portion of the potential-energy curve, i.e., for distances less than the equilibrium separation, r_0 . They then reverse their direction and travel back down the well and eventually separate ($r \gg r_0$). If, for example, two Li atoms are in the ungerade state, $^3\Sigma_u^+$, their collision could lead to several different end products should they return along a different potential curve. This event takes place at a crossing between two potential curves. For instance, they may return on curves such that the end products (at $r \gg r_0$) are in excited states or even ionized. This picture of producing excited sputtered atoms is, however, somewhat over-simplified since collisions at or near the surface in a sputtering site involve many bodies. In addition, adsorbates, such as oxygen, are known to drastically effect the yield of secondary photons (16,17), a feature which may or may not be readily explained through such a curve-crossing mechanism. However, this picture does imply that the production of excited sputtered atoms is a threshold type process. That is, the colliding partners must travel to at least the first crossing point in the potential-energy diagram in order for excitation to occur. This threshold behavior will be discussed at length in a subsequent section.

Following the thermal model of sputtering, Andersen and Hinthorne (10) have proposed that a local thermodynamic equilibrium exists between a plasma and the bulk solid during the sputtering event. Consequently, there would exist an equilibrium number of atoms in an ionized state, governed by the temperature of such a plasma, according to a Boltzmann factor, $\exp(-E_i/kT)$, where E_i is the energy of the i^{th} excited level. Similarly, Good-Zamin et al. (18) have attempted to

apply the same formalism to excited states.

The decay of a sputtered excited atom as it leaves the solid takes place by two routes: non-radiative and radiative transitions. In the non-radiative cases, de-excitation occurs through resonant electron transfer back to the solid (i.e., tunneling) or else by Auger processes (19). The probability of an excited species surviving a non-radiative transition a perpendicular distance x from the surface is given by $\exp(-A/v_{\perp})$, where A is the transition rate for the particular electronic levels of interest and v_{\perp} , the sputtered atoms' perpendicular velocity. Should this be the case, then the excited species decays radiatively by emitting a photon in the vacuum above the target. This process is what is referred to as secondary-photon emission.

2.2 EXPERIMENTAL

2.2.1 The Accelerator Chamber

A monoenergetic beam of ions was normally incident upon targets as schematically shown in Fig. 2.3. Acceleration potentials of 3-20 keV could be obtained in a vacuum of approximately 10^{-6} torr (beam on) and with typical currents on the target of 0-20 μ A. The beam was mass analyzed with a Wien (cross-field) filter and could be focussed at three stages along the beam path (~ 1 m). Ion beams were not rastered.

The photon signal from sputtered excited species was analyzed by a Jarrel-Ash model 82-410 (0.25 m) monochromator through two slits. The first, located approximately 25 mm from the target centre, was 0.2 mm wide and facilitated the measurement of photon intensity

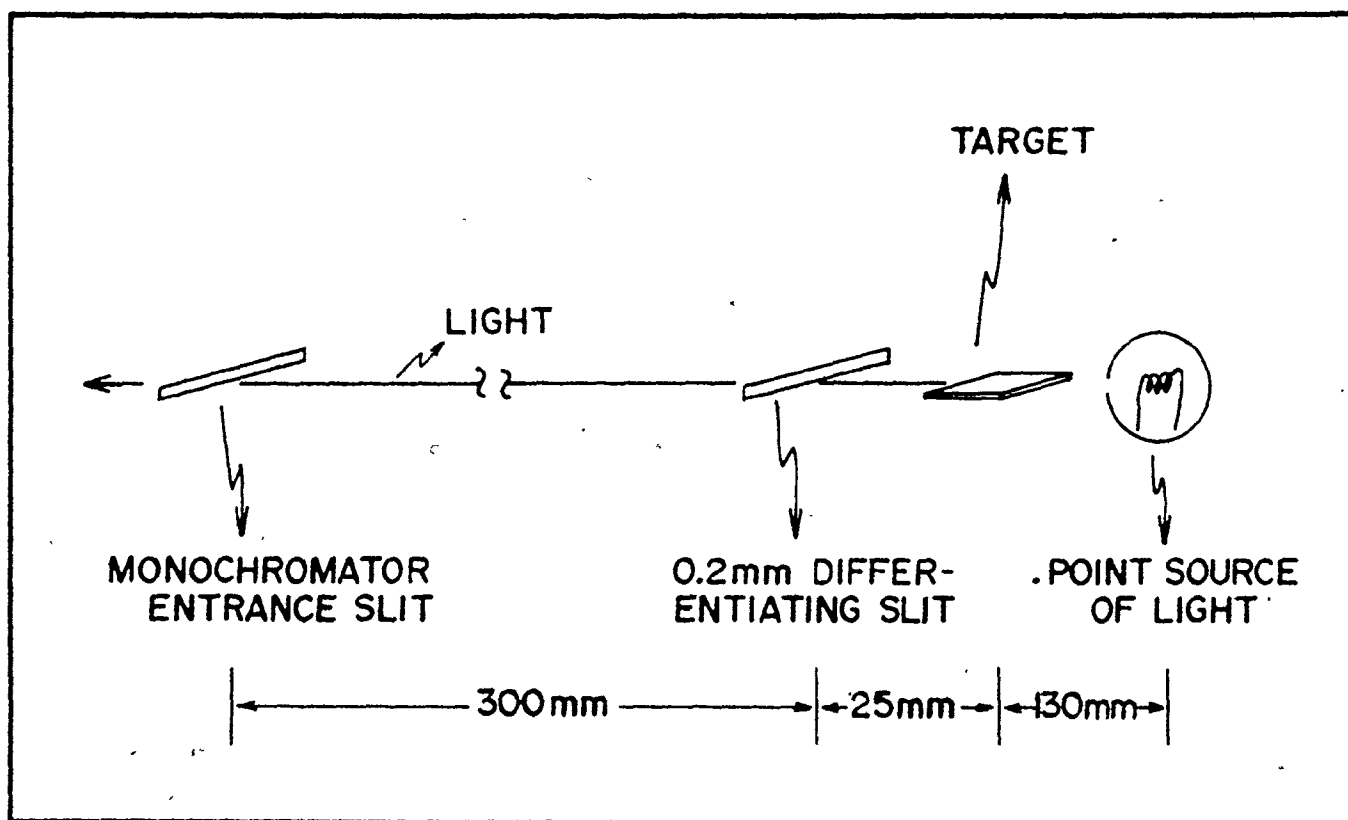


Figure 2.3. Schematic of collision chamber showing the target and differentiating slit along with a point source used to align the latter with the target surface.

distributions as a function of distance from the target surface. The second slit, 0.5 mm wide, was the entrance to the monochromator. The light was processed by an EMI 6256 QB photomultiplier tube housed at -30°C . Photon yields were then fed into a Princeton Applied Research model 1140 quantum photometer and finally displayed on a conventional strip-chart recorder.

The detection efficiency of the system was determined using a black-body source (Optronics model IR-13) and in relative units is shown in Fig. 2.4. Here, the efficiencies are seen to drop to zero for wavelengths above 650 nm and to be erratic below approximately 250 nm.

2.2.2 Typical Spectra

It has been well known that photon emission results from a variety of sputtered excited species, that is, atoms, ions, and molecules and from electronic, vibronic, and vibrational/rotational transitions. The experimentation for this study, however, was limited, for the most part, to electronic and vibronic transitions in the wavelength interval 250-650 nm.

As previously discussed, during sputtering one or more of the outer shell electrons can (even with very low probability) be promoted to a level greater than the ground state configuration. As the excited atom moves away from the target, the excited electron decays by emitting a photon of energy (and hence wavelength) appropriate to the difference between the initial and final levels. For example, the ground-state electronic configuration of Li is $1s^2 2s^1$ $^2S_{1/2}$ and the outer 2s valence

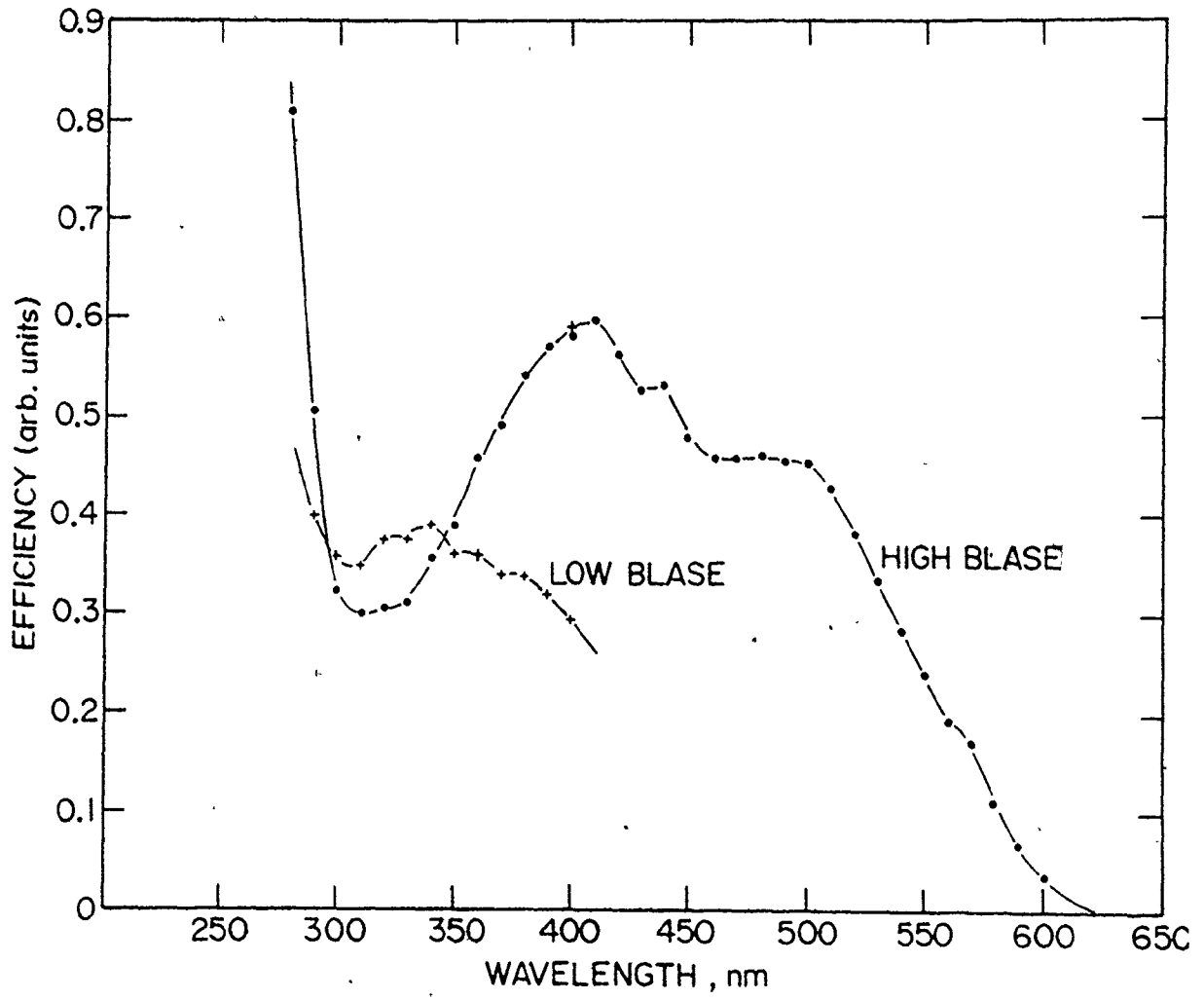


Figure 2.4. Relative system efficiency curve used in photon detection.

electron becomes the participant in electronic excitation and subsequent de-excitation. For instance, the transition of this outer electron from the 2p level back to the ground state is accompanied by a photon of wavelength 670.8 nm. Figure 2.5 gives an extensive summary of the energy levels (Grotrian Diagram) for Li along with the wavelengths of photons emitted upon de-excitation.

Experimentally, when 12 keV Kr^+ ions were incident upon, for example, a LiF target and the differentiating slit (cf. Fig. 2.3) was in a fixed position, then by scanning the monochromator over the wavelength region 250-650 nm results shown in Figs. 6a, b, and c were obtained. In this particular case three series were observed as listed in Table 2.1. The extracted spectra in general were well resolved, with excellent signal to noise ratio. When estimates of detection efficiencies can be made, as from Fig. 2.4, the intensity of a particular transition can be used to infer level population as indicated in Fig. 2.7. It can be seen that a semi-logarithmic plot of intensity versus principal quantum number, n , which scales as the energy of the upper level, gives a straight line indicating a Saha-type population distribution (10). Though such a relationship is observed, it is not self evident nor indicative that the production of excited sputtered atoms is thermal in origin. In fact the slope of such a plot as in Fig. 2.7 yields a temperature of the order of several thousand kelvins. In this context it is difficult to physically justify such a temperature. Notwithstanding such problems, a semi-log plot of this nature is often useful in simply categorizing data.

In addition, the final column of Table 2.1 gives the mean radius

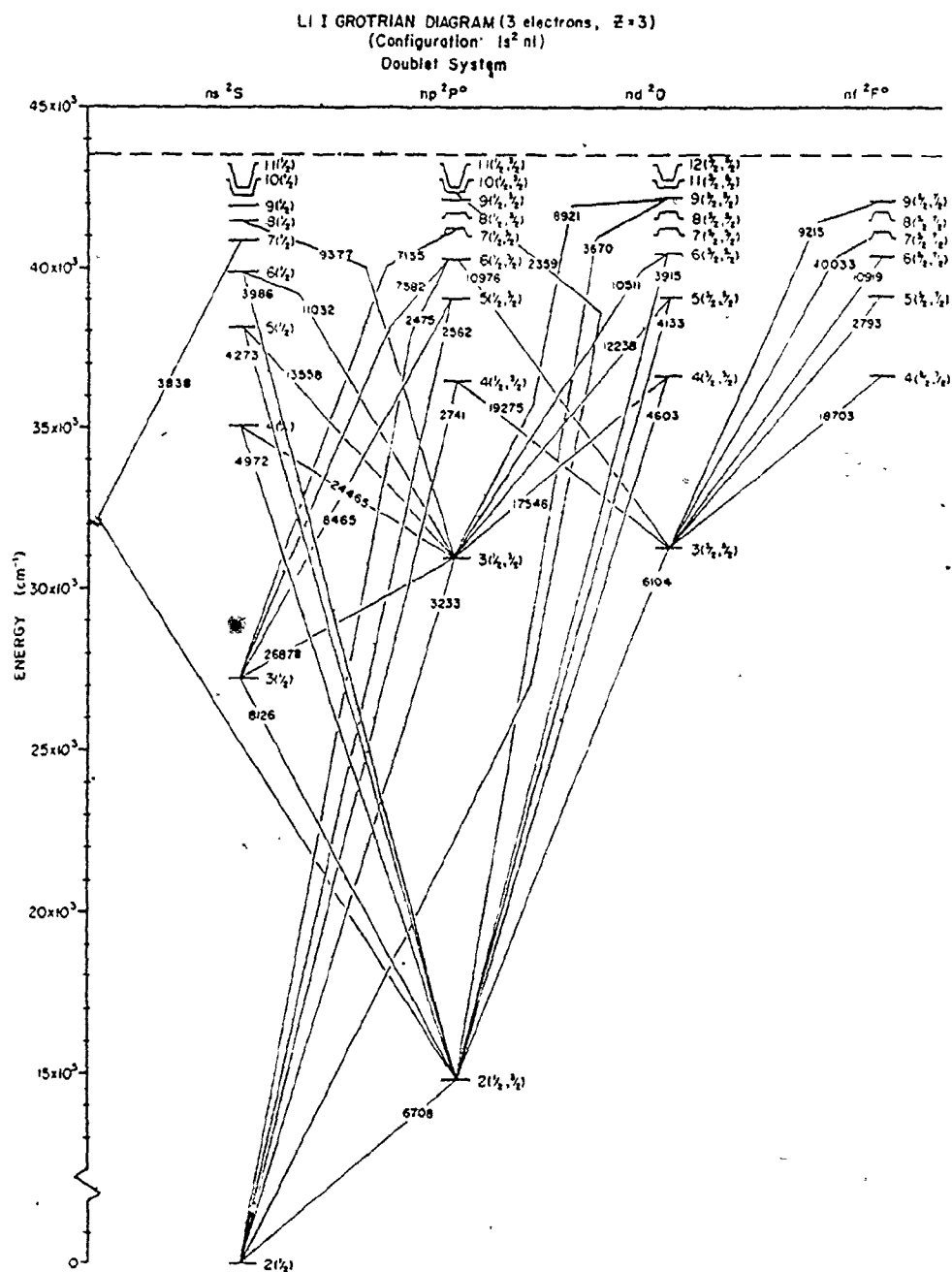


Figure 2.5. Grotrian Diagram for Li.

Table 2.1

Observed LiI transitions as a result of 12 keV Kr^+ bombardment.

Term	Transition	Wavelength, nm	$\langle r \rangle$, a_0
$2S - 2P$	$2s - 2p$	670.8	5.31
	$2s - 3p$	323.3	12.51
	$2s - 4p$	274.1	23.01
	$2s - 5p$	256.2	36.51
$2P - 2S$	$2p - 4s$	497.2	24.00
	$2p - 5s$	427.3	37.50
	$2p - 6s$	398.6	54.00
$2P - 2D$	$2p - 3d$	610.4	9.51
	$2p - 4d$	460.3	18.00
	$2p - 5d$	413.3	34.50

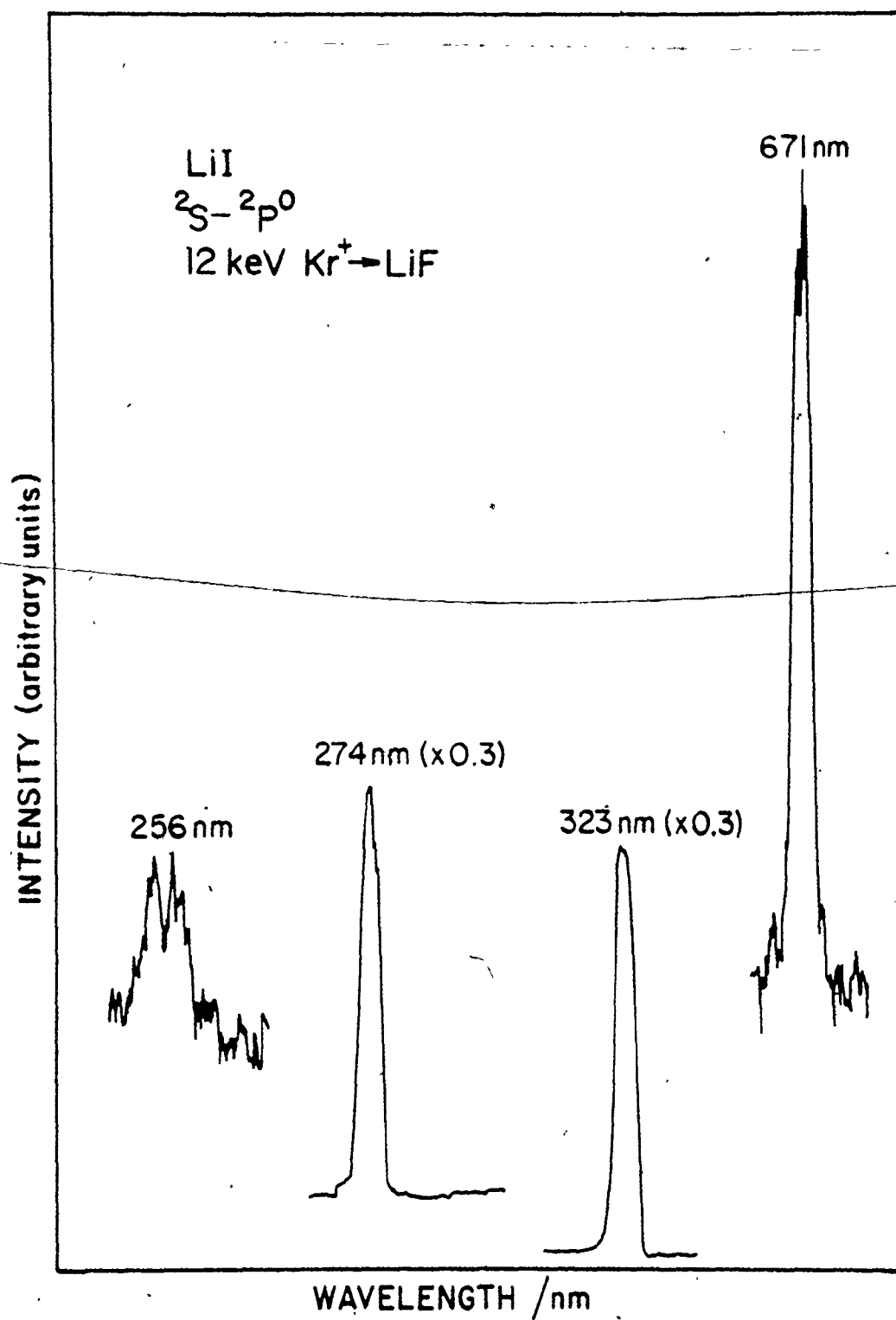


Figure 2.6a. Extracted electronic transitions resulting from bombardment of Li.

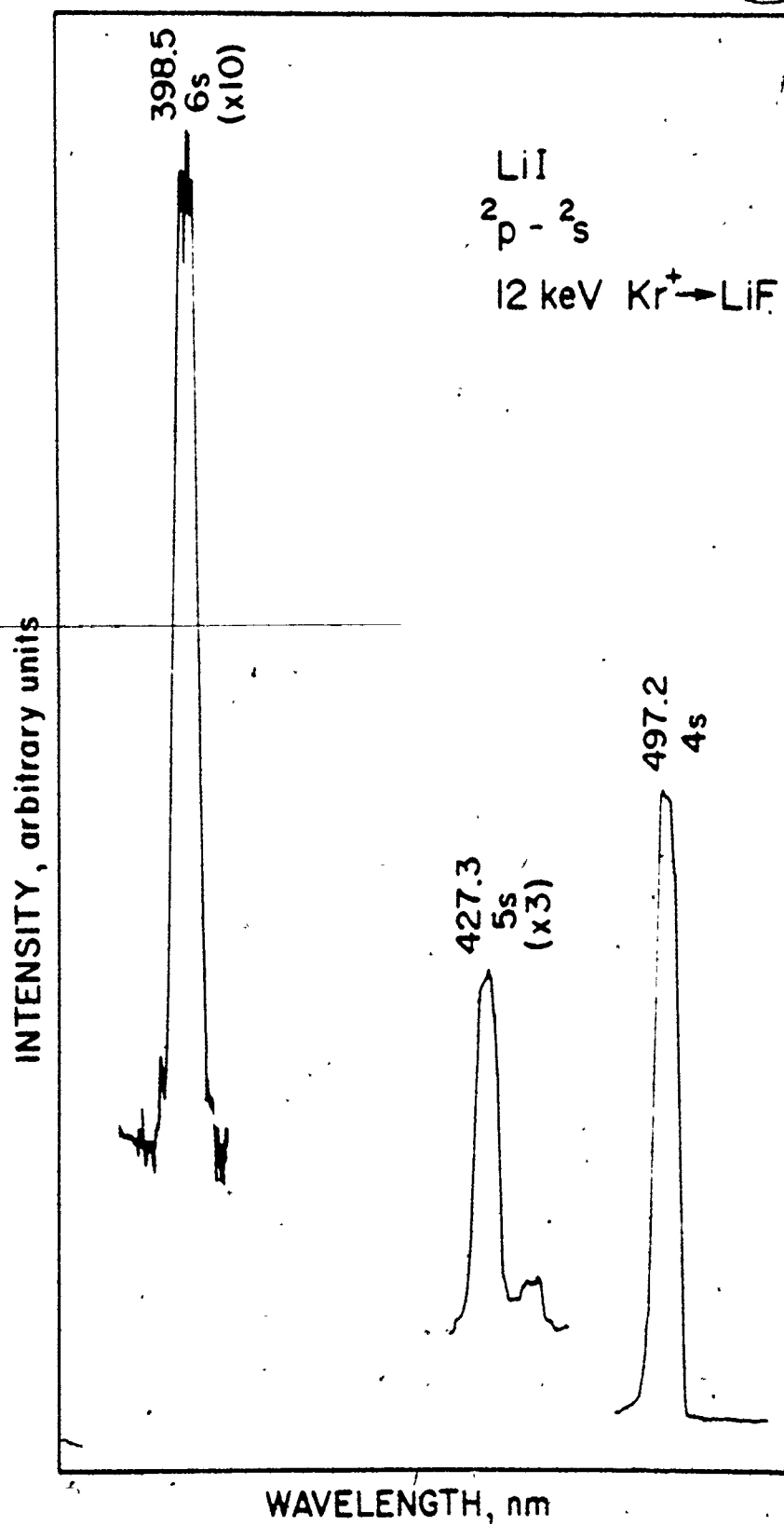
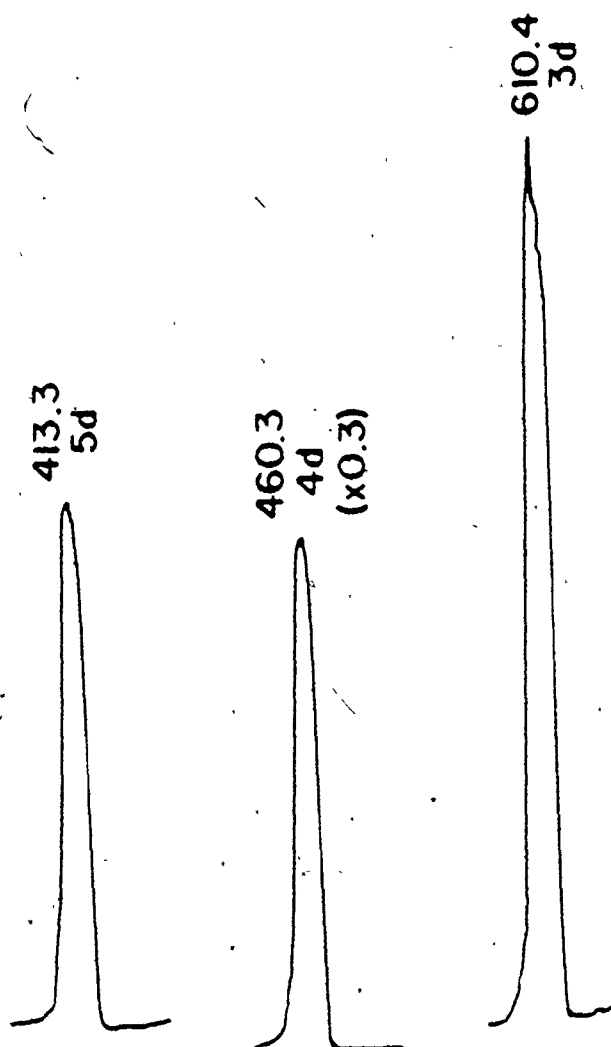


Figure 2.6b. Extracted electronic transitions resulting from bombardment of Li.

INTENSITY, arbitrary units

LiI
 $2p - 2D$
12 keV $Kr^+ \rightarrow LiF$



WAVELENGTH, nm

Figure 2.6c. Extracted electronic transitions resulting from bombardment of Li.

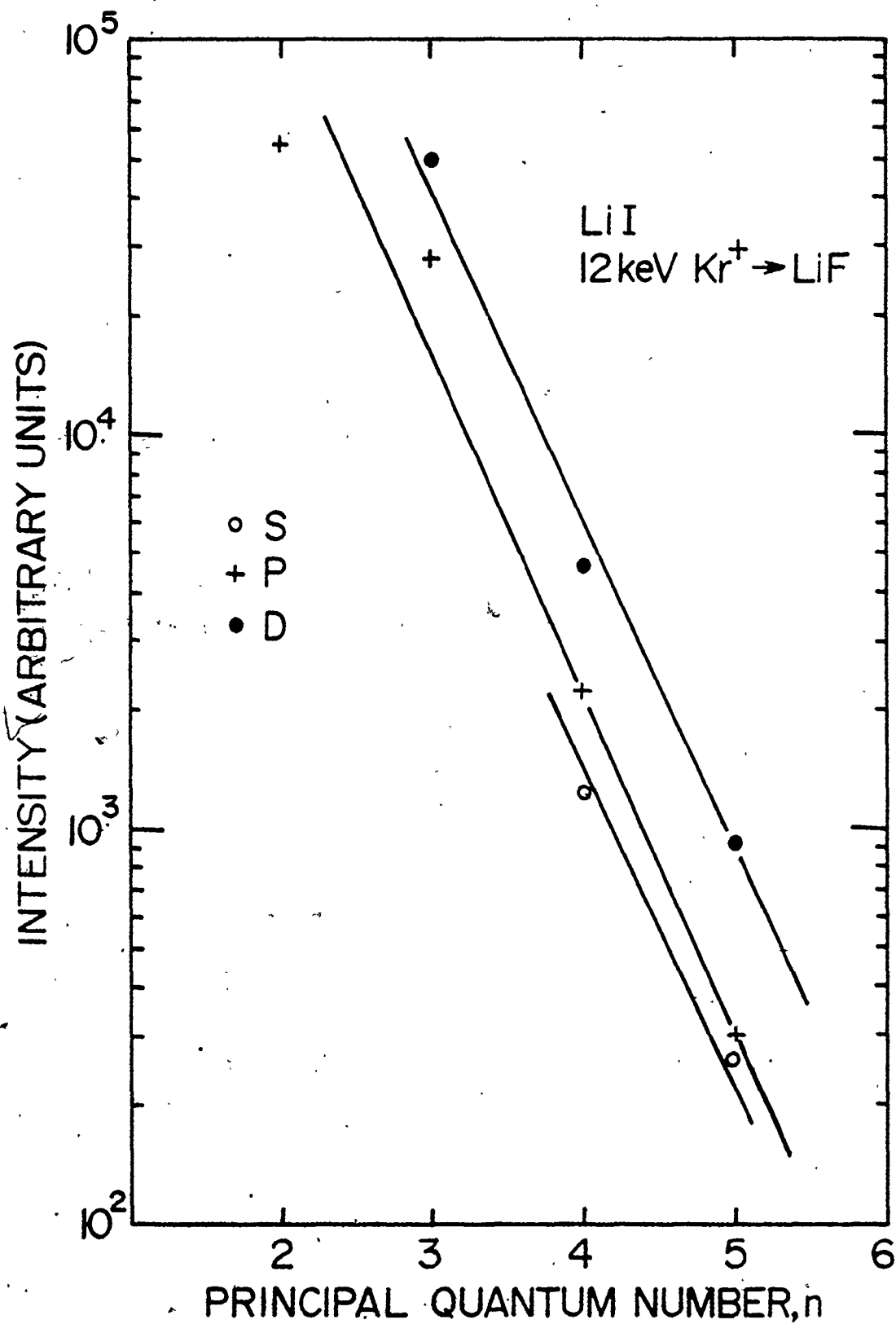


Figure 2.7. Semi-logarithmic plot of photon intensity versus principal quantum number n , for several Li I transitions.

of the Rydberg states for Li in units of the Bohr Radius $a_0 = 0.529 \text{ \AA}$, using the relation

$$\langle r \rangle = \frac{n^2 a_0}{Z} \left[1 + \frac{1}{2} \left(1 - \frac{\ell(\ell+1)}{n^2} \right) \right], \quad (2.4)$$

where n is the principal quantum number, ℓ the angular momentum quantum number and Z the effective atomic number (including screening by core electrons). When compared to atomic separation in solids, typically $4a_0$, it is doubtful that such large radii species could survive an excursion through the solid. Rather, it seems plausible that excited sputtered atoms are created in collisions involving very near surface atoms and hence the sputtered atom kinetic energies are expected to be greater than those energies that typify a sputtered atom from a collision cascade. Finally, it should be pointed out that the ion beam, due to its small areal density, does not participate in the excitation process. This has been verified by the observation of excited sputtered atoms in a transmission mode.

In addition to electronic spectra from single atoms, we have also observed molecular (vibronic) spectra as shown in Fig. 2.8 for the BH molecule. This spectrum corresponds to transitions to the ground state vibrational level $A^1\Pi$ from the first excited state $X^1\Sigma$ and is, in general, characterized by a continuum over a large range of wavelengths. However, this continuum, with improved resolving power, could be broken up to the individual vibrational/rotational transitions. In most experimental investigations of this sort, molecular transitions are for the most part seen as continua (17).

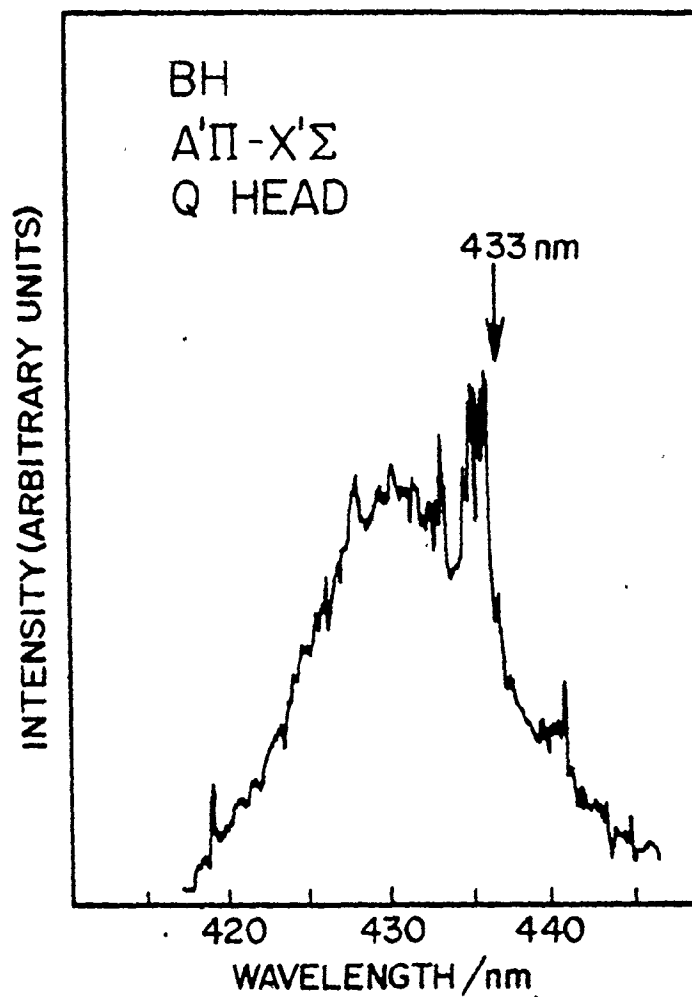


Figure 2.8. Vibrational transition of the BH molecule.

Finally, concerning the application of secondary photon emission in surface analysis, Fig. 2.9 shows the time - intensity plot for the BeI 332 nm transition in a pure Be target and in oxidized $\text{Ni}_{0.88}\text{Be}_{0.12}$ alloy. The intensity level from the pure sample serves as a reference. The intensity distribution in the oxidized alloy from BeI shows two important features with respect to surface analysis. Firstly, there is the enhancement of the BeI 332 nm signal as a result of the oxide. This effect may be interpreted as the presence of oxygen inhibiting non-radiative transitions (resonant or Auger de-excitation), thus increasing the probability of a radiative transition, i.e., photon emission. The final result is that we observe an increase in photon intensity with oxygen content. Secondly, as the Kr^+ sputters through the oxide film a steady state signal from BeI 332 nm of approximately 27% of the pure sample is achieved revealing an enhancement of about a factor of two when compared to pure Be.

This matrix effect is, at the present, not fully understood, though attempts at qualitatively justifying such an effect may lie in heteronuclear collisions leading to more excitation (i.e., more curve crossings) than homonuclear collisions. The details of such quantum mechanical calculations are, however, beyond the scope of this investigation.

2.2.3 Intensity Distributions

With reference to Fig. 2.3, with the differentiating slit fixed in one position, the target could be lowered in steps of 0.5 mm so that intensity distributions of a selected transition, as a function of

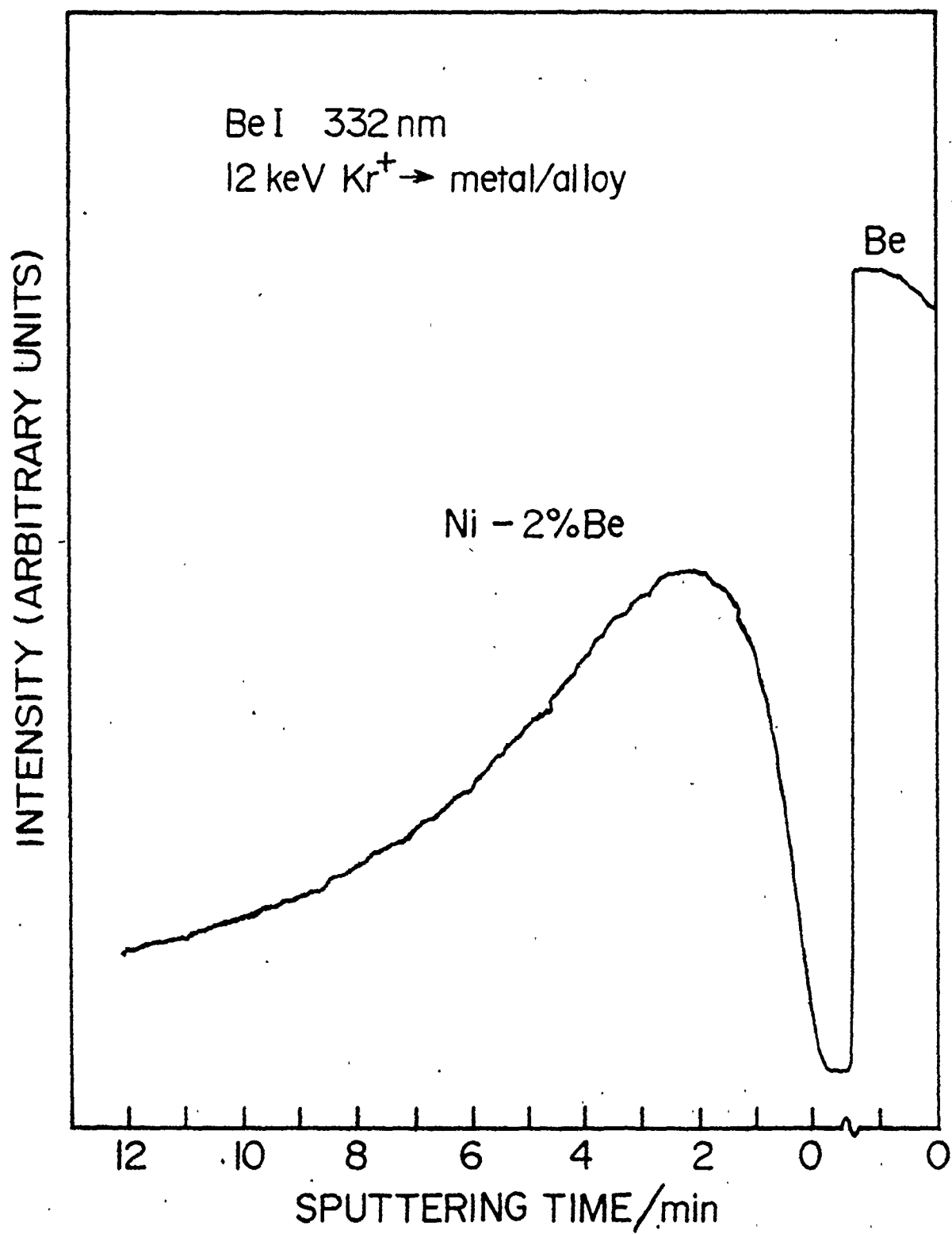


Figure 2.9. Photon signal from Be in the pure state (right) and an oxidized alloy.

distance from the target surface, could be obtained.

The alignment of the differentiating and monochromator entrance slits was done by employing a point source of light, as shown in Fig. 2.3, to maximize the signal from the source to the photomultiplier tube. Once these were aligned, the target surface was located, with respect to the differentiating slit, by simply maximizing the photon signal of a chosen transition. Figure 2.10 shows a typical "as obtained" intensity distribution for the BeI 234 nm photon. In general, the first step is to locate the line of interest by slowly scanning the monochromator as shown in the right portion of Fig. 2.10. Once the peak is located, the monochromator is locked and the target is raised (+ive direction) or lowered (-ive direction) in integral steps of 0.5 mm to locate the surface i.e., where the intensity is a maximum. This point defines $x = 0$ to within 0.2 mm due to the finite slit width. By lowering the target (-ive direction), an intensity distribution of BeI 234 is built up. This distribution extends well out in front of the target; approximately 7 mm for BeI 234 nm. As a further example, Figs. 2.11a and b show the intensity distributions obtained for the $2P^0 - 2S$ and $2P^0 - 2D$ series of LiI where the raw data have been plotted as $\ln(I/I_0) \equiv \ln(Y^{\text{diff.}})$, where I_0 is the intensity at the surface, against distance from the target. It should be emphasized that since these distributions were measured through a thin slit, they are by definition differential, hence the notation $Y^{\text{diff.}}$. Conversely, integral distributions can be obtained by viewing the light over an edge, hence: $Y^{\text{int.}}$. Further results pertaining to such intensity plots are given in section 2.3 following a proposed model for the distribu-

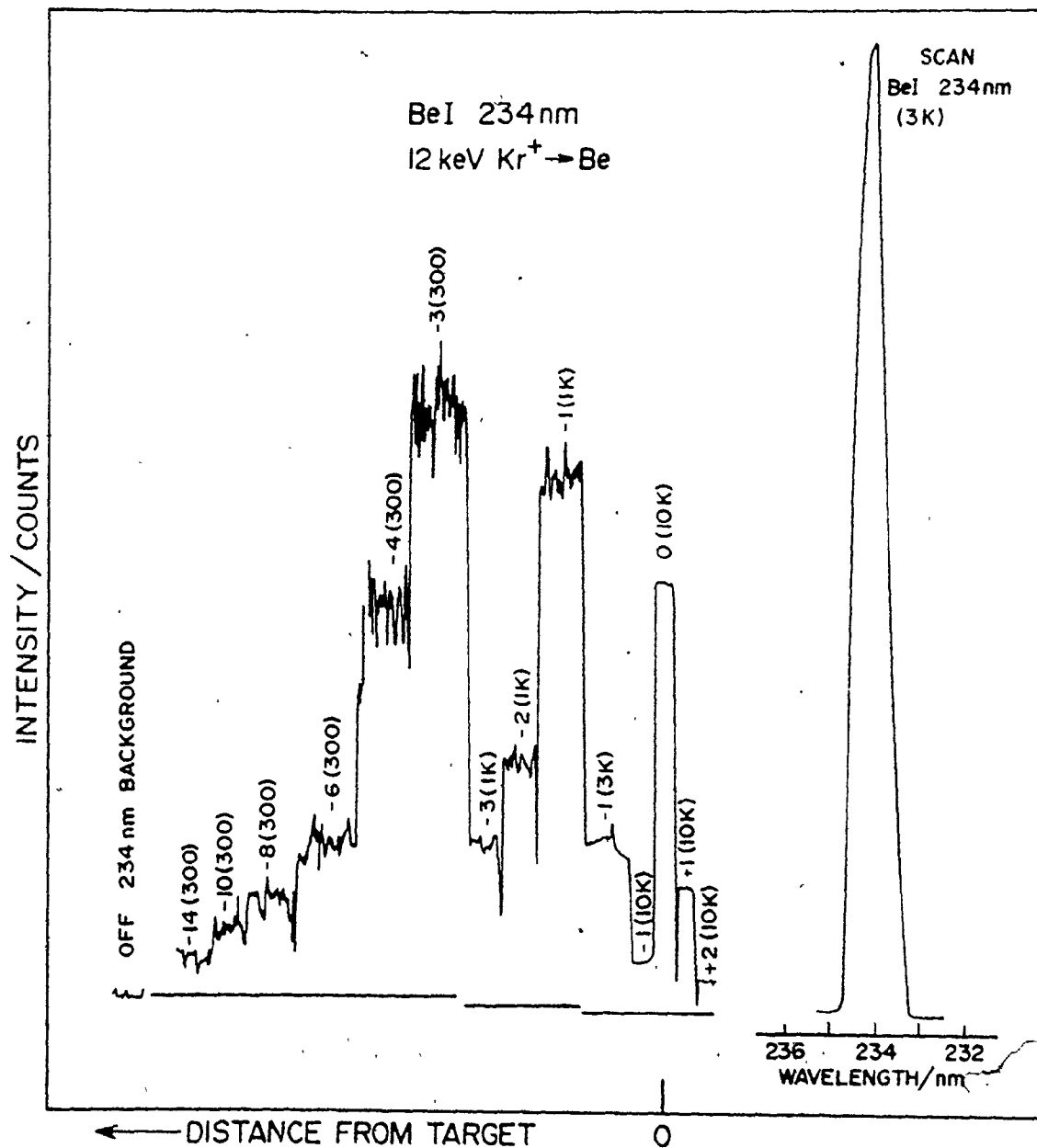


Figure 2.10. As obtained photon intensity distribution from BeI.

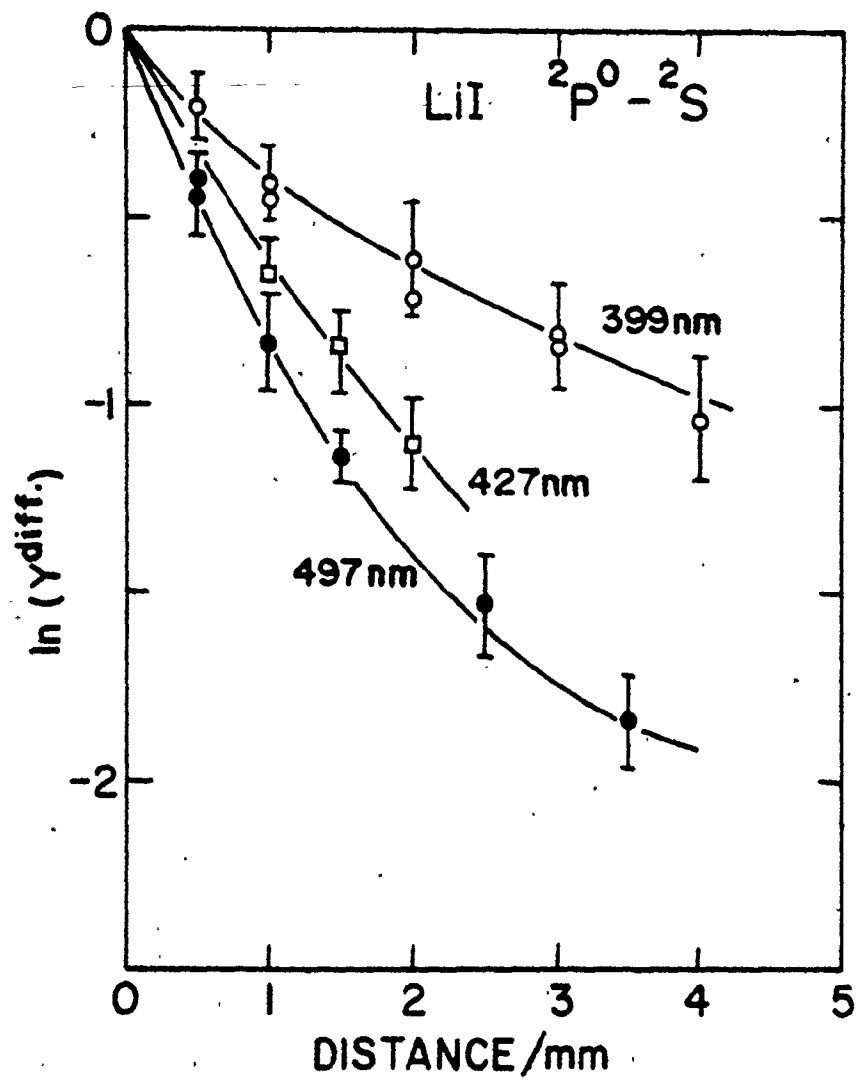


Figure 2.11a. Photon intensity distribution from LiI for three transitions.

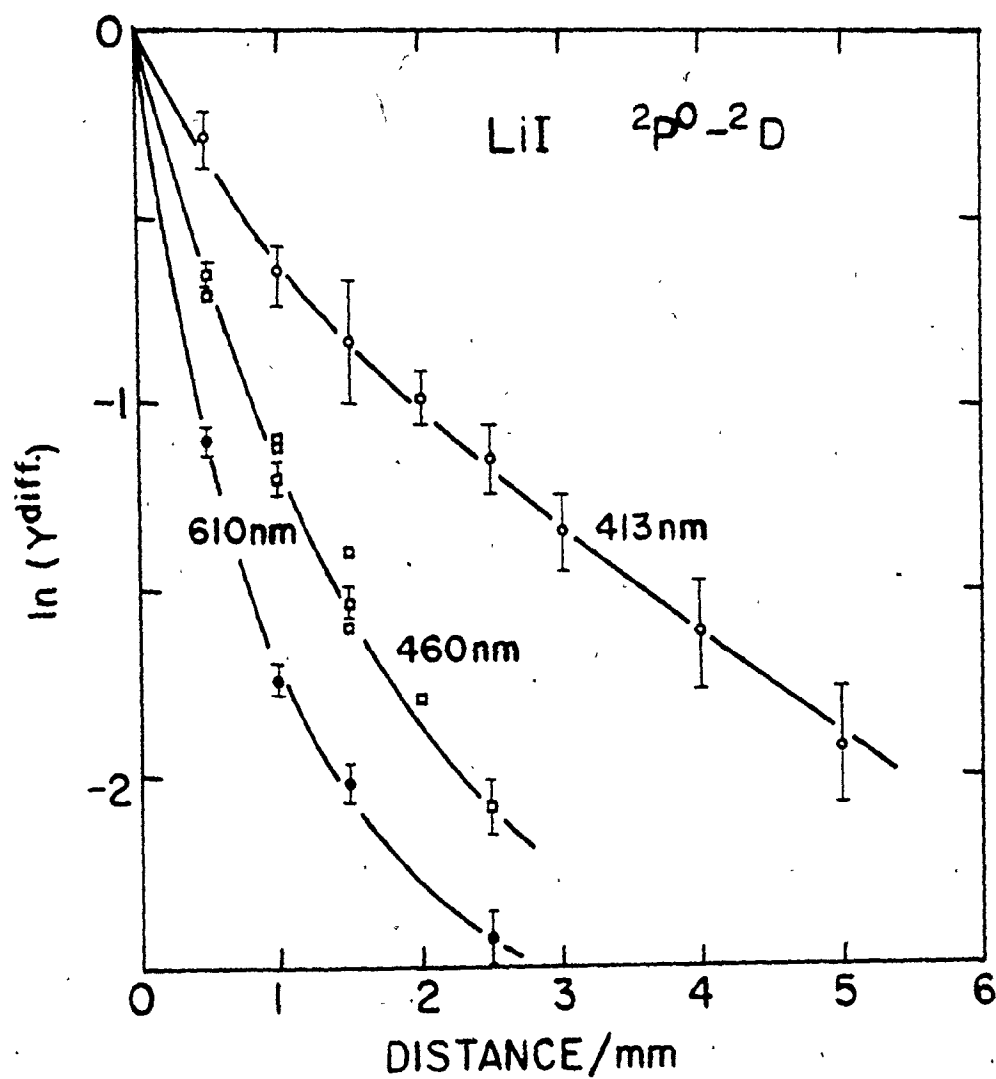


Figure 2.11b. Photon intensity distribution from LiI for three transitions.

tions. (All measured intensity distributions were differential)

2.3 ANALYSIS AND DISCUSSION OF INTENSITY DISTRIBUTIONS

2.3.1 Intensity Distribution Functions

In what follows it will be proposed that the measured intensity distributions can lead to an estimation of the velocity with which sputtered excited atoms leave the surface provided a postulate is made concerning the probability of finding an atom in an excited state, $P(E)$, given it has kinetic energy E . We will take several functional forms for $P(E)$ and compare the results.

The process of photon emission is illustrated in Fig. 2.12, where the rate of de-population of an excited level i (i =initial) is governed by the total rate of decay from the i^{th} level to levels f (f =final) and the total rate of feeding to the i^{th} level from levels u (u =upper), i.e.,

$$\frac{dN_i}{dt} = -\sum_f A_{fi} N_i + \sum_u A_{iu} N_u, \quad (2.5)$$

or in the absence of any feeding process

$$\frac{dN_i}{dt} = -\sum_f A_{fi} \cdot N_i \equiv -\gamma_i N_i, \quad (2.6)$$

where γ_i is called the decay rate constant. The relation in eq. (2.6) can be justified in particular cases by examining the lifetimes and relative populations of the upper feeding levels. Namely, (i) if the transition probability, A_{iu} , is small compared to that for the transi-

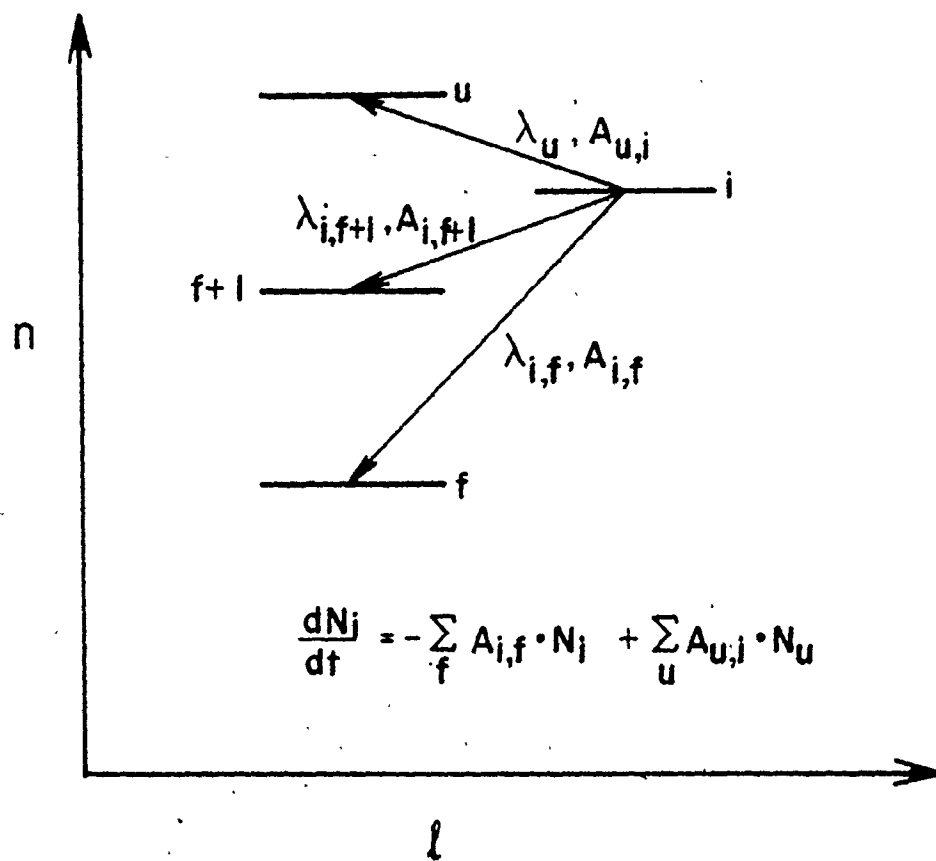


Figure 2.12. Electronic transitions involved in photon emission.

tion of interest, $i \rightarrow f$, then feeding can be neglected, (ii) if the populations of the excited levels are governed by Boltzmann (Saha) factors, then, for large principal quantum number n , the occupations fall off exponentially and hence N_u is small and the result in eq. (2.6) is justified. In what follows, we will first assume that no cascade feeding is active. We later investigate cases where this is not true.

Returning to eq. (2.6) and integrating we obtain the well known result,

$$N_i(t) = N_i^0 \exp(-\gamma_i t) , \quad (2.7)$$

for the population of the i^{th} level after a time t . Provided that the intensity, I , of photons emitted in such a decay is proportional to $N_i(t)$, then the yield of photons from a sputtered excited particle of kinetic energy E leaving the surface at an angle θ is

$$y(t) \propto \exp(-\gamma_i t) . \quad (2.8)$$

By substituting for t we get

$$y(E, \theta) = \exp(-bx/E^{1/2} \cos \theta) , \quad (2.9)$$

where $b = \gamma_i m^{1/2}/2^{1/2}$ and m is the mass of the sputtered atom.

Hagstrum (19) has shown that for a particle of perpendicular velocity, v_{\perp} (with respect to the surface), the probability of the

sputtered excited particle surviving a non-radiative decay beyond a distance x from the surface is given by

$$\begin{aligned} Q &= \exp\left(\frac{-A}{v_1}\right) \\ &= \exp(-a/E^{1/2} \cos\theta) , \end{aligned} \quad (2.10)$$

where a is most realistically an empirical constant. Also, since the sputtered atoms are distributed in their energies according to $dN(E)/dE$, the yield of photons becomes

$$y(E, \theta) = k \cdot Q \cdot (dN(E)/dE) \cdot \exp(-bx/E^{1/2} \cos\theta) \quad (2.11)$$

Next we postulate a probability of creating an excited sputtered atom whose kinetic energy is E , i.e., $P(E)$. We will take four cases for $P(E)$ and examine the differences, if any, in analyzing the experimentally obtained intensity distributions. Combining eq. (2.11) with $P(E)$ and with a factor $\cos\theta$ for an assumed isotropic angular distribution, we write the yield of photons (integral distribution) as

$$\begin{aligned} Y^{int} &= k \int_{E^*}^{\infty} \int_0^{\pi/2} Q \cdot (dN(E)/dE) \cdot P(E) \cdot \exp(-bx/E^{1/2} \cos\theta) \cdot \\ &\quad \sin\theta \cdot \cos\theta \cdot d\theta \cdot dE , \end{aligned} \quad (2.12)$$

where k represents all constants independent of E and θ . It now remains to evaluate eq. (2.12) for specific cases for $P(E)$ and appropriate choices for $dN(E)/dE$.

CASE I: We first postulate that the probability of finding an atom in an excited state, given that the sputtered atom has kinetic energy E , as a threshold step function, namely

$$P(E) = 0 \quad \text{for } E < E^* \quad (2.13a)$$

$$= \text{constant.} \quad \text{for } E \geq E^* \quad (2.13b)$$

This probability may be valid if the excitation mechanism is one involving inner curve crossings as outlined in section 2.1.2. The sputtered energy distribution, $dN(E)/dE$, is taken as

$$\frac{dN(E)}{dE} \propto \frac{E}{(E + E_b)^3} \quad (2.14)$$

which is a function characteristic of sputtered ground state neutrals (20). For energies much greater than the surface binding energy, E_b , eq. (2.14) reduces to

$$\frac{dN(E)}{dE} \propto \frac{1}{E^2} \quad (2.15)$$

In evaluating the integral in eq. (2.12), we proceed by first integrating the angular functions, while holding the energy constant, i.e.,

$$I(\theta) = \int_0^{\pi/2} \exp(-z'/\cos\theta) \cdot \sin\theta \cdot \cos\theta \cdot d\theta, \quad (2.16)$$

where $z' = (a + bx)/E^{1/2}$. By substituting $u = 1/\cos\theta$, eq. (2.16) becomes

$$I(z') = \int_1^\infty u^{-3} \exp(-z'u) du ,$$

which is just the exponential integral of order 3 (21), and is written

$$\begin{aligned} I(z') &= E_3(z') \\ &= E_3\left(\frac{a + bx}{E^{1/2}}\right) . \end{aligned} \quad (2.17)$$

The photon intensity distribution is now written, by putting eq. (2.17) into eq. (2.12), as

$$Y^{\text{int}} = k \int_{E^*}^\infty (dN(E)/dE) \cdot P(E) \cdot E_3\left(\frac{a + bx}{E^{1/2}}\right) dE , \quad (2.18)$$

where, for this first choice of $P(E)$, the lower limit of integration is the threshold energy E^* and the upper limit is taken as infinity.

Strictly speaking, the upper limit should be the maximum transferred energy in a binary collision, $4M_1M_2E_1/(M_1 + M_2)^2$, however, we assume this to be much greater than E^* . Now, putting the step function and $dN(E)/dE$ into eq. (2.18) yields the result

$$\begin{aligned} Y^{\text{int}} &= k \int_{E^*}^\infty \frac{1}{E^2} E_3\left(\frac{a + bx}{E^{1/2}}\right) dE \\ &= \frac{2k}{(a + bx)^2} \int_0^z z' E_3(z') dz' , \end{aligned} \quad (2.19)$$

which has the solution

$$Y^{int}(z) = \frac{k}{2z^2 E^*} \{1 - e^{-z} - 3zE_4(z)\} , \quad (2.20)$$

where $z = (a + bx)/E^{*1/2}$. Equation (2.20) then, gives the yield of photons (light intensity) as a function of distance from the target surface ($z \propto$ distance) under the assumption of a threshold type behavior for excitation. Equation (2.20) can be put into normalized form by constructing

$$Y^{int}(z) = y^{int}(z)/y^{int}(0) . \quad (2.21)$$

By expanding the exponential term in eq. (2.20) and recognizing that

$E_n(0) = \frac{1}{n-1}$, it is easily shown that

$$Y^{int}(0) = k/2E^* , \quad (2.22)$$

so that the normalized integral intensity distribution is

$$Y^{int}(z) = \frac{1}{2} \{1 - e^{-z} - 3zE_4(z)\} \quad (2.23a)$$

$$Y^{int}(0) = 1 . \quad (2.23b)$$

This result is applicable for experimentation wherein the light above the target is viewed over an edge, however, a differential distribution can be constructed, applicable when viewing the light through a

slit, by simply differentiating eq. (2.20). That is

$$\begin{aligned} \gamma^{\text{diff}}(z) &= \frac{d}{dz} \gamma^{\text{int}}(z) \\ &= \frac{2}{z^2} \left\{ e^{-z} \left(\frac{1}{z} + 1 \right) - \frac{1}{z} + z E_3(z) \right\}, \end{aligned} \quad (2.24)$$

and by normalizing this we obtain the differential form

$$\gamma^{\text{diff}}(z) = \frac{3}{2z^2} \left\{ \frac{1}{z} - \left(1 + \frac{1}{z} \right) e^{-z} - z E_3(z) \right\} \quad (2.25a)$$

$$\gamma^{\text{diff}}(0) = 1. \quad (2.25b)$$

This differential intensity distribution is shown in Fig. 2.13 for the step function case (Case I). Two approaches can be taken in analyzing the measured distributions using eq. (2.25a). Firstly, one could simply curve fit the data through the parameter $b/E^{*1/2} = \gamma_{im}^{1/2}/2^{1/2} E^{*1/2}$ since all quantities are known except E^* . (This also assumes $a = 0$) A second approach, one which is employed here, is to assign a z value (from Fig. 2.13) for each measured intensity ratio, I/I_0 . One then plots z versus measured distance, x , which should yield a straight line of slope $\gamma_{im}^{1/2}/2^{1/2} E^{*1/2}$ and from tabulated data on transition probabilities (22) evaluate $\gamma_i = \sum_f A_{if}$ hence obtaining E^* , the proposed threshold energy. This approach avoids putting a restriction on a.

CASE II: As mentioned earlier, a portion of the total sputtered flux is in the form of ions, this being the basis of secondary ion emission

mass spectrometry (SIMS). Some of these are also in excited states.

Following some evidence concerning the sputtering of ions (23), we formulate the intensity distribution of sputtered excited ions by using $dN(E)/dE \propto E^{-3/2}$ along with a threshold behavior as in Case I.

This renders eq. (2.18) as

$$Y^{\text{int}}(z) = \frac{2}{z} \left\{ \frac{1}{3} - E_4(z) \right\} \quad (2.26a)$$

$$Y^{\text{int}}(0) = 1, \quad (2.26b)$$

and analogously, in normalized differential form

$$Y^{\text{diff}}(z) = \frac{2}{3z^2} \{ 1 - e^{-z} - 2zE_3(z) \} \quad (2.27a)$$

$$Y^{\text{diff}}(0) = 1. \quad (2.27b)$$

This result as might be expected for sputtered excited ions, is also plotted in Fig. 2.13.

CASE III: Here we explore the possibility of $P(E)$ being velocity dependent. This follows from the nature of inelastic stopping in a solid being also proportional to the ion velocity. In particular

$$P(E) = (E - E^*)^{1/2} \quad \text{for } E \geq E^* \quad (2.28a)$$

$$= 0 \quad \text{for } E < E^* \quad (2.28b)$$

By expanding $P(E)$ and retaining the first three terms, and approximating the sputtered energy distribution as $dN(E)/dE = E^{-2}$, we get

$$\gamma^{\text{int}}(z) = \frac{12}{5z^3} \left\{ 1 - (1+z)e^{-z} - \frac{3z^2}{2} E_4(z) \right\} \quad (2.29a)$$

$$\gamma^{\text{int}}(0) = 1, \quad (2.29b)$$

or in differential form

$$\gamma^{\text{diff}}(z) = \frac{8}{15z^2} \left\{ \frac{5}{3} - \frac{3}{z^2} - \left(\frac{1}{6} - \frac{3}{z} - \frac{3}{z^2} \right) e^{-z} - \frac{7z}{3} E_3(z) \right\} \quad (2.30a)$$

$$\gamma^{\text{diff}}(0) = 1. \quad (2.30b)$$

In the preceding cases, the reduced variable is $z = (a + \gamma_{im}^{1/2} x) / 2^{1/2} E^{*1/2}$ and each case contains a postulate about the probability of excitation which, throughout Cases I-III, has involved a threshold phenomenon. It is worth pointing out at this point that the assumption of a threshold kinetic energy E^* has in effect determined the form of $dN(E)/dE \propto E^{-n}$ since we assume that $E^* \gg E_b$. In turn, the inverse power relationship in $dN(E)/dE$ has facilitated analytical solutions to the integrals in eqs. (2.12) and (2.18), which would otherwise have been intractable. One exception to this difficulty is a case where no threshold behavior is implied: this constitutes CASE IV.

CASE IV: Here we assume that all sputtered particles have equal (and constant) probability of being found in the excited state independently of their energy. That is, the assumption of a threshold is removed, however, is replaced by the qualification that the sputtered particle must overcome the surface binding energy E_b . This assumption leads to the use of the sputtered energy distribution in its full form,

$$\frac{dN(E)}{dE} = \frac{E}{(E + E_b)^3} \quad (2.31)$$

The intensity distribution in integral normalized form becomes, by putting eq. (2.31) into eq. (2.18) and integrating from E_b to infinity,

$$Y^{int}(z) = 1 - zf(z) \quad (2.32a)$$

$$Y^{int}(0) = 1, \quad (2.32b)$$

or its equivalent in differential form,

$$Y^{diff}(z) = \frac{2}{\pi} \{f(z) - zg(z)\} \quad (2.33a)$$

$$Y^{diff}(0) = 1. \quad (2.33b)$$

The variable z in this case is $(a + bx)/E_b^{1/2}$ where E_b is the surface binding energy. The functions $f(z)$ and $g(z)$ are given, as in Abramowitz and Stegun (21), by

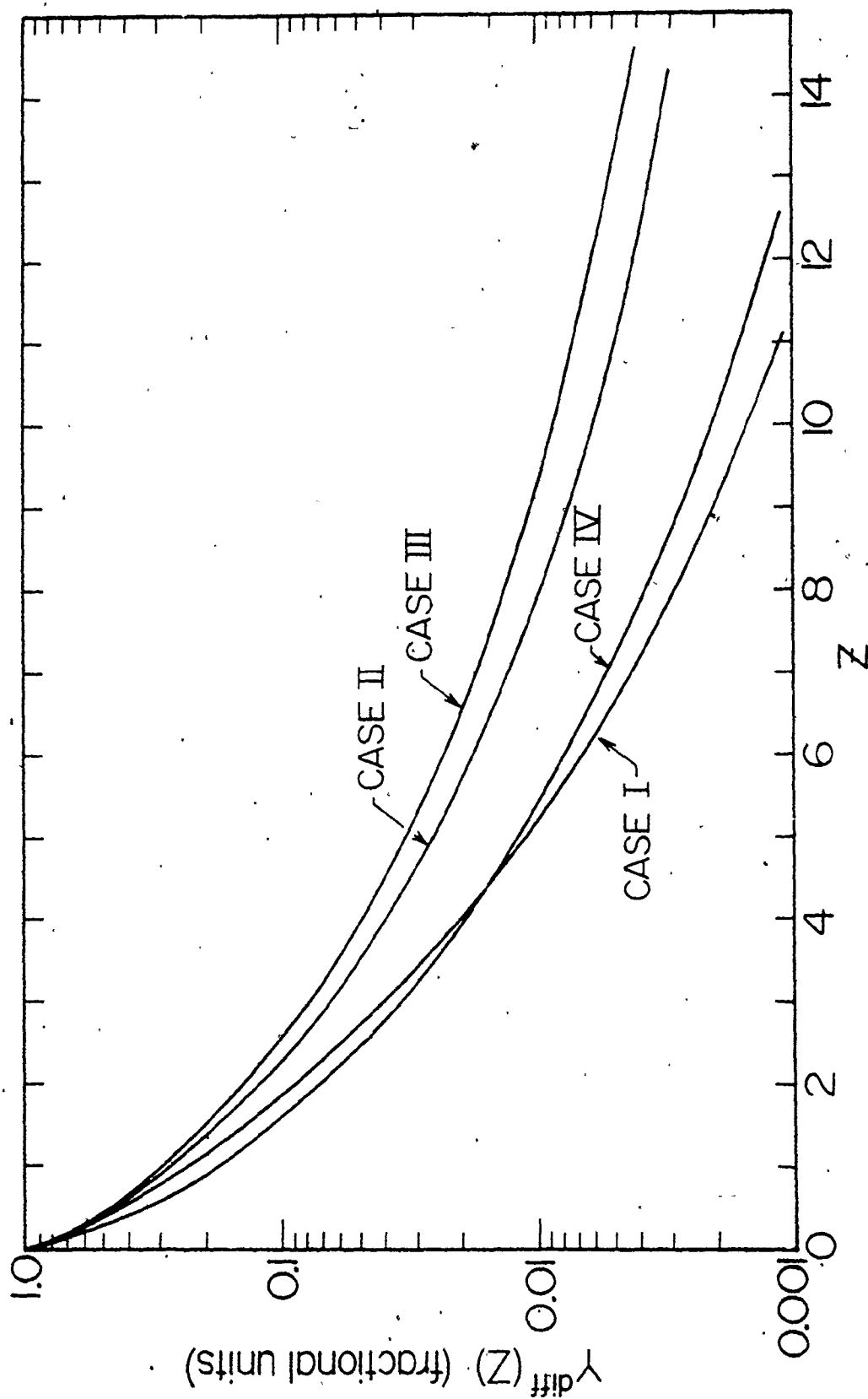


Figure 2.13. Calculated intensity distribution functions in differential form for four cases for $P(E)$.

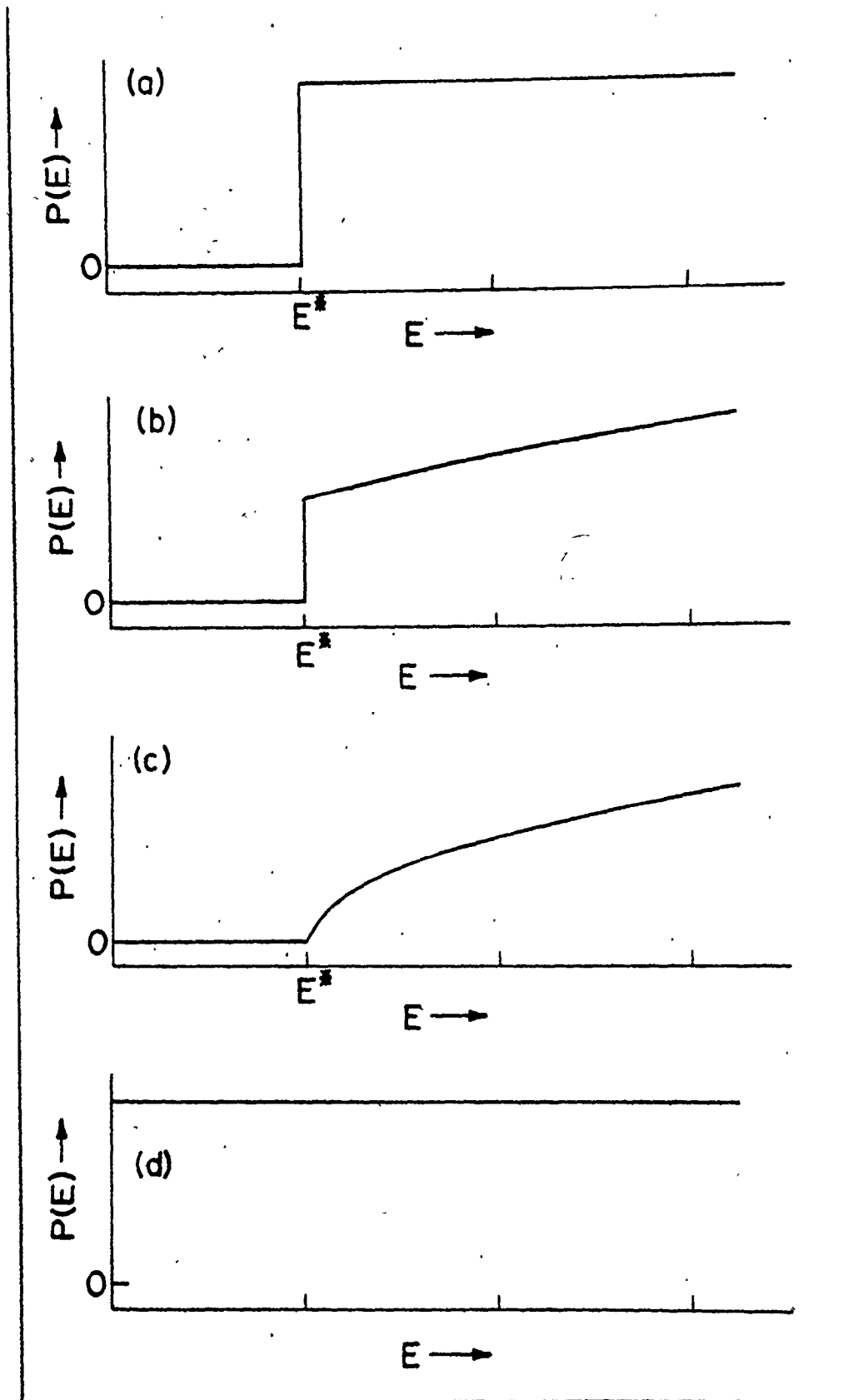


Figure 2.14. Schematic illustrations for the four cases for finding an atom in an excited state given it has kinetic energy E .

$$f(z) = Ci(z) \cdot \sin(z) - si(z) \cdot \cos(z), \quad (2.34a)$$

$$g(z) = -Ci(z) \cdot \cos(z) - si(z) \cdot \sin(z). \quad (2.34b)$$

In this particular case, the analysis of the measured intensity distributions should give rise to E_b of the order of 1-10 eV, as deduced from thermodynamic quantities. In anticipation of what will follow, any large deviation from such values would render this case suspect in light of the fact that surface binding energies are relatively small and constant.

Finally, in all cases the functions $Y^{\text{diff}}(z)$ are used to linearize the observed light intensity distributions, through use of Fig. 2.13, by plotting z versus distance and deducing E^* , the threshold energy or E_b the surface binding energy. In addition, Fig. 2.14 summarizes the cases for $P(E)$.

We now return to the experimental data and apply the preceding section to Li, Na and the group IIA fluorides.

2.3.2 Discussion

As shown in section 2.2.3, LiI (the numeral I indicating neutral Li atoms) photon intensity distributions were measured as a function of distance from the target surface and were given in Figs. 2.11a and b for several transitions. The linearization of such data, as discussed in section 2.3.1, is shown for some LiI and NaI transitions in Figs. 2.15 and 2.16 in terms of z vs x . In the LiI and NaI data, the step function formalism was used (Case I). Both the Li and Na plots

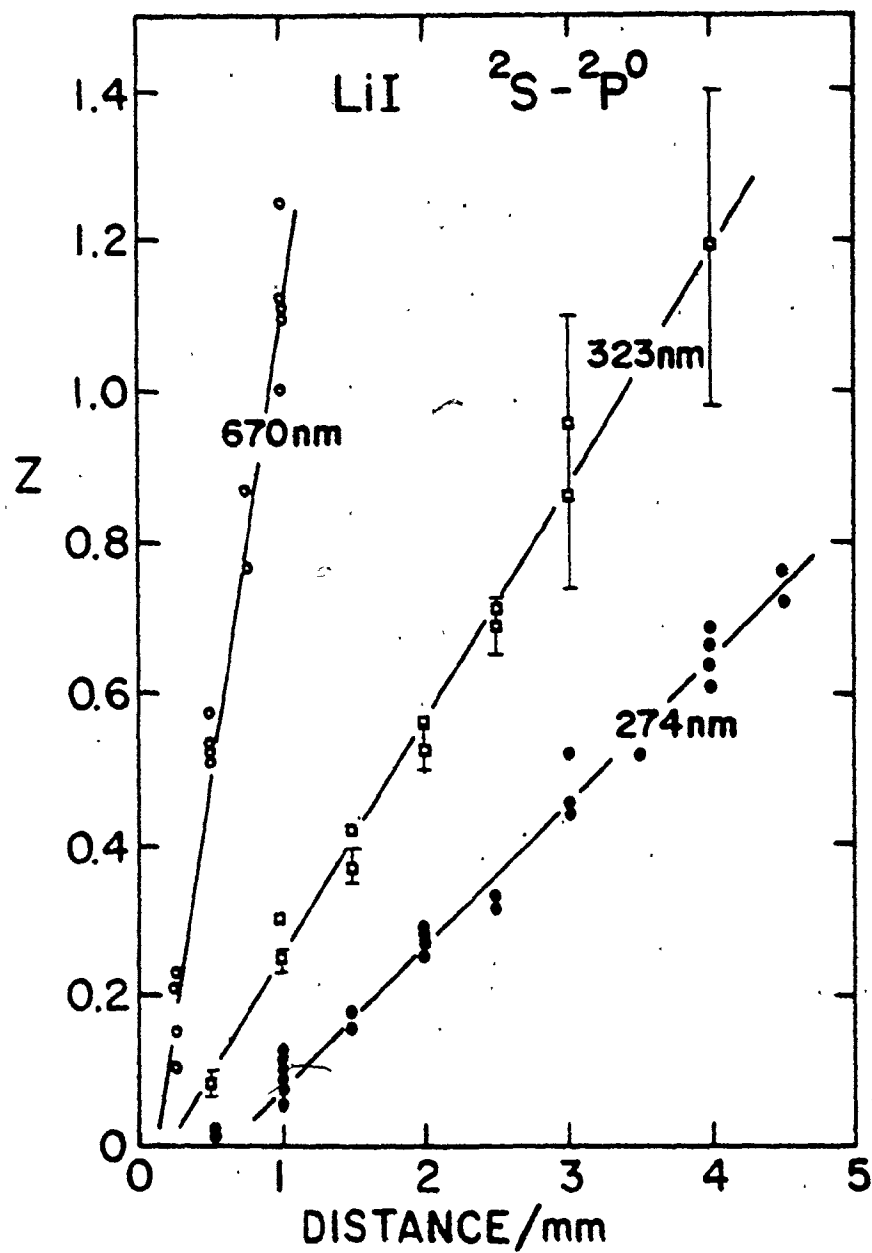


Figure 2.15. Linearization plots for some LiI transitions.

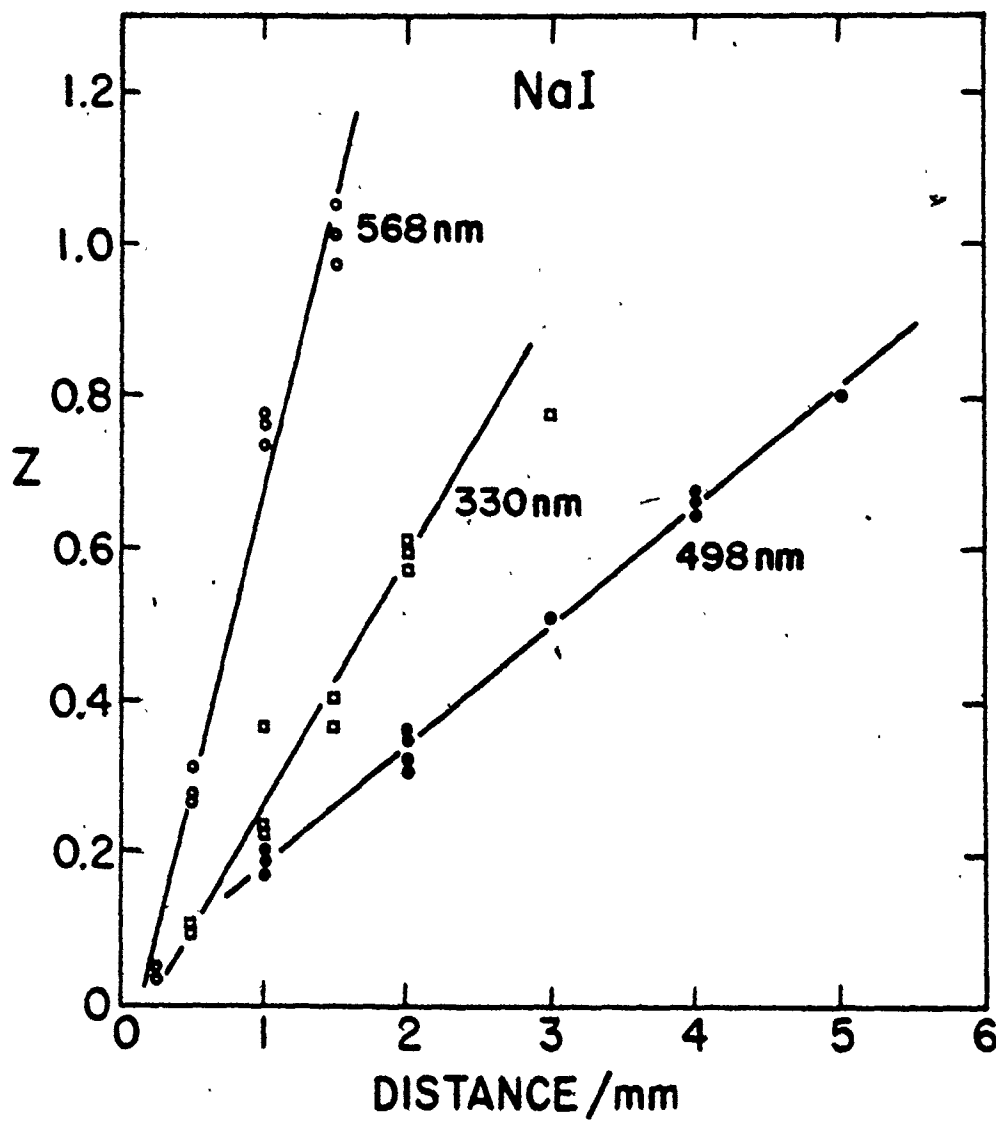


Figure 2.16. As in 2.15 except for some NaI transitions.

show excellent linearity over approximately three orders of magnitude in I/I_0 , although the intercept is not zero. The origin of this displacement is twofold: (i) The variable z is $(a + bx)/E^{*1/2}$, from which, in principle, the intercept renders a value for the empirical constant a . (ii) The accuracy with which one is able to locate the surface of the target is ultimately governed by the differentiating slit having a finite width (0.2 mm). With these two problems in mind it is the writer's opinion that the second effect predominates and any attempt to extract information concerning a would most likely prove fruitless.

Now, using the step function formalism (Case I), Table 2.2 lists the results for several LiI and NaI transitions. The first column of Table 2.2 indicates that the targets used were either the metallic state or in fluoride or chloride form. It should be recognized that for metallic Li targets, the surfaces were fully oxidized, even with the beam on. Further, in the cases where the fluorides or chlorides were used, a thin sheet of electron microscope mesh was placed over the surface in order to prevent target charging which would disrupt the beam size or position. The second entry lists the transitions investigated where the notation reads lower state \leftarrow upper state (e.g., $2s \leftarrow 2p$) followed by the wavelength for the photon emitted in such a transition. The fourth column tabulates the decay rate constants, $\gamma_i = \sum_f A_{if}$, where A_{if} is the "transition probability" from the initial to particular final level. The last entry lists the deduced threshold kinetic energies. The most striking feature is the fact that these energies are markedly higher than the surface binding

Table 2.2

Sputtered excited atoms from Li and Na.

Target	Transition	Wavelength, nm	Decay Constant $\tau_i = \sum A_{fi}$ 10^7 s^{-1} (Refs. 22a, b)	Threshold Energy, eV	
Li, LiF	$2S-2P^0$	2s-2p	671	3.72	31
Li, LiF		2s-3p	323	0.494	9
Li		2s-4p	274	0.274	7
Li, LiF	$2P^0-2S$	2p-4s	497	1.76	28
Li		2p-5s	427	0.961	24
Li		2p-6s	399	0.571	40
LiF	$2P^0-2D$	2p-3d	610	7.16	44
Li		2p-4d	460	2.99	24
Li, LiF		2p-5d	413	1.54	53
NaCl	$2S-2P^0$	3s-4p	330	0.928	97
NaCl	$2P^0-2D$	3p-4d	569	1.98	83
		3p-5d	498	$\sim 0.76^a$	306

^a Lacks A_{fi} for 5p-5d.

energy, E_b , and basically lie in the interval $10^1 - 10^2$ eV. This relatively high energy is a first indication that the sputtering of excited atoms or the creation of excited atoms in a collisional event is certainly not a typical event.

In addition to the sputtering of excited atoms, observations were made on excited ions as given in Fig. 2.17 for Ca^+ , Sr^+ and Ba^+ ions. Here the targets were Group IIA fluorides. A summary of the data for these targets appears in Table 2.3, where the targets, transitions, wavelengths, decay rate constants, and a statement concerning the cascade feeding problem is listed. In Table 2.4, we present the proposed threshold energies or surface binding energies as obtained using all four analyses of section 2.3.1 for sputtered excited atoms and ions. Again, the energies are relatively high. The entries for Case IV (surface binding energy) reveal that the assumption of no threshold is probably not valid for physical reasons, i.e., E_b values should be in the range 1 - 10 eV rather than $10^2 - 10^3$ eV.

A general picture now emerges that indicates an inherent and perhaps fundamental difference between species sputtered in excited states and those sputtered as ground states. In fact several differentiating features can be identified;

- (i) Energies. Throughout this investigation (cf. Tables 2.2 and 2.4) we report anomalously high kinetic energies for the excited sputtered species - both atomic and ionic. This feature can be compared to the sputtered energies for ground state atoms and ions as illustrated in Table 2.5, where the most probable energies and average energies are

Table 2.3

Transitions, decay rate constants for Group IIA fluorides.

Target	Transition	Wavelength, nm	Decay rate constant, γ_i , 10^8 s^{-1} (ref.)	Is cascading a problem ^a
MgF ₂	MgI $1S_0-1P_1^0$	285.2	0.22 ^b (22b)	yes (Y, γ)
	MgI $3P_0-3D_1$	383.5	1.69 (22b)	possibly (Y, γ)
	MgI $3P_0-3S_1$	517.8	1.04 (22b)	possibly (Y, γ)
	MgII $2S_{1/2}-2P_0^0$	279.8	2.67 (22b)	no (Y, γ)
CaF ₂	CaI $1S_0-1P_1^0$	422.7	2.18 (22b)	no (Y)
	CaII $2S_{1/2}-2P_{3/2}^0$	393.4	1.61 (22b)	no (γ)
	CaII $2S_{1/2}-2P_{1/2}^0$	396.8	1.57 (22b)	no (Y, γ)
SrF ₂	SrI $1S_0-1P_1^0$	460.7	2.14 (27a)	-
	SrII $2S_{1/2}-2P_{3/2}^0$	407.8	1.78 (27b)	-
	SrII $2S_{1/2}-2P_{1/2}^0$	421.6	1.48 (27c)	-
BaF ₂	BaI $1S_0-1P_1^0$	553.5	1.15 (22c)	probably no (Y)
	BaII $2S_{1/2}-2P_{3/2}^0$	455.5	1.61 (22c)	no (Y, γ)
	BaII $2S_{1/2}-2P_{1/2}^0$	493.4	1.29 (22c)	no (γ , γ)

^a Cascading effects are based upon upper level yields (Y) or decay rate constants, γ . (cf. text section 2.3.1)

^b This value is deduced directly from beam foil spectroscopy ref. 22a.

Table 2.4

Characteristic energies for Group IIA fluorides.

Wavelength, nm	E* for Case I (eV)	E* for Case II (eV)	E* for Case III (eV)	E* for Case IV (eV)
MgI 285.2 ^a	40	20	15	40
MgI 383.5	640	400	340	760
MgI 517.8	1050	360	290	1170
MgII 279.8	1600	820	760	1520
CaI 422.7	1580	630	510	1510
CaII 393.4	1060	530	470	900
CaII 396.8	1280	620	410	1060
SrI 460.7 ^b	(9600)	(4300)	(4000)	(9200)
SrII 407.8	2270	1240	900	2500
SrII 421.6	1300	740	620	1830
BaI 553.5	2900	1040	920	2350
BaII 455.4	1950	1130	980	1730
BaII 493.4	1380	980	720	1130

^a We have here assumed the decay rate constant for cascade feeding (22b).

^b These results appear to be high, as if unsuspected cascade played a role.

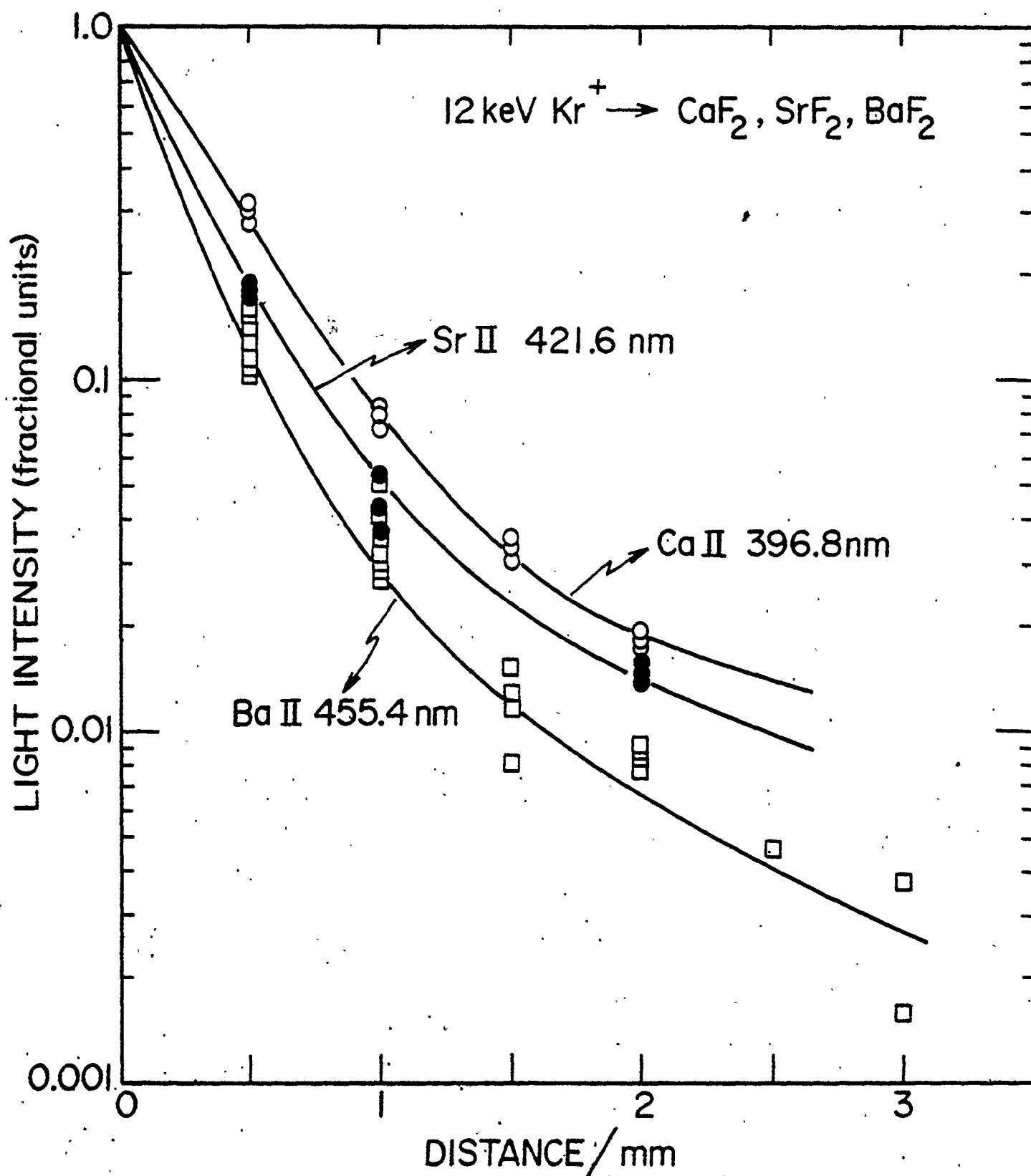


Figure 2.17. Intensity distribution for several sputtered excited ions.

listed. The values tabulated in Table 2.5 are obtained by analyzing experimental sputtered energy distributions from which the average energy is obtained.

Also given in Table 2.5 are the heats of atomization for the elements, which give an estimate of the surface binding energy. Comparing Tables 2.2, 2.4 to Table 2.5, dramatically illustrate that energies of excited species are substantially greater than those for ground state atoms or ions. With respect to excited atoms and ground state ions, the difference in kinetic energies suggests that secondary ion emission is not simply an extension of secondary photon emission but that they have origins of different sorts. For example, secondary ions could in principle be created simply from a "bond breaking" process whence their energies would be as those typifying the overall sputtering event.

(ii) Sizes. From classical atomic structure, the mean Rydberg radius of an atom in an excited state, characterized by the quantum numbers n and ℓ , is

$$\langle r \rangle = \frac{n^2 a_0}{Z} \left\{ 1 + \frac{1}{2} \left[1 - \frac{\ell(\ell+1)}{n^2} \right] \right\}, \quad (2.35)$$

where a_0 is the Bohr Radius and Z the effective atomic number. For excited states in this investigation we find $\langle r \rangle$ in the range 6-30 Å.

This size is to be compared to ions (~2 Å) or the atomic separations in solids (~2 Å). The implication is that if excited states are created in the collision cascade, they certainly could not survive an excursion to the

Table 2.5

Previous measurements of energies of secondary ions. Ref. 28.

Target	Most probable energy, eV.	Average energy, eV.	Surface binding energies, eV.
Mg	4.6	18.0	-
Al	4.6	18.5	9.2
Si	4.7	31.0	3.8
Ti	6.5	31.0	6.1
V	4.1	33.0	-
Cu	4.6	65.0	2.3

surface and still remain in an excited state. More likely, one can propose that excited states are created in very near surface collisions (recoil events) involving large energy transfers from the primary ion.

(iii) Yields. An estimate of the total yield (i.e., excited atoms/sputtered atom) can be made if it is assumed that the energy distribution follows the form

$$\frac{dN(E)}{dE} = \frac{2EE_b}{(E + E_b)^3}, \quad (2.36)$$

written normalized to unity. The fraction of sputtered species in excited states with energies greater than the threshold is, by integrating eq. (2.36), just

$$N(E^*) = \frac{2E^* E_b + E_b^2}{(E + E_b)^2} \quad (2.37)$$

Corresponding to the LiI and NaI data, $N(E^*)$ is in the range 0.06-0.4 excited atoms/sputtered atom. These values are reasonable in that they exceed the absolute yields as measured by Tsong and Yusuf (24), namely, 0.008 for LiI 670 and 0.01 for all excited states of Na. For CaI 422.7, for which E^* is 510-1580 eV, the fraction $N(E^*) = 0.007-0.02$ with E_b taken as 5 eV. Again, logical agreement is obtained with the data from Tsong and Yusuf, who measured 0.003 photons/sputtered atom.

With respect to yields of secondary ions and secondary photons, it is generally observed that both yields are enhanced by the presence of oxygen.

Indeed, except for the presence of oxygen, all the observations lead us to believe that excitation during sputtering has origins different from that for ionization. In particular, the mechanism of curve crossing seems very attractive in so far as it justifies a threshold phenomenon for excitation. Further we find it reasonable that excited states involve collisions at the very surface.

Finally, of particular interest concerning the intensity distributions are instances when cascade feeding seems to play an important role, as in the case of the Mg 383 photon shown in Fig. 2.18. When plotted in terms of z versus distance, the MgI 383 nm line shows a break in slope at approximately 2 mm while the 517 nm and 285 nm lines show excellent linearity. We interpret this change in slope, not as two velocity groups, but rather the result of longer lived upper states controlling the de-population of the $3d\ ^3D$ level of MgI. For example, as shown in Fig. 2.19, the transition $3p\ ^3P^0 - 3d\ ^3D$ (383 nm) is fed by several $nf\ ^3F^0$ states and $np\ ^3P^0$ states. It is these levels which are assumed to contribute to the cascade feeding. In so far as this is true, only the first portion of the z vs distance plot is used in evaluating threshold energies. Still concerning MgI, Fig. 2.20 illustrates the ordering effect in spatial extension based on the level lifetime, τ_i . The distributions for short lived states decay close to the surface (eg., MgI 383.5 nm, $\tau = 5.9$ ns) while the longer lived states (eg., MgI 517.8 nm, $\tau = 9.6$ ns) are further extended in front of the target. Along these lines, states which are very short lived, such as MgI 285.2 nm, 0.2 ns, should have decayed practically at the surface in which case the observed intensity distribution must be the

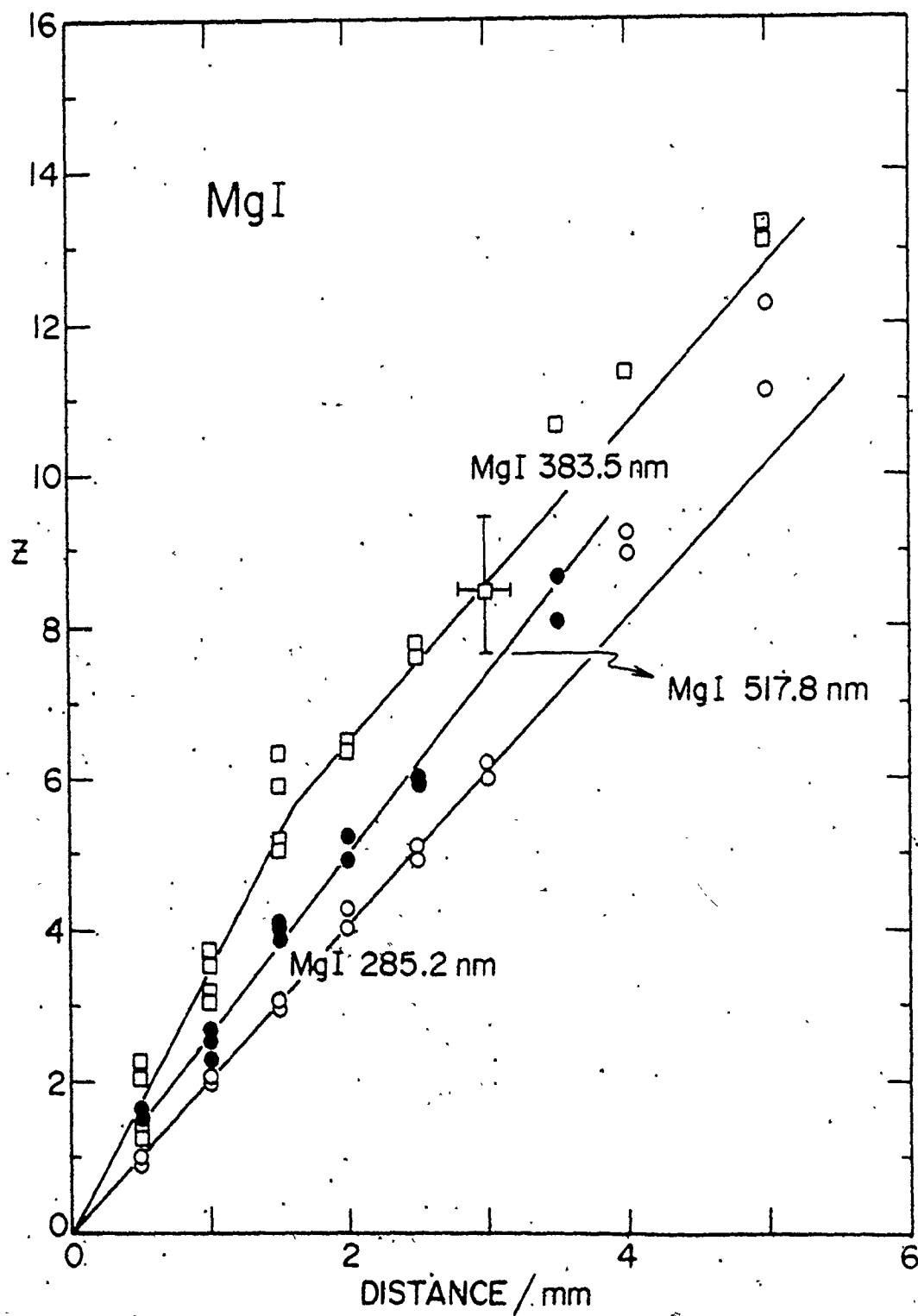


Figure 2.18. Linearization plot for Mg transitions showing a cascade effect for the MgI 383.5 nm line.

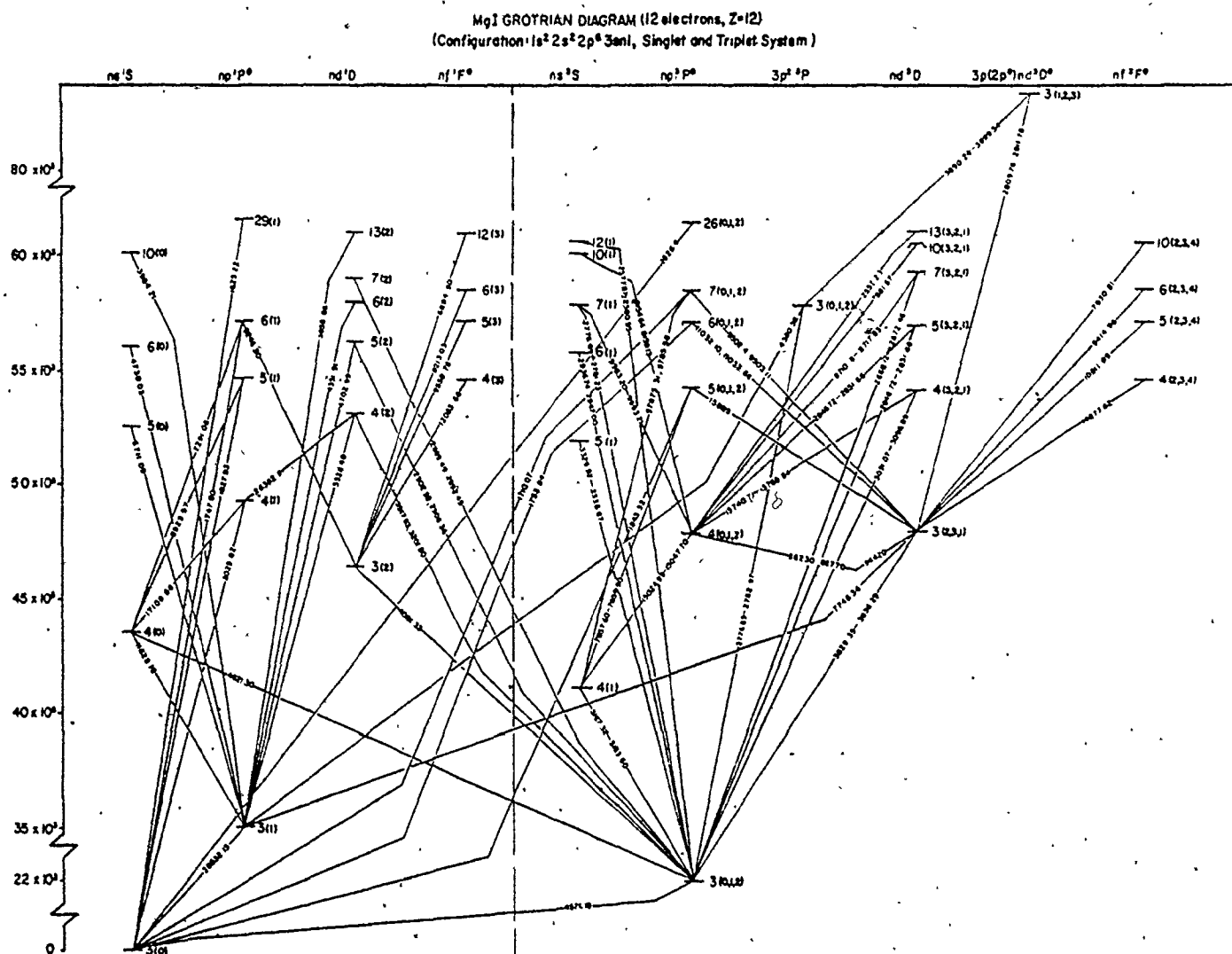


Figure 2.19. Grotrian diagram for Mg.

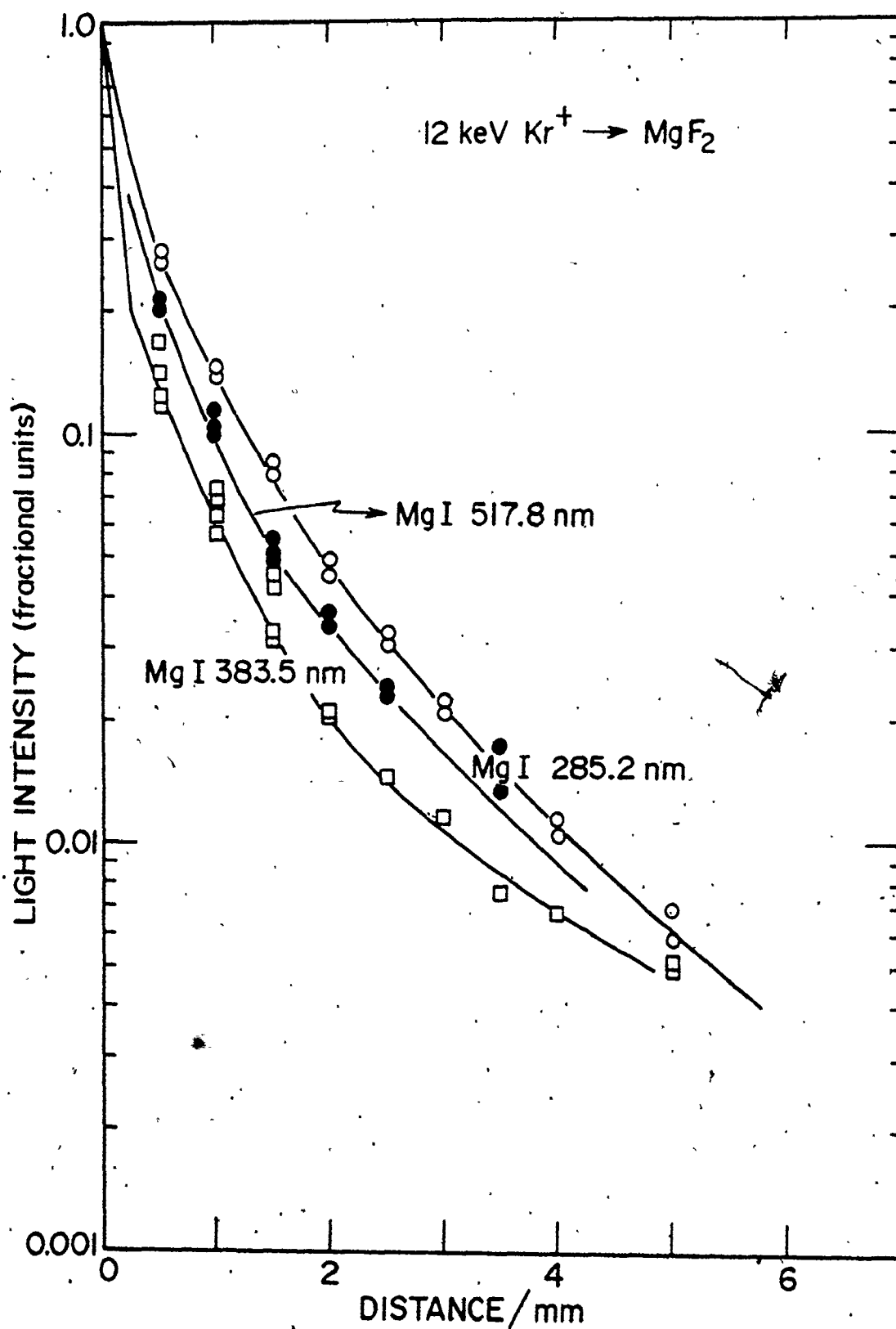


Figure 2.20. Intensity distributions for Mg illustrating the effect of the decay rate constant.

APPENDIX 2.1

NORMALIZED INTEGRAL DISTRIBUTIONS

Consider a function $f(x)$ which is continuous and well behaved over the interval $[x, b]$. Then, one can construct the integral form of this function as

$$F(x) = \int_x^b f(x') dx' \quad \text{A.2.1.1}$$

In the context of atomic collision phenomena, $f(x)$ can be, for example, a differential concentration depth distribution, for which one considers the integration limits as $[x, b] = [x, \infty]$, i.e., from a depth x to very large depths in the solid. Then we get

$$F(x) = \int_x^{\infty} f(x') dx \quad \text{A.2.1.2}$$

as the integral concentration depth distribution. In addition, the integral formalism is often normalized such that

$$F(0) = 1 \quad \text{A.2.1.3}$$

This property is valid of course only if the integrand $f(x')$ is well behaved, namely, convergent as $x \rightarrow 0$.

APPENDIX 2.2

SURFACE NORMAL ENERGY DISTRIBUTION OF SPUTTERED RECOILS

In the treatment concerning the sputtering of excited states (cf. section 2.3.1), the sputtered energy distribution was stated to be of the form

$$f(E)dE \propto \frac{EdE}{(E + E_b)^3}$$

$$= \frac{dE}{E^2} \quad \text{A.2.2.1}$$

for $E \gg E_b$. Here, E_b is the surface binding energy. This result is now justified by considering the internal fluxes.

For random collisions in an isotropic medium we will accept the result that internal flux of recoil atoms in a given direction due to a source is

$$f_i(E_i)dE_i \cos\theta \sin\theta d\theta \propto \frac{1}{E_i^2} dE_i \cos\theta \sin\theta d\theta \quad \text{A.2.2.2}$$

as illustrated in Fig. A.2.1. If these recoil atoms are at the surface they will tend to escape; however the physical surface imposes a barrier to escape, by an amount E_b , the surface binding energy, such that for the external flux we use

$$f_e(E_e)dE_e \cos\phi \sin\phi d\phi \propto \frac{E_e}{(E_e + E_b)} f_i(E_e + E_b) dE_e \cos\phi \sin\phi d\phi$$

A.2.2.3

This result is obtained by conserving energy and transverse momentum as depicted in Fig. A.2.1. It follows that:

(i) Conserving Energy:

$$E_i = E_e + E_b$$

A.2.2.4

(ii) Conserving Transverse Momentum

$$v_i \sin\theta = v_e \sin\phi$$

A.2.2.5

i.e.,

$$E_i \sin^2\theta = E_e \sin^2\phi$$

or

$$E_i \sin\theta \cos\theta d\theta = E_e \sin\phi \cos\phi d\phi$$

Combining these gives the result for the external distribution of recoils from the internal flux as

$$f_i(E_i) dE_i \sin\theta \cos\theta d\theta = f_i(E_e + E_b) dE_e \frac{E_e}{(E_e + E_b)} \sin\phi \cos\phi d\phi$$

$$= \frac{E_e}{(E_e + E_b)^3} dE_e \sin\phi \cos\phi d\phi$$

A.2.2.6

$$= f_e(E) dE_e \sin\phi \cos\phi d\phi$$

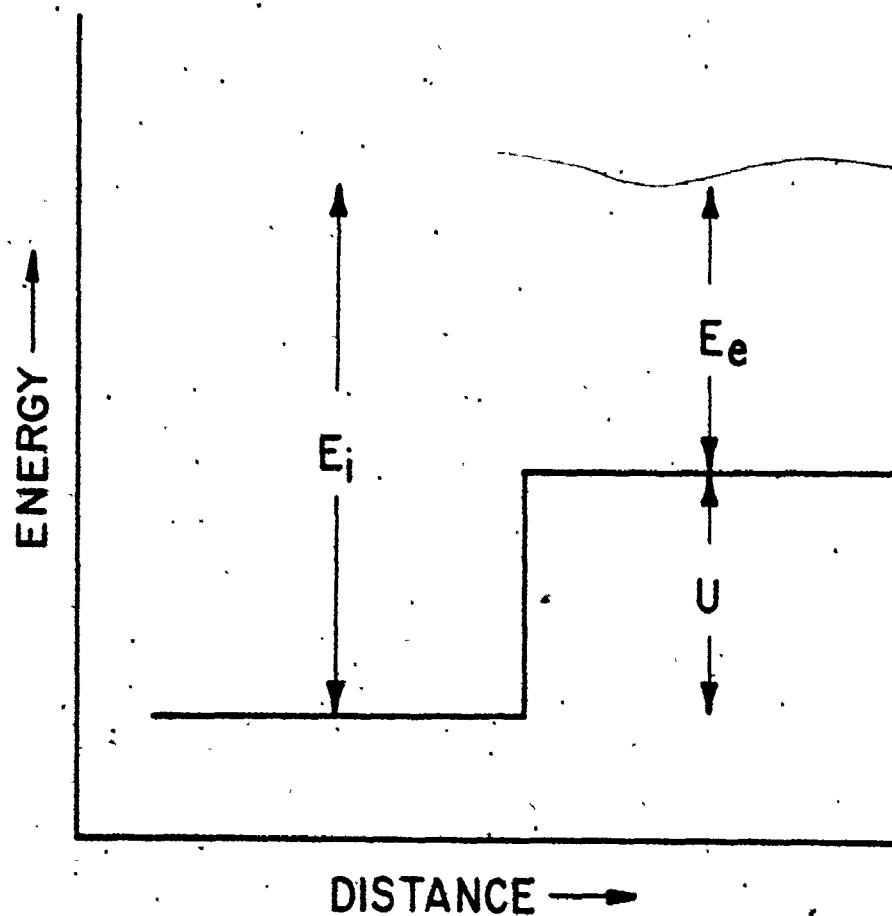


Figure A.2.1. Internal and external energy balance.

This is the result in eq. A.2.2.1, where the subscript for external, e , has been dropped.

It remains now to derive an expression for the surface normal distribution $f(E)$. Here, making use of $E = E_e \cos^2 \phi$, the surface normal distribution is

$$f(E) dE \cos \phi \sin \phi d\phi = \frac{E \cos^{-4}}{(E \cos^{-2} \phi + E_b)^3} dE \cos \phi \sin \phi d\phi. \quad A.2.2.7$$

By integrating over ϕ we get the required result for the surface normal energy distribution of sputtered recoils as

$$f(E) dE = \frac{1}{(E + E_b)^2} \quad A.2.2.8a$$

$$= \frac{1}{E^2} \quad A.2.2.8b$$

for $E \gg E_b$.

Finally it is of interest to note that we can construct a sputtering yield, S , through these functions using

$$S = C_0 \int_0^{\hat{E}} \int_0^{\pi/2} f_e(E_e) dE_e \cos \phi \sin \phi d\phi \quad A.2.2.9$$

REFERENCES TO CHAPTER 2

1. W.R. Grove, Phil. Trans. Roy. Soc., (1952) 82.
2. For a general review and data source see G. Carter and J. Colligon, Ion Bombardment of Solids, Heineman Educational Books Ltd., 1968.
3. J. Lindhard, M. Scharff and H. Schiøtt, Mat. Fys. Medd. Dan. Vid. Selsk., 33 (1963).
4. P. Sigmund, Phys. Rev., 184 (1969) 383.
5. E.B. Henschke, Phys. Rev., 106 (1957) 737.
6. D.T. Goldman and A. Simon, Phys. Rev., 111 (1958) 383.
7. H. Oechsner, Appl. Phys., 8 (1975) 185.
8. R. Kelly, Rad. Effects, 32 (1977) 91.
9. H.M. Naguib and R. Kelly, Rad. Effects, 25 (1975) 1.
10. C.A. Andersen and J.R. Hinthorne, Anal. Chem., 42 (1973) 121.
11. M.W. Thompson, Phil. Mag., 38 (1968) 377.
12. J. Politiek and J. Kistemaker, Rad. Effects, 2 (1969) 129.
13. W. Heiland, J. Kraus, S. Leung and N.H. Tolk, Surf. Sci., 67 (1977) 437.
14. G. Staudenmaier, Rad. Effects, 13 (1972) 87.
15. M.L. Olson and D.D. Konowalow, Chem. Phys. 21 (1977) 393.
16. M. Braun, Physica Scripta, 19 (1978) 234.
17. C.B. Kerkdijk, K.H. Scharfner, R. Kelly and F.W. Saris, Nucl. Instr. Meth., 132 (1976) 427.
18. C.J. Good-Zamin, M.T. Shehata, D.B. Squires and R. Kelly, Rad. Effects, 35 (1978) 139.
19. H.D. Hagstrum, in Physics of Ionized Gases, ed. B. Navinsek, 1970 p. 190.

20. R.A. Weller and T.A. Tombrello, Rad. Effects, 37 (1978) 83.
21. M. Abramowitz and I.A. Stegun, Handbook of Mathematical Functions, NBS Applied Mathematics Series-55, 1964.
- 22a. W.L. Wiese, M.W. Smith and B.M. Glenon, Atomic Transition Probabilities, Vol. I, NBS-4, 1966.
- 22b. W.L. Wiese, M.W. Smith and B.M. Miles, Atomic Transition Probabilities, Vol. II, NBS-4, 1969.
- 22c. B.M. Miles and W.L. Wiese, NBS-474, 1969.
23. A. Kraus and D.M. Gruen, Appl. Phys., 14 (1977) 89.
24. I.S.T. Tsong and N.A. Yusuf, Appl. Phys. Lett., 33 (1978) 999.
25. T. Andersen, K.A. Jessen and G. Sørensen, J. Opt. Soc. Am., 59 (1969) 1197.
26. L. Lundin, B. Engman, J. Hilke and I. Martinson, Physica Scripta, 8 (1973) 274.
- 27a. F.M. Kelly, T.K. Koh and M.S. Mathur, Can. J. Phys., 52 (1974) 795.
- 27b. F.M. Kelly, T.K. Koh and M.S. Mathur, Can. J. Phys., 52 (1974) 1438.
- 27c. F.M. Kelly, T.K. Koh and M.S. Mathur, Can. J. Phys., 52 (1974) 1666.
28. M.A. Rudat and G.H. Morrison, Int. J. Mass Spectrom. and Ion Physics, 30 (1979) 197.

CHAPTER 3

3. THE THEORY OF RECOIL IMPLANTATION AND SPUTTERING

3.1 INTRODUCTION

The theory of particle stopping in solids has as its roots the classic works by Lindhard, Scharff and Schiøtt (1), called LSS Theory and Winterbon, Sigmund and Sanders (2), called WSS Theory. In particular, their investigations led to approximations for the spatial distributions for damage (deposited energy) and for particles implanted into random solids. For instance, as shown in Chapter 2, section 2.1, the cascade sputtering yield, S , depended upon the distribution of deposited energy at the surface.

In this chapter we investigate the theory of recoil implantation and its corollary, recoil sputtering. By "recoil" we mean the direct transfer of energy (elastic) to target atoms which subsequently implant into the solid or rebound out of the solid. We develop depth distribution functions of the implanted species as well as estimate the sputtering yield due to recoil effects. In addition an attempt will be made to calculate the energy of a recoil sputtered atom and compare this to the observed energies as reported in the previous chapter. This correlation is a natural one since we believe that excited sputtered atoms have, as their collisional origin, surface recoil effects.

To this end a very brief review of ion implantation is required in order to extend the basic concepts to recoil phenomena. To facilitate

clarity, listed below are the basic quantities employed in the theory to follow:

M_1, M_2, M_3 = masses of the ion, recoil source, and target respectively

Z_1, Z_2, Z_3 = atomic numbers of the aforementioned

E_1 = initial ion energy

$T_2 = \frac{4M_1 M_2 E_1}{(M_1 + M_2)^2} \cdot \cos^2 \theta/2$ = recoil energy in a binary collision between an accelerated particle (M_1) and a struck particle (M_2) for a given scattering angle (θ)

$\hat{T}_2 = \gamma_{12} E_1$ = maximum transferred energy

$\gamma_{12} = \frac{4M_1 M_2}{(M_1 + M_2)^2}$

N = atomic number density

$C = \frac{\pi}{2} \lambda_m a^2 \left(\frac{M_1}{M_2} \right)^m \left(\frac{2Z_1 Z_2 e^2}{a} \right)^{2m}$

λ_m = parameter depending upon m , namely, $\lambda_{1/3} = 1.309$, $\lambda_{1/2} = 0.327$,

$\lambda_1 = 0.5$

m = parameter, typically 0, 1/3, 1/2 or 1 (see text)

$a = 0.8853 a_0 Z^{-1/3}$ = screening radius for a Thomas-Fermi encounter

a_0 = Bohr Radius = 0.529 Å

$Z^{2/3} = Z_1^{2/3} + Z_2^{2/3}$

e = electronic charge

In the interest of clarity we will relegate applications of recoil implantation and sputtering to Chapter 4.

3.2 THE FIRST GENERATION PROBLEM

We define the first generation problem as that for the stopping of ions in a random or amorphous solid through collisions with target atoms. In particular we will review in this section the spatial distribution of these ions along with the spatial extent of the deposited energy. (In general the term deposited energy is synonymous with elastic damage). An understanding of scattering or collision events of two isolated particles has been available since Bohr's classic work in 1948 (3). However, in atomic collision phenomena one deals with a rather large flux of incoming accelerated particles, of the order of 10^{16} ions/s, interacting with a rather large number of target atoms. In order to determine the spatial distributions of such a large number of events, statistical methods must be used. To such an end the quantity $d\sigma$, the differential scattering cross section is introduced. Specifically, $d\sigma$, describes the probability of an energy transfer T in dT in a two body collision and is given by

$$d\sigma = CE_1^{-m} T^{-1-m} dT, \quad (3.1)$$

for power-law scattering. The parameter m depends on ion energy and a brief discussion of its origin is given below. The amount of transferred energy lies in the interval $(0, \gamma_{12} E_1)$. For any transferred energy in this region we use the cross section, for averaging purposes, given by appropriate integration of eq. 3.1. For example, the mean transferred energy is just

$$\langle T_2 \rangle = \int T_2 d\sigma / \int d\sigma , \quad (3.2)$$

where σ is the total cross section, $\sigma = \int_0^{\gamma_{12} E_1} d\sigma$.

Of course, all scattering and hence collision events are ultimately based upon the choice of interatomic potentials between the colliding bodies. For example, the differential cross section in eq. (3.1) is based upon a Screened Coulomb Potential of the form

$$V(r) = \frac{Ze}{r} \phi(r/a) , \quad (3.3)$$

where r is the distance from the atom centre, Z its atomic number and $\phi(r/a)$ a screening function which describes the effect of the electrons on screening the nuclei. The screening function is shown in Fig. 3.1 (solid curve) for a Thomas-Fermi atom along with several power law approximations of the form

$$\phi(r/a) \approx \text{constant} \cdot x^{-s} , \quad (3.4)$$

where $x = r/a$. The figure gives various s values ranging from $1/2$ to 3 . The choice of s clearly depends upon the distance of approach in the binary collision, which in turn depends upon the accelerating energy, E_1 . For energies in the low keV region a good approximation is $s = 3$, for which $m \equiv 1/s = 1/3$. Throughout the majority of this work we will take $m = 1/3$.

Returning now to the first generation problem, as depicted

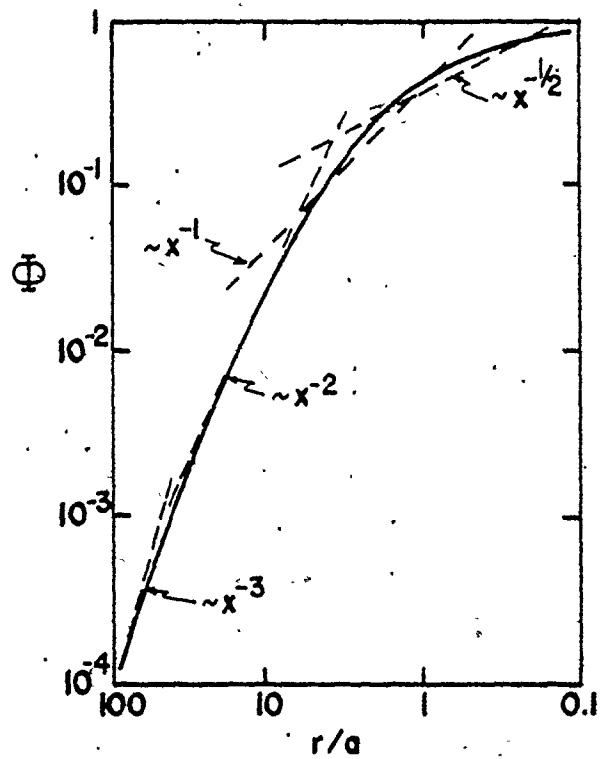


Figure 3.1. Power law approximations (dotted) to the screening function (solid). From ref. 4.

in Fig. 3.2, monoenergetic ions will implant into the target and will spatially distribute themselves according to the expansion

$$C^{(1)}(x)dx = \frac{dx}{(2\pi\mu_2)^{1/2}} \exp\left\{-\frac{\xi^2}{2}\right\} \cdot f(\xi), \quad (3.5)$$

where $\xi = \frac{x - \langle x \rangle}{\mu_2^{1/2}}$ and $\mu_n = \langle \Delta x^n \rangle = \langle (x - \langle x \rangle)^n \rangle$, with x being the spatial variable, $\langle x \rangle$ the mean, and Δx the straggling or width of the distribution. The function $f(\xi)$ is an expansion in terms of higher moments, however, in most applications it is taken as unity which, in that case, renders the distribution Gaussian. The general n moments of the distribution have been given by WSS theory (2) as

$$\langle x^n \rangle = \left\{ \frac{E_1^{2m}}{NC} \right\} \sum_{\ell} (2\ell + 1) A_{(1)\ell n} \cdot P_{\ell}(\cos\theta) \quad (3.6)$$

The functions $P_{\ell}(\cos\theta)$ are the Legendre Polynomials of order ℓ and θ is the angle of incidence with respect to the surface normal. Also, the functions $A_{(1)\ell n}$ are listed in Table 3.1 for $m = 1/3$ and various mass ratios. It should be pointed out that the form of the distribution in eq. 3.5 is applicable, in its generality, to the spatial extent of deposited energy. To this end, Table 3.2 lists the coefficients $A_{(1)\ell n}$ for deposited energy or, simply, damage.

The distribution function as written in eq. 3.5 is of differential form, however, it is often advantageous to write the distribution in integral form, namely

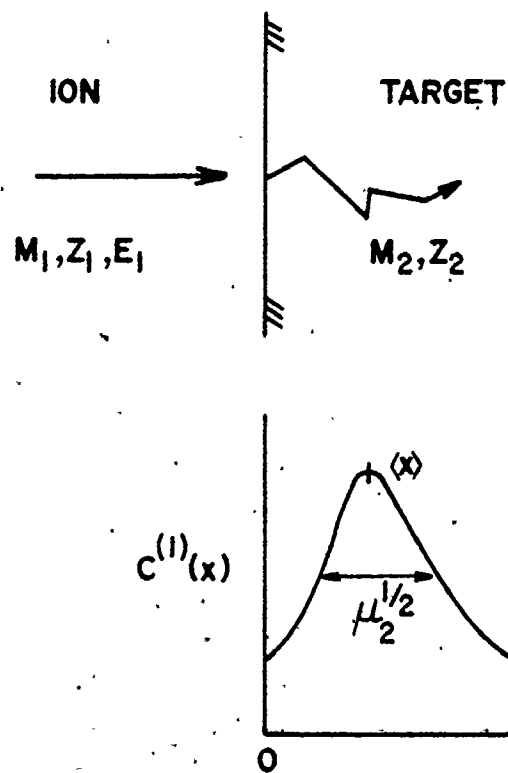


Figure 3.2. Schematic representation of ion implantation, defined in this work as the first generation problem.

Table 3.1

Coefficients $A_{(1)qn}$ for $m = 1/3$ for various mass ratios for range calculations. From ref. 2.

M_3/M_2	0.1	0.25	0.5	1.0	2.0	4.0	10.0
$A_{(1)00}$	1.000	1.000	1.000	1.000	1.000	1.000	1.000
$A_{(1)11}$	6.511×10^{-1}	3.821×10^{-1}	2.685×10^{-1}	1.991×10^{-1}	1.520×10^{-1}	1.170×10^{-1}	8.384×10^{-2}
$A_{(1)02}$	1.394	5.402×10^{-1}	3.123×10^{-1}	2.168×10^{-1}	1.768×10^{-1}	1.653×10^{-1}	1.795×10^{-1}
$A_{(1)22}$	5.226×10^{-1}	1.852×10^{-1}	9.388×10^{-2}	5.229×10^{-2}	3.046×10^{-2}	1.805×10^{-2}	9.315×10^{-3}
$A_{(2)13}$	1.795	4.523×10^{-1}	2.045×10^{-1}	1.166×10^{-1}	7.872×10^{-2}	5.945×10^{-2}	4.670×10^{-2}
$A_{(1)33}$	4.409×10^{-1}	1.009	3.747×10^{-2}	1.574×10^{-2}	6.995×10^{-3}	3.200×10^{-3}	1.194×10^{-3}
$A_{(1)04}$	4.194	7.552×10^{-1}	2.978×10^{-1}	1.626×10^{-1}	1.146×10^{-1}	9.926×10^{-2}	1.092×10^{-1}
$A_{(1)24}$	2.250	3.735×10^{-1}	1.314×10^{-1}	5.986×10^{-2}	3.206×10^{-2}	1.888×10^{-2}	1.060×10^{-2}
$A_{(1)44}$	4.318×10^{-1}	5.946×10^{-2}	1.631×10^{-2}	5.176×10^{-3}	1.758×10^{-3}	6.266×10^{-4}	1.682×10^{-4}

Table-3.2

Coefficients $A_{(1)gn}$ for $m = 1/3$ for various mass ratios for deposited energy calculations. From ref. 2.

M_3/M_2	0.1	0.25	0.5	1.0	2.0	4.0	10.0
$A_{(1)00}$	1.000	1.000	1.000	1.000	1.000	1.000	1.000
$A_{(1)11}$	3.776×10^{-1}	2.678×10^{-1}	2.123×10^{-1}	1.685×10^{-1}	1.338×10^{-1}	1.074×10^{-1}	8.056×10^{-2}
$A_{(1)02}$	6.347×10^{-1}	3.573×10^{-1}	2.382×10^{-1}	1.572×10^{-1}	1.142×10^{-1}	1.002×10^{-1}	1.055×10^{-1}
$A_{(1)22}$	2.078×10^{-1}	1.032×10^{-1}	6.468×10^{-2}	4.043×10^{-2}	2.529×10^{-2}	1.605×10^{-2}	8.842×10^{-3}
$A_{(1)13}$	6.364×10^{-1}	2.701×10^{-1}	1.468×10^{-1}	7.813×10^{-2}	4.742×10^{-2}	3.504×10^{-2}	2.764×10^{-2}
$A_{(1)33}$	1.387×10^{-1}	4.790×10^{-2}	2.359×10^{-2}	1.153×10^{-2}	5.632×10^{-3}	2.805×10^{-3}	1.127×10^{-3}
$A_{(1)04}$	1.359	4.911×10^{-1}	2.246×10^{-1}	9.911×10^{-1}	5.755×10^{-2}	4.713×10^{-2}	4.987×10^{-2}
$A_{(1)24}$	6.473×10^{-1}	2.046×10^{-1}	8.983×10^{-2}	3.815×10^{-2}	1.878×10^{-2}	1.111×10^{-2}	6.325×10^{-3}
$A_{(1)44}$	1.048×10^{-1}	2.507×10^{-2}	9.650×10^{-3}	3.662×10^{-3}	1.390×10^{-3}	5.413×10^{-4}	1.583×10^{-4}

$$C^{int.}(x) = \int_x^{\infty} C^{diff.} dx' . \quad (3.7)$$

For the Gaussian case this is just

$$S_i^{(1)} = \frac{1}{2} \operatorname{erfc} \left\{ \frac{x - \langle x \rangle}{(2\mu_2)^{1/2}} \right\} , \quad (3.8)$$

where $\operatorname{erfc}(z)$ is the complementary error function. The notation, $S_i^{(1)}$, is not the usual one but should be read as the number of ions implanted (hence the subscript i) per incident ion (hence the symbol "S", as if sputtering were being described) into a target (hence the superscript (1) for the first generation case). In addition to ion implantation, a fraction of the ions is found in front of the surface. The amount reflected is given by

$$S_s^{(1)} = \frac{1}{2} \operatorname{erfc} \left(\frac{\langle x \rangle}{(2\mu_2)^{1/2}} \right) . \quad (3.9)$$

Equations 3.8 and 3.9 describe a forward effect (implantation) and a backward effect (reflection) when a particle of mass M_1 strikes a target of mass M_2 .

The foregoing treatment has assumed the target to be amorphous and as will be shown, crystalline effects can play a prominent role in the spatial distribution of implanted particles.

3.3 THE SECOND GENERATION PROBLEM

3.3.1 Recoil Distribution Functions - Thin Sources

We now extend the concepts of the first generation problem to the case illustrated in Fig. 3.3, where a monoenergetic ion of mass M_1 strikes a target which contains a source of atoms of mass M_2 located at a depth x' in the target of mass M_3 . This thin source may take the form of an oxide on the surface or a vapor deposited layer. When the ion transfers some energy to a source atom, the struck atom recoils into the solid in a fashion much the same as in the first generation problem, however, its initial motion is over a wide range of angles, ψ . We calculate the depth distribution of these recoils measured along a direction normal to the surface. From the geometry in Fig. 3.3 this distance is

$$x = \xi \cos \psi - \eta \sin \psi, \quad (3.10)$$

where ξ is the depth of penetration along its initial trajectory, η the projected perpendicular straggling, and ψ the angle with respect to the surface normal.

As in the first generation problem, the random variables can be approximated by a Gaussian function for the recoil atom

$$E(\xi) d\xi = \frac{d\xi}{(2\pi\mu_2)^{1/2}} \exp \left\{ -\frac{(\xi - \langle \xi \rangle)^2}{2\mu_2} \right\}. \quad (3.11)$$

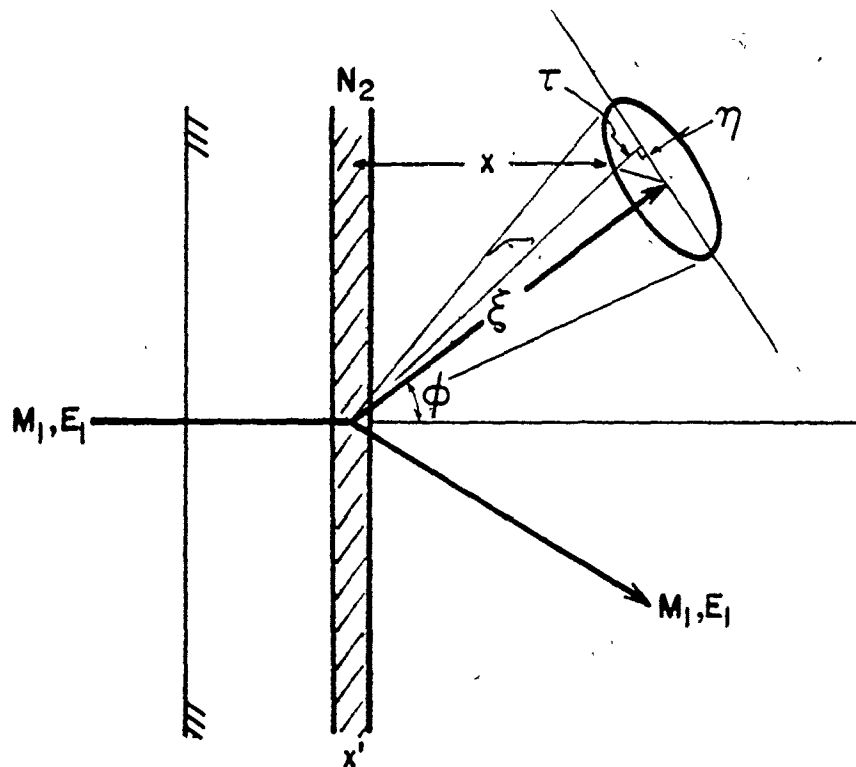
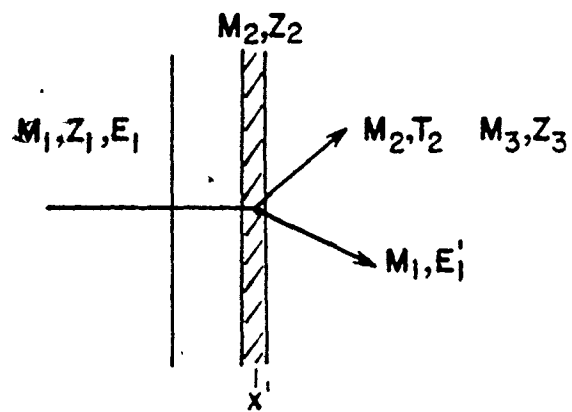


Figure 3.3 Schematic representation of recoil implantation, defined in this work as the second generation problem. Also shown are the statistical variables.

Again, the integral distribution is constructed to give the probability of a recoil source atom penetrating beyond a distance x as

$$F(x-x', w) = \frac{1}{2} \operatorname{erfc} \left\{ \frac{x-x' - \langle \xi \rangle w}{[2\mu_{2\xi} w^2 + 2\mu_{2\eta} (1-w^2)]^{1/2}} \right\} \quad (3.12)$$

Here the variable is $w = \cos\psi$. As pointed out earlier the statistical parameters $\langle \xi \rangle$, $\mu_{2\xi}$ and $\mu_{2\eta}$ can be determined from eq. 3.6 with the slight modification that E_1 is replaced by the transferred energy, T_2 . The moments are then simply

$$(i) \quad n=1 \quad \langle \xi \rangle = f_{23} T_2^{2m_{23}} \{N_3 C_{23}^{(m_{23})}\}^{-1} \quad (3.13a)$$

$$(ii) \quad n=2 \quad \mu_{2\xi} = g_{23} T_2^{4m_{23}} \{N_3 C_{23}^{(m_{23})}\}^{-2} \quad (3.13b)$$

$$(iii) \quad n=2 \quad \mu_{2\eta} = h_{23} T_2^{4m_{23}} \{N_3 C_{23}^{(m_{23})}\}^{-2} \quad (3.13c)$$

The terms f , g and h are simply the summation terms of eq. 3.6 and are listed in Tables 3.3a, b for both range and deposited energy as deduced from Tables 3.1 and 3.2 for the case $m = 1/3$.

Combining eqs. 3.13 and 3.12 yields the result

$$F(x-x', w) = \frac{1}{2} \operatorname{erfc} \left\{ \frac{(x-x')z^{-4m_{23}} - z}{F(g/h)} \right\}, \quad (3.14)$$

with the following definitions,

Table 3.3.

Summation coefficients f_{23} , g_{23} and h_{23} as defined through eq. 3.6 for range and deposited energy

(a) Range

M_3/M_2	f_{23}	g_{23}	h_{23}
0.1	1.953	0.192	0.0875
0.25	1.146	0.152	0.0772
0.5	0.806	0.133	0.0776
1	0.597	0.121	0.0861
2	0.456	0.121	0.101
4	0.351	0.132	0.120
10	0.251	0.163	0.156

(b) Deposited Energy

M_3/M_2	f_{23}	g_{23}	h_{23}
0.1	1.133	0.390	0.115
0.25	0.803	0.228	0.0993
0.5	0.637	0.156	0.0765
1	0.505	0.104	0.0561
2	0.401	0.0795	0.0509
4	0.322	0.0766	0.0601
10	0.242	0.0913	0.0834

$$r = \left\{ \frac{f_{23}}{(2h_{23})^{1/2}} \right\}^{4m_{23}} \left\{ \frac{x N_3 C_{23}^{(m_{23})}}{(2h_{23})^{1/2} (\gamma_{12} E_1)^{2m_{23}}} \right\} \quad (3.15a)$$

$$z = \frac{f_{23}}{(2h_{23})^{1/2}} \cdot w \quad (3.15b)$$

$$\text{and} \quad F(g/h) = [1 + (g_{23}/h_{23} - 1)w^2]^{1/2} \quad (3.15c)$$

For the case where a beam of ions strikes a recoil source, all transferred energies are permitted and the concentration profile of recoil source atoms is

$$H^{(2)}(x-x') = IN_2^{2/3} \int_{T_2}^{\gamma_{12} E_1} F(x-x', w) d\sigma_{12} \quad (3.16)$$

Here T_2 is a minimum transferred energy required to displace the recoil source atom and is of the order of 25 eV, I is the ion beam current.

✓ Taking a power law scattering cross section, eq. 3.16 can be written as

$$H^{(2)}(x-x') = \frac{IC_{12}N_2^{2/3}}{\gamma_{12}^{m_{12}}E_1^{2m_{12}}} \left(\frac{f}{(2h)} \right)^{1/2} \int_0^{\gamma_{12} E_1} z^{-1-2m_{12}} \cdot \text{erfc} \left\{ \frac{(r-r')z^{-4m_{23}} - z}{F(g/h)} \right\} dz \quad (3.17)$$

Putting this into units of recoil atoms/incident ion gives the final result for the depth distribution of recoils implanted beyond a depth x into the target (integral distribution) as

$$\begin{aligned}
 S_i^{(2)} &= \frac{H^{(2)}(x-x')}{I} \\
 &= \frac{C_{12}N_2^{2/3}}{\gamma_{12}^{m_{12}}E_1^{2m_{12}}} \left(\frac{f}{(2h)^{1/2}} \right)^{2m_{12}} \cdot I_i^{(2)}(x-x', M_3/M_2),
 \end{aligned}
 \tag{3.18a}$$

where

$$I_i^{(2)}(x-x', M_3/M_2) = \int_0^{f/(2h)^{1/2}} z^{-1-2m_{12}} \operatorname{erfc}\left\{ \frac{(x-x')z^{-4m_{23}} - z}{F(g/h)} \right\} dz.
 \tag{3.18b}$$

The integral in eq. 3.18b is parametrically dependent only upon the ratio of the target to recoil source masses, M_3/M_2 .

As in the first generation problem, we calculate the fraction of recoil sputtered atoms through

$$\begin{aligned}
 S_s^{(2)} &= \frac{H^{(2)}(-\infty) - H^{(2)}(-x')}{I} \\
 &= \frac{C_{12}N_2^{2/3}}{\gamma_{12}^{m_{12}}E_1^{2m_{12}}} \left(\frac{f}{(2h)^{1/2}} \right)^{2m_{12}} \cdot I_s^{(2)}(x', M_3/M_2),
 \end{aligned}
 \tag{3.19a}$$

where

$$I_s^{(2)}(x', M_3/M_2) = \int_0^{f/(2h)^{1/2}} z^{-1-2m_{12}} \operatorname{erfc}\left\{ \frac{x'z^{-4m_{23}} + z}{F(g/h)} \right\} dz.
 \tag{3.19b}$$

These results give a forward effect, recoil implantation, and its analogue, recoil sputtering, for atomically thin sources of recoils.

The integrals in eqs. 3.18b and 3.19b have been evaluated by computer and are shown in figs. 3.4 and 3.5 for various mass ratios.

Equations 3.18a and 3.19a can be used to construct recoil implantation profiles as will be shown in the next chapter. Whereas the foregoing have applied to thin sources an extension can be made to thicker sources provided we assume that the incident ion does not deviate significantly within the source itself, i.e., its trajectory is constant through the source.

3.3.2 Recoil Distribution Functions - Moderately Thick Sources

The case for moderately thick sources is developed by a summation of the thin source cases from some minimum to maximum source width. That is

$$\begin{aligned}
 S_i^{(2A)} &= \frac{1}{\lambda} \int_{r'}^{\hat{r}} H^{(2)}(x-x') dx' \\
 &= \frac{C_{12} \gamma_{12}^{2m_{23}-m_{12}} (2h)^{1/2}}{C_{23} E_1^{2m_{12}-2m_{23}}} \cdot \left(\frac{f}{(2h)^{1/2}} \right)^{2m_{12}-4m_{23}} \\
 &\quad \cdot I_i^{(2A)}(x-x', M_3/M_2) \quad (3.20a)
 \end{aligned}$$

where

$$\begin{aligned}
 I_i^{(2A)}(x-x', M_3/M_2) &= \int_0^{f/(2h)^{1/2}} z^{4m_{23}-1-2m_{12}} F(g/h) \cdot \\
 &\quad \text{ierfc}\left\{ \frac{(r-r')z^{-4m_{23}} - z}{F(g/h)} \right\} \quad (3.20b)
 \end{aligned}$$

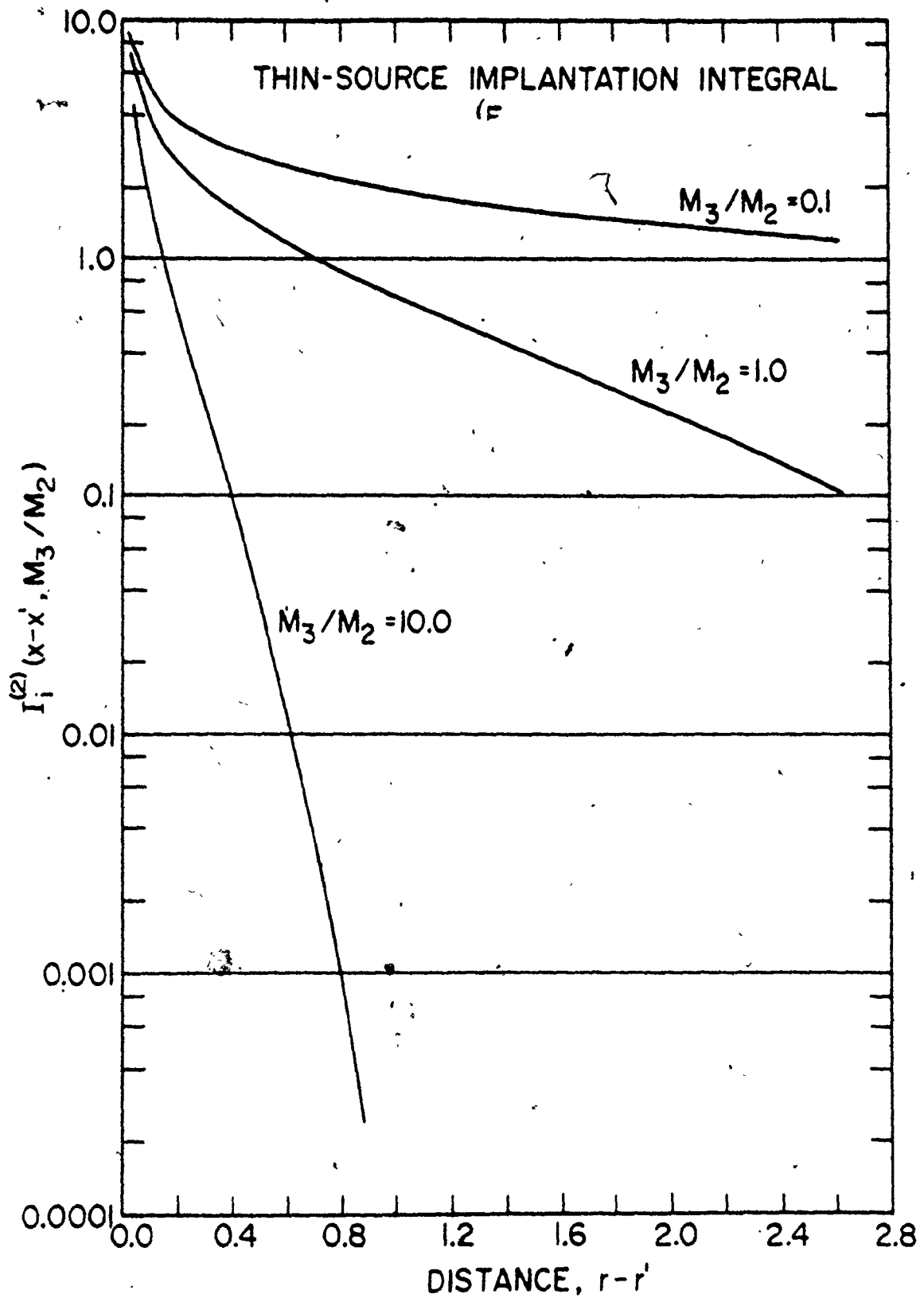


Figure 3.4. Recoil implantation integral evaluated by computer for $m_{12}=m_{23}=1/3$ as given by eq. 3.18b.

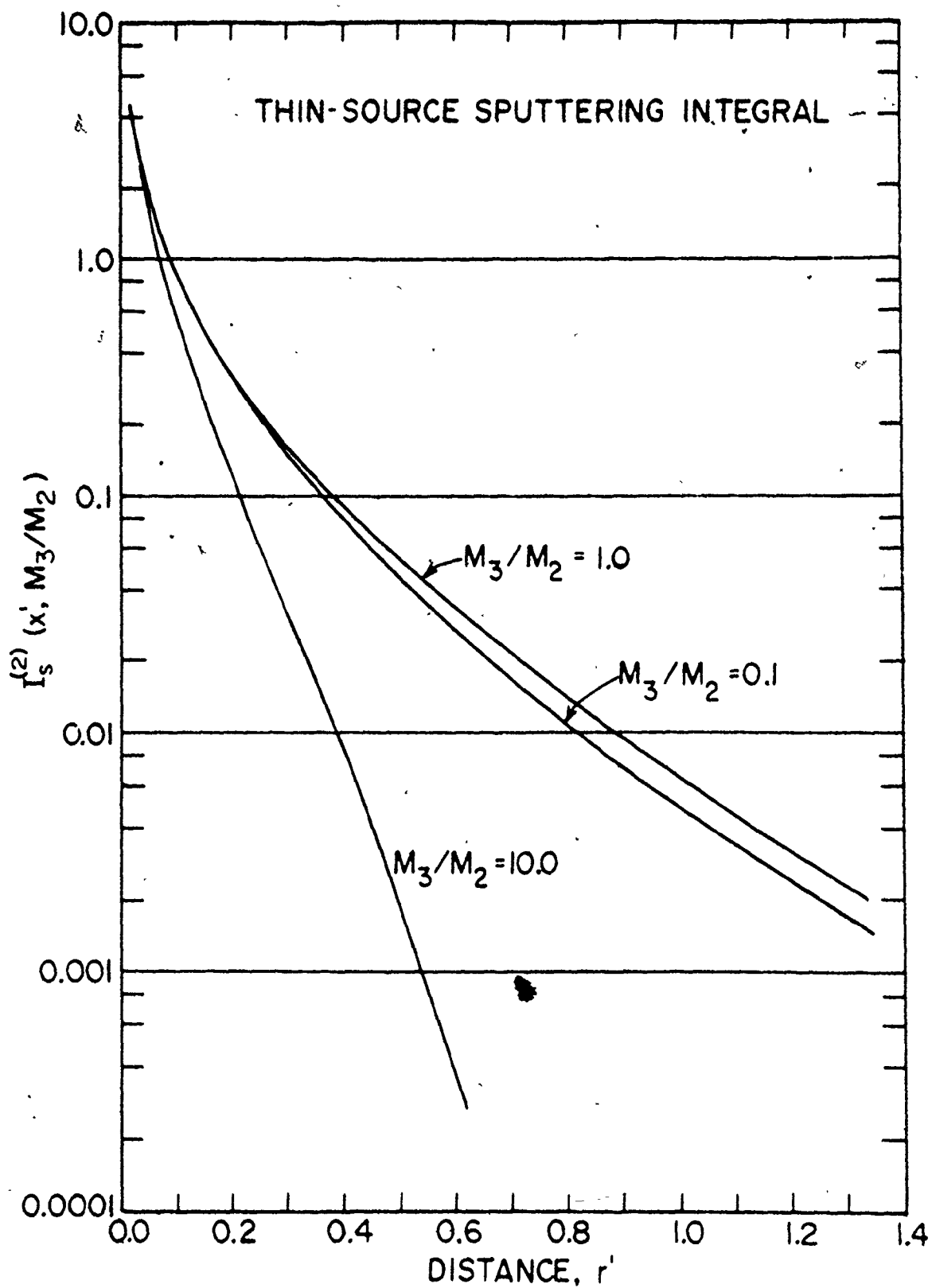


Figure 3.5. Recoil sputtering integral as given by eq. 3.19b.

for recoil implantation from a thick source. In addition, a thick source sputtering yield can be obtained as

$$\begin{aligned}
 S_s^{(2A)} &= \frac{1}{\lambda} \int_{\tilde{r}_1}^{\tilde{r}_1'} \{H^{(2)}(-\infty) - H^{(2)}(-x')\} dx' \\
 &= \frac{C_{12} \gamma_{12}^{2m_{23}-m_{12}} (2h)^{1/2}}{C_{23} E_1^{2m_{12}-2m_{23}}} \cdot \left(\frac{f}{(2h)^{1/2}} \right)^{2m_{12}-4m_{23}} \\
 &\quad \cdot I_s^{(2A)}(x', M_3/M_2)
 \end{aligned} \tag{3.21a}$$

where

$$\begin{aligned}
 I_s^{(2A)}(x', M_3/M_2) &= \int_0^{f/(2h)^{1/2}} z^{4m_{23}-1-2m_{12}} \cdot F(g/h) \\
 &\quad \cdot \text{ierfc}\left\{ \frac{r'z^{-4m_{23}} + z}{F(g/h)} \right\} dz
 \end{aligned} \tag{3.21b}$$

As before, the integrals have been evaluated and are given in figs. 3.6 and 3.7 for various mass ratios. Results for implantation profiles and sputtering yields are analogous to cases for thin sources.

Of particular interest in what is to follow, the integrals for thick source cases evaluated at the surface, i.e., $I_s^{(2A)}(0, M_3/M_2)$ have been calculated for $m = 1/3$ and are given in Table 3.4. When these values are put into eq. 3.21a along with the pre-integral term then a recoil sputtering yield in units of atoms/incident ion is obtained.

3.3.3 Recoil Sputtered Energies

In so far as the mechanism for secondary photon emission has

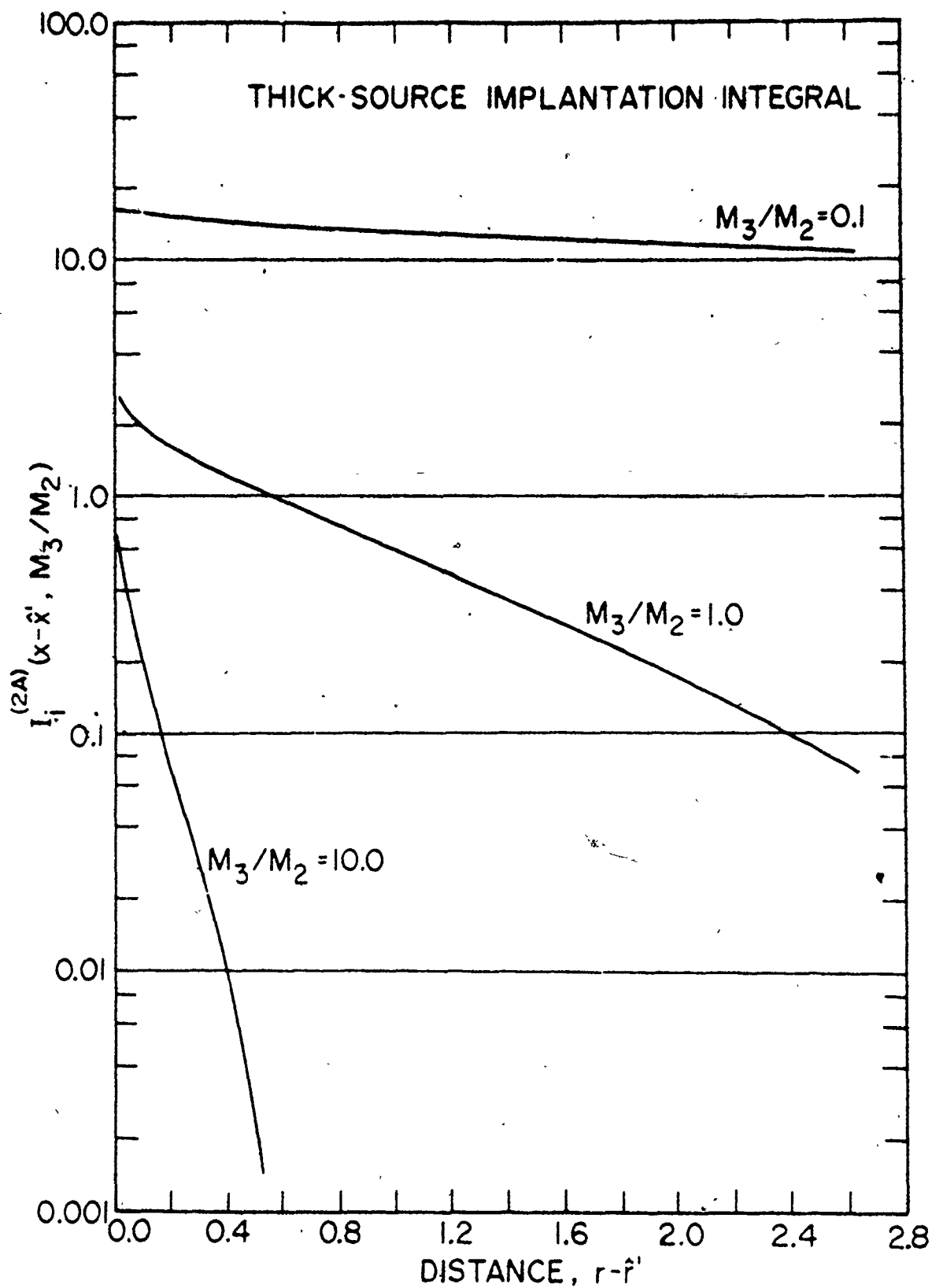
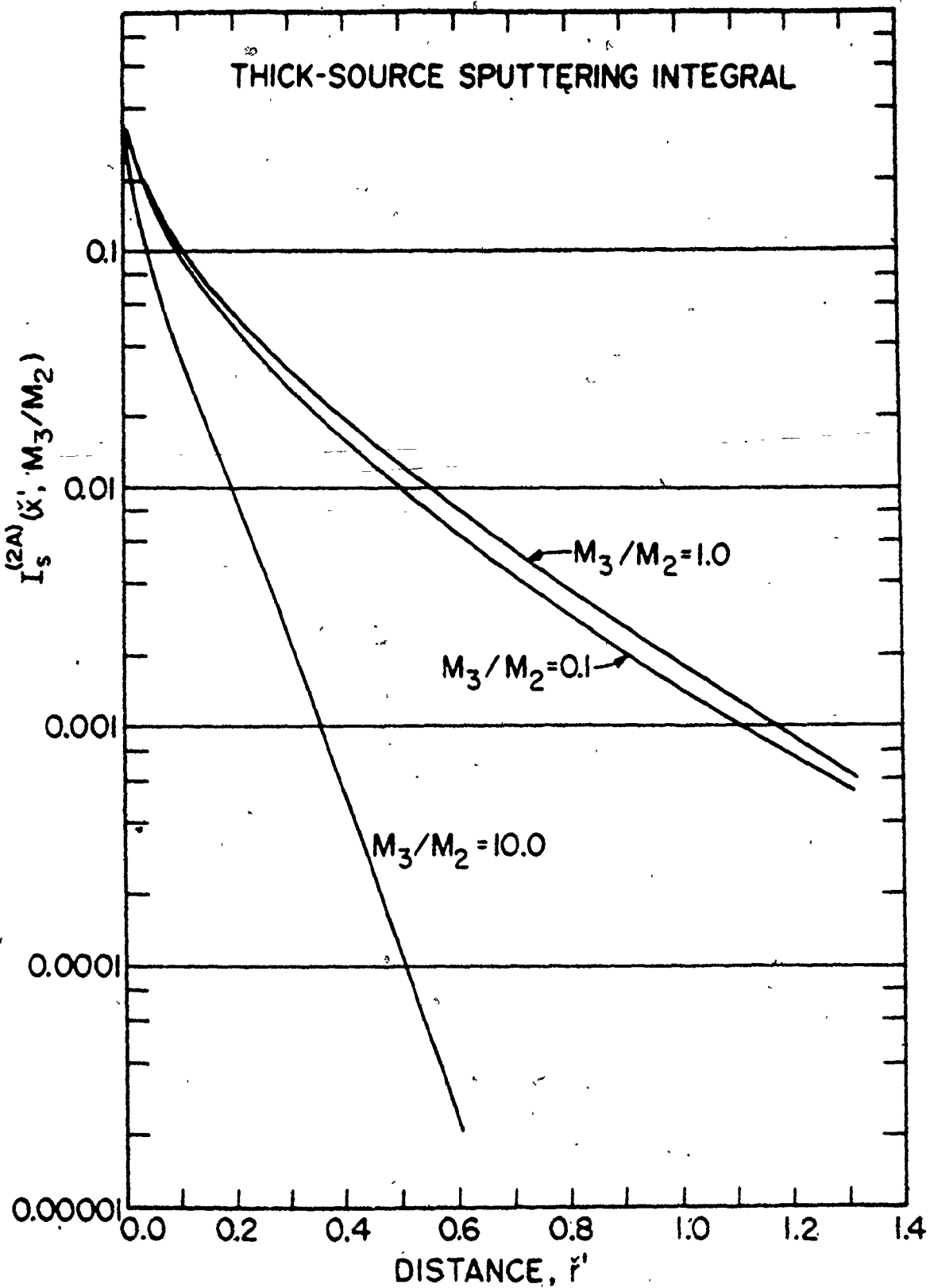


Figure 3.6. Recoil implantation integral as given by eq. 3.20b.



• Figure 3.7. Recoil sputtering integral as given by eq. 3.21b.

been proposed to involve recoil events, we now calculate the energy of such a recoil sputtered atom. The previous formalism can be extended to the deposited energy calculation at the surface by constructing the appropriate integral for the mean energy of an escaping recoil atom (cf. eq. 3.2). Referring to eq. 3.22 and putting $m_{12}=m_{23}=1/3$ we obtain the result

$$\begin{aligned} \langle E/N \rangle &= \frac{E_1 C_{12} \gamma_{12}^{1/3} (2h)^{5/6}}{S_s^{(2A)} C_{23} f^{2/3}} \int_0^{f/(2h)^{1/2}} \frac{T_2}{E_1} z^{-1/3} F(g/h) \text{ierfc}\{ \\ &\quad z/F(g/h) \} dz \\ &\equiv \frac{S_{sd}^{(2A)}}{S_s^{(2A)}} \cdot E_1 \end{aligned} \quad (3.22)$$

where $S_{sd}^{(2A)}$ represents the total energy deposited outside the surface.

The calculation of this quantity follows directly from the use of

eq. 3.13 appropriate for deposited energy. Using the fact that

$$T = \gamma_{12} w^2 E_1 \text{ then}$$

$$S_{sd}^{(2A)} = \frac{C_{12} \gamma_{12}^{4/3} (2h)^{11/6}}{C_{23} f^{8/3}} \int_0^{f/(2h)^{1/2}} z^{5/3} F(g/h) \text{ierfc}(z/F(g/h)) dz \quad (3.23)$$

for the thick source case. It must be pointed out that the values for f , g and h in eq. 3.23 are those for deposited energy, i.e., Table 3.3b.

This final expression will prove valuable in comparing the sputtered kinetic energies of recoils compared to sputtered atoms from a cascade or thermal spike model.

Table 3.4

Recoil sputtering integral

$I_s^{(2A)}(0, M_3/M_2)$ for $m=1/3$.

M_3/M_2	$I_s^{(2A)}(0, M_3/M_2)$
0.1	0.4612
0.25	0.4701
0.5	0.4766
1	0.4721
2	0.4535
4	0.4227
10	0.3652

3.4 CONCLUSIONS

Analogous to ion implantation, here defined as the first generation problem, we have developed equations which describe a forward effect and a backward effect for a particle which recoils in a target.

The forward effect, recoil implantation, results when a primary ion strikes a source atom which subsequently implants into the target. The spatial distribution of such recoils was developed using a power law scattering cross section and is given by eq. 3.18(a) for thin sources and eq. 3.20a for thick sources for $m_{12}=m_{23}=1/3$. Figures 3.4 to 3.7 facilitate the calculations.

The backward effect, recoil sputtering, occurs when the source atom is found to leave the solid. The number of such atoms is given by evaluating the recoil sputtering equations (eqs. 3.19a and 3.21a) at $x=0$.

Finally by taking the ratio of the deposited energy outside the solid to the yield of sputtered recoils gives a measure of the mean sputtered energy.

Applications of the above concepts will be given in Chapter 4.

REFERENCES TO CHAPTER 3

1. J. Lindhard, M. Scharff and H. Schiøtt, Mat. Fys. Medd. Dan. Vid. Selsk., 33 (1963).
2. K.B. Winterbon, P. Sigmund and J.B. Sanders, Mat. Fys. Medd. Dan. Vid. Selsk., 37 (1973).
3. N. Bohr, Mat. Fys. Medd. Dan. Vid. Selsk., 18 (1948).
4. P. Sigmund, Rev. Roum. Phy., 17 (1972) 823, 969, 1079.

CHAPTER 4

4. APPLICATIONS OF RECOIL IMPLANTATION AND SPUTTERING

4.1 INTRODUCTION

As mentioned in the introduction to this investigation, recoil phenomena may play a role in several, hitherto unexplained, effects concerning ion-surface interactions. Firstly, we have proposed that the creation of excited states may have as its origin recoil sputtering in which large energies are transferred. Secondly, recoil implantation may find application in doping processes and, related to this, may be the cause of observed long time transients in secondary photon yields. Thirdly, recoil effects are proposed to be contributing factors in chemical compositional changes during ion bombardment.

Each of these topics will be discussed and an effort made to relate them, where possible, to previous findings, both in this work and in that from the literature.

4.2 RECOIL SPUTTERING

Chapter 3 was devoted to developing solutions for the yield of recoil sputtered atoms as a result of ion bombardment. Equation (3.20) gives the number of recoil sputtered atoms per incident ion from a thin source located at a depth x' in the solid, while eq. (3.22) gives the analogous quantity for moderately thick sources. Figure 4.1 shows an example of the sputtering yield of oxygen from Al bombarded with Xe ions

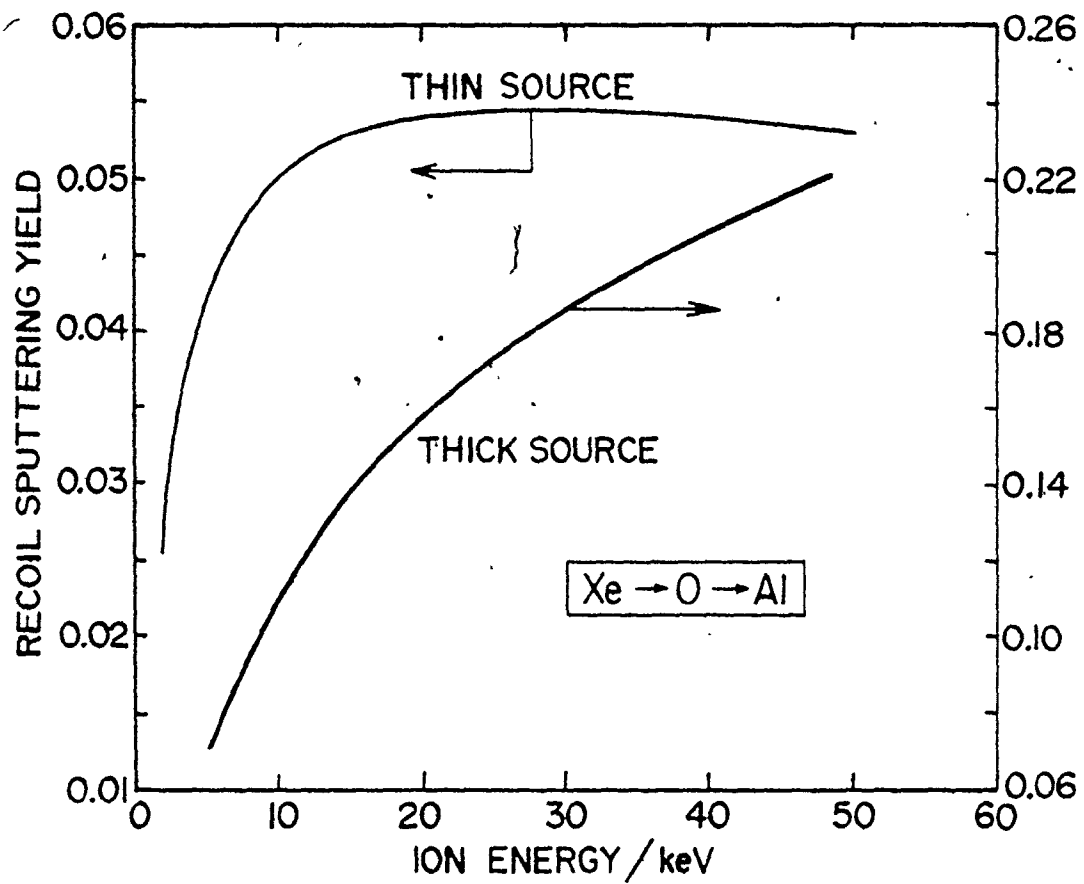


Figure 4.1. Recoil sputtering yields of oxygen from aluminum.

as a function of ion energy. Yields of the order of 0.05 recoils/incident ion are obtained from thin sources while yields of the order of 0.26 recoils/incident ion are seen with thicker sources. If these yields are compared to those for cascade sputtering, typically 5 atoms/incident ion, one finds a much lower overall yield.

Of particular interest, however, is the average energy of such a recoil as given by

$$\langle E/N \rangle = \frac{S_{sd}^{(2A)}}{S_s^{(2A)}} \cdot E_1, \quad (4.1)$$

namely the ratio of the deposited energy outside the surface to the total number of recoil sputtered atoms. Using eqs. (3.22) and (3.24), and eq. (4.1) the mean energy per recoil sputtered atom is easily shown to be

$$\langle E/N \rangle = 12 \frac{f_r^{2/3}}{f_d^{8/3}} \cdot \frac{(2h_d)^{11/6}}{(2h_r)^{5/6}} \cdot \frac{I_{sd}^{(2A)}(0, M_3/M_2)}{I_s^{(2A)}(0, M_3/M_2)}. \quad (4.2)$$

In this result, for thick sources, the subscripts r and d refer to range and deposited energy, respectively. The integrals $I_{sd}^{(2A)}$ for deposited energy and $I_s^{(2A)}$ for range have been evaluated at the surface and are listed in Table 4.1. The moments f and h are found in Table 3.3. With this data, Table 4.2 lists various cases for the calculated mean sputtered energy per atom for various targets. As seen, these energies are, in comparison, much greater than those that typify the random collision cascade sputtered atom, namely much greater than the surface

Table 4.1

Thick source recoil integrals evaluated
at the surface for $m = 1/3$.

M_3/M_2	$I_s^{(2A)}$	$I_{sd}^{(2A)}$
0.1	0.46122	0.22338
0.25	0.47007	0.14112
0.5	0.47668	0.12138
1	0.47213	0.10686
2	0.45347	0.081742
4	0.42276	0.051514
10	0.36516	0.023541

Table 4.2

Calculated recoil sputtered energies for
12 keV Kr^+ bombardments.

Source	Target	γ_{12}	$\langle E/N \rangle$, eV.
Li	LiF	0.2840	239
Mg	MgF_2	0.6913	646
Ca	CaF_2	0.8741	1162
Sr	SrF_2	0.9998	1329

binding energy. The striking correlation between these calculated energies and those energies deduced for excited states (cf. Table 3.) lead us to believe that excitation has as its origin recoil sputtered atoms. The size argument as previously discussed lends further credence to this conclusion.

As for experimental observations of such high energy particles, Reid et al. (1) have found large sputtering yields, i.e., peaks in a time of flight spectra situated at approximately 1000 eV for 20 keV Ar⁺ bombardment of Au which they attribute to recoil phenomena. This relatively high energy leads to a small fraction ($\sim 10^{-2}$) of atoms with such an energy, which could explain the reason for the yield of secondary photons being much less than the yields of secondary ions.

Continuing along these lines, the question arises as to what extent the random collision cascade high energy tail contributes to the yield of high energy particles. The normalized integral flux for the random cascade model is

$$N(E) = \frac{2EE_B + E_B^2}{(E + E_B)^2} \quad (4.3)$$

and for E in the range 240-1330 eV (cf. Table 4.2 for Li and Sr) the high energy yields are in the range 0.034-0.0075 atoms/ion. However, this is an order of magnitude less than the yield of recoil atoms, namely $S_s^{(2A)} = 0.26$ atoms/ion for thick sources. We interpret this result as indicating two features. Firstly, in the present context, recoil sputtered atoms are more important than high energy cascade atoms as a source of excited particles. Secondly, in a more general sense, recoil

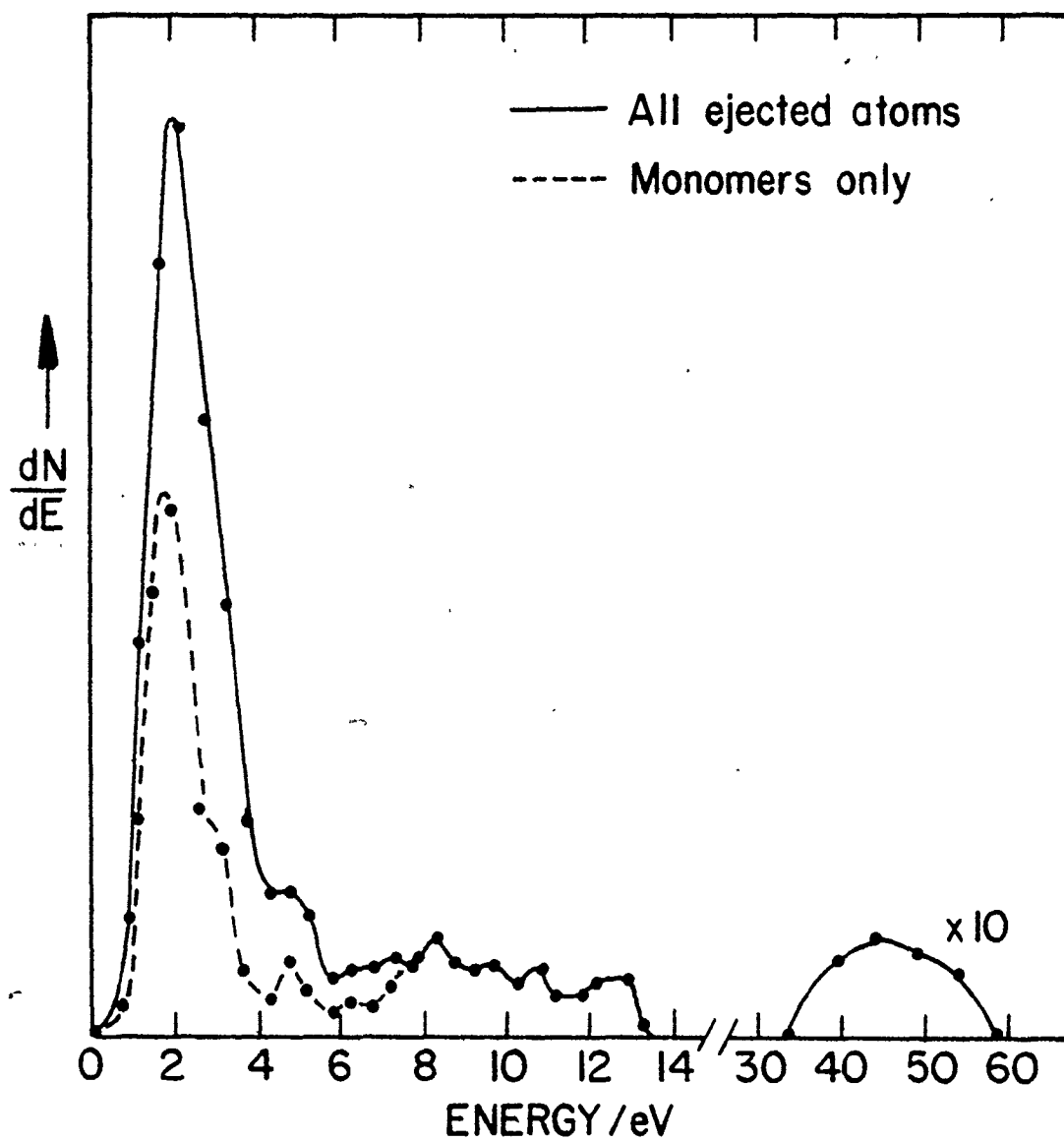


Figure 4.2. Computer simulation of the energy spectra of sputtered atoms. From ref. 2.

sputtering is an additive quantity to the cascade yield, such that it increases the high energy yield. This second point is verified in Harrison's (2) computer simulation studies on sputtering as reproduced in Fig. 4.2 where a high energy contribution to the overall yield is shown. We interpret this excess as due to sputtered recoils.

4.3 RECOIL IMPLANTATION

The incorporation of electrically active dopants into Si has of course led to a new frontier in electronics, however, methods to implant impurities still remain exploratory, particularly in the area of damage annealing.

The use of recoil implantation facilitates a wider range of dopant materials since the beam can be an inert gas which recoils dopants into the target. Figure 4.3 shows the calculated depth distribution of oxygen into tungsten for three Kr^+ energies. As to be expected the higher energy renders a deeper penetration of the dopant as obtained through eq. (3.19). The advantage in using recoil implantation lies in the ready availability of inert-gas-atom beams, thus avoiding complicated and expensive ion sources for such compounds as BF_3 for B doping into Si. Also, Fig. 4.4 illustrates the effect of the ion mass on the distributions of oxygen recoiled into tungsten at 5 keV.

Further we propose that transients in photon signals may be due to such recoil implantation effects. For instance the transients in Fig. 1.3 are obtained from Al by varying the oxygen partial pressure in the collision chamber. Initially, a steady state signal is maintained for approximately 4 min. then the oxygen pressure is increased by a

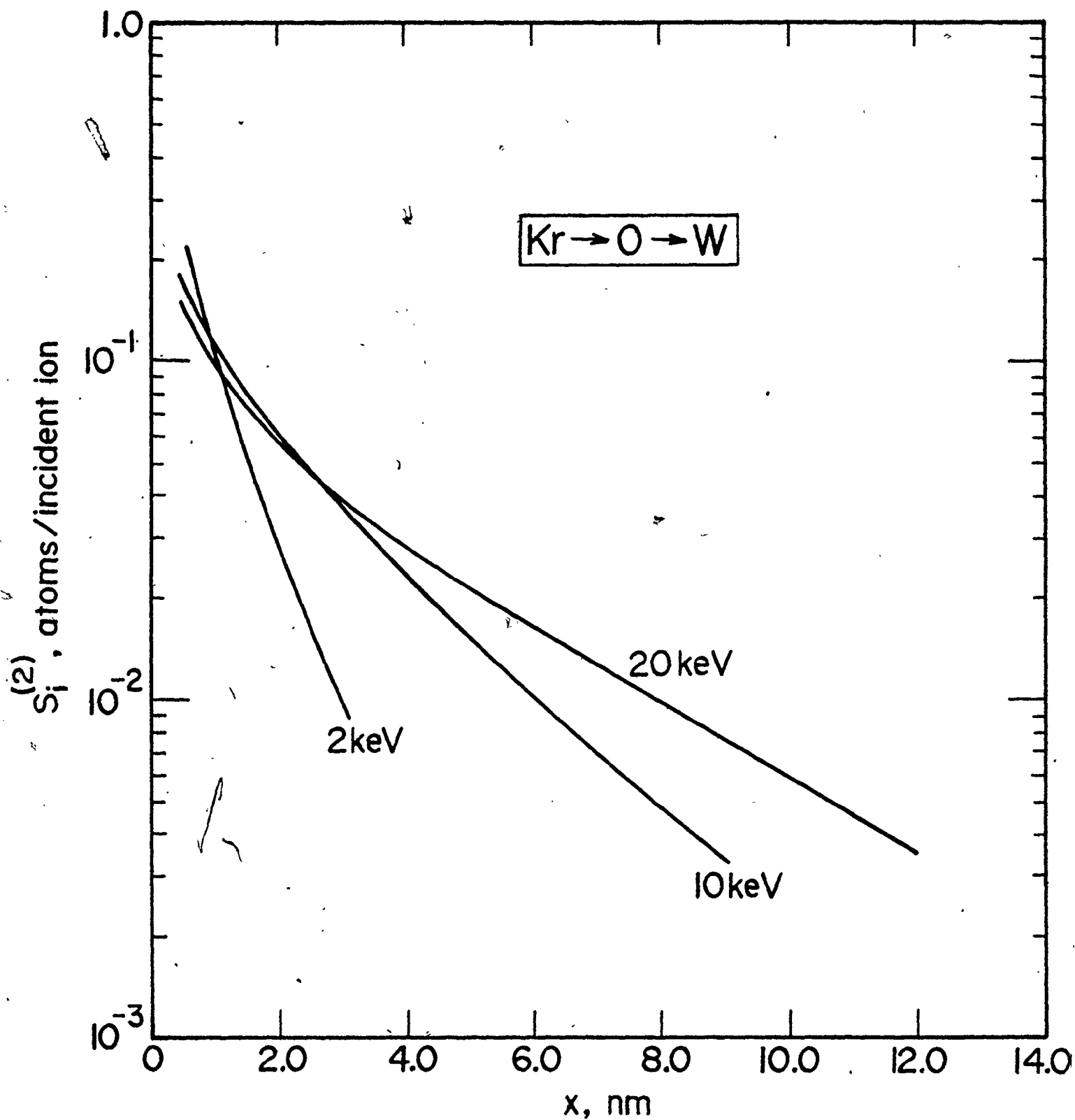


Figure 4.3. Recoil implantation distribution of oxygen in tungsten for three ion energies.

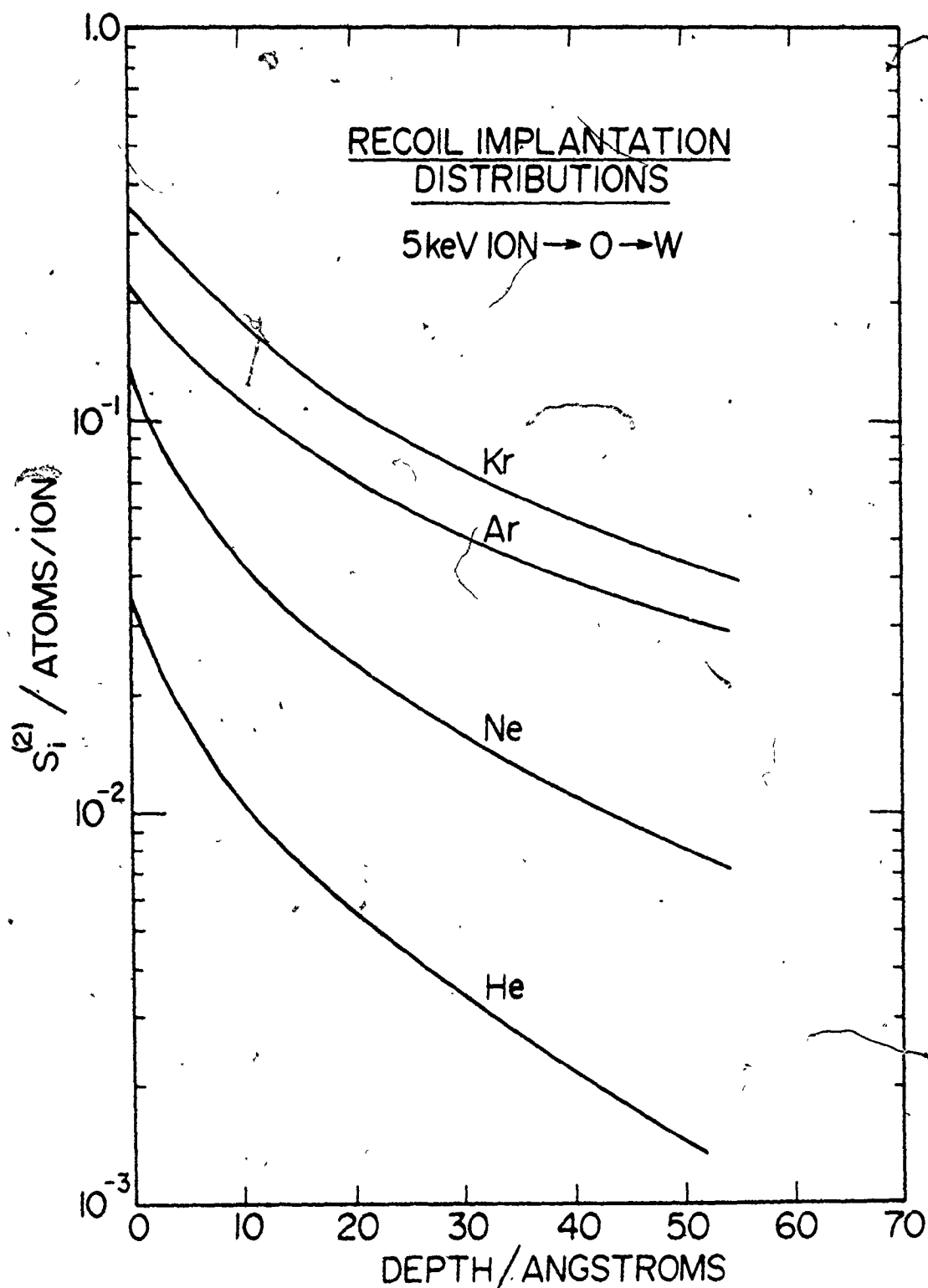


Figure 4.4. The effect of ion mass on the recoil implantation distribution of oxygen in tungsten.

factor of 80. The response time to reach a steady state signal at the higher pressure is of the order of 10 mins. The partial pressure of oxygen is then reduced back to 1.0×10^{-6} ton with an accompanying long time transient. These effects can be rationalized as due to surface oxygen being recoiled implanted into the target by the primary ion.

In addition, our own investigations on a Ni-2% Be oxidized alloy, as in Fig. 2.9, show a transient that may be in part due to the grown oxide being recoiled implanted into the alloy during sputtering, giving rise to a rather broad photon signal as a function of time. However, the origin of such straggling may also be due to poor quality of the beam areal density.

As a final example, Wittmack (3) has monitored the secondary ion yields from Si as reproduced in Fig. 4.5. He also finds a long time transient after the oxygen pressure is reduced (time=0 in Fig. 4.5) which we interpret as being due to sputter removal of recoil-implanted oxygen.

4.4 PREFERENTIAL EFFECTS

With the advancing use of accelerated particle beams used in surface analysis as, for example, in Auger Electron Spectrometry (AES) and Secondary Ion Mass Spectrometry (SIMS), problems arise associated with preferentiality during sputtering. For example, it has been well known that during bombardment, compound targets are often enriched in the heavier component, i.e., there is a preferential loss of the light element. (4,5)

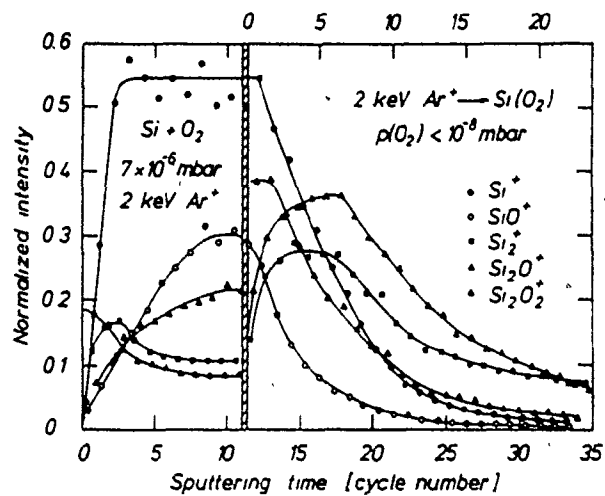


Figure 4.5. Transient secondary ion yields from SiO_2 . From ref. 3.

Calculations based on total yields of sputtered and implanted species are shown in Table 4.3. From these data several generalities emerge:

- (i) If the recoil source atom is light (compared to the target mass), it undergoes significant straggling and is implanted and sputtered to comparable extents. For example, for the case of $25 \rightarrow 10 \rightarrow 100$ in Table 4.3, it is seen that the thick source implanted yield is 0.075 atoms/incident ion while the sputtered yield is 0.051 atoms/incident ion.
- (ii) If the source atom is heavy, it undergoes insignificant straggling and is recoil implanted to a far greater extent than sputtered. For example, for $25 \rightarrow 100 \rightarrow 100$ the implanted and sputtered yields are, respectively, 0.098 and 0.0012.
- (iii) In the presence of a mixed target, it follows from (i) and (ii) that the target will become enriched in the heavier component.

Such preferential effects have been well known, however, their origins may have many sources such as surface binding energy effects and diffusional effects. It is not the intention to debate all effects but rather simply to add a recoil effect to the list.

4.5 CONCLUSIONS

We have developed solutions to recoil phenomenon based on a collisional model which give depth distributions for recoil implanted species as well as yields of recoil sputtered atoms. These yields are shown to be approximately an order of magnitude less than the yields from a random cascade model. The striking feature, however, is that the

Table 4.3

Numerical examples of recoil implantation and sputtering.

(Example: 25→10→100 means $M_1=25$ impacting on $M_2=10$ which in turn slows down in $M_3=100$. The evaluations were done for $N=0.06 \text{ \AA}^{-3}$, $m_{12}=m_{23}=1/3$, $Z_i=1/2 M_i$ (where Z_i is the atomic number), $E_1=10 \text{ keV}$ and $x-x' = x' = x-\hat{x}' = x' = 0.5 \text{ nm}$).

	value for 25→10→100	value for 25→100→100	value for 25→10→10	value for 25→100→10
$S_i^{(2)}$	0.075	0.030	0.097	0.077
$S_s^{(2)}$	0.051	0.0013	0.028	0.000
$S_i^{(2A)}$	0.79	0.098	1.1	0.75
$S_s^{(2A)}$	0.33	0.0012	0.096	0.000

recoil sputtered atom is characterized by a relatively high energy, of the order $10^2 - 10^3$ eV, and the yields for such energies are an order of magnitude larger than the yields from a random cascade model.

Calculations have shown that preferential effects may be due, in part, to recoil phenomenon where there is a preferential sputtering of the lighter component in a compound target.

REFERENCES TO CHAPTER 4

1. I. Reid, B.W. Farmery and M.W. Thompson, Nuc. Instr. Meth., 132 (1976) 317.
2. B.J. Garrison, N. Winograd and D.E. Harrison, J. Chem. Phys., in press.
3. K. Wittmack, Nucl. Instr. Meth., 68 (1977) 118.
4. H.H. Andersen, J. Vac. Sci. Tech., 16 (1979) 770.
5. D.K. Murti and R. Kelly, Thin Solid Films, 33 (1976) 149.

CHAPTER 5

5. THE FATE OF THE PRIMARY ION

5.1 INTRODUCTION

Previous chapters have focused on the sputtering process as a result of ion bombardment; in effect, we considered the fate of the struck atoms. In this chapter, attention is placed on the fate of the primary ions as affected by thermal effects, namely, diffusion and thermal release. The processes to be discussed are of importance in radiation damage problems as in nuclear reactor cladding materials where a portion of the fission/fusion products are inert gas-atoms.

This investigation is based upon isothermal anneals of implanted Kr^+ coupled with an anodic oxidation microsectioning technique and in addition, thermal release rate experimentation.

We wish to point out that the results to follow are in striking contrast to the previous chapters. The contrast, and complexities, is a natural one resulting from the method of experimentation and analysis. The atoms or particles which are sputtered can be studied on a much more refined scale since they can be considered as free, isolated species in vacuum and hence can be examined directly. This is to be compared to the results presented in the following chapter where the ions are buried within the solid and their examination can only come about through indirect means.

5.2 DIFFUSION PROFILES

A monoenergetic ion beam will implant into a target in a distribution which is approximately Gaussian (cf. section 3.2). This calculated distribution is based upon an amorphous or random target. Figure 5.1 shows the measured initial room temperature implantation profiles of Kr^+ in polycrystalline vanadium.

These distributions were measured by an anodic oxidation microsectioning technique, first developed for vanadium by Arora and Kelly (1). Basically, an oxide film is anodically grown in an electrochemical cell at a preset applied voltage and current. The electrolyte used in this work was a solution of glacial acetic acid such that each litre of solution contained 0.02 moles of $Na_2B_4O_7 \cdot 10 H_2O$ and 1.0 moles of additional H_2O . Once the film is grown, it is dried and then stripped off in a solution of dilute KOH. From gravimetric measurements the weight of metal removed is obtained and correlated with the applied voltage to obtain a calibration for metal removed versus voltage. Such a process gives a calibration of the form:

$$\text{metal removed} = 5.5 + 0.64 V \mu g/cm^2$$

where V is the applied potential in volts. For example, an applied voltage of 10 volts leads to an amount of metal removal equal to 11.9 $\mu g/cm^2$ or a 20 nm depth of vanadium. Repeating the procedure provides a microsectioning technique for diffusion analysis.

The depth distributions in Fig. 5.1 were obtained in this fashion

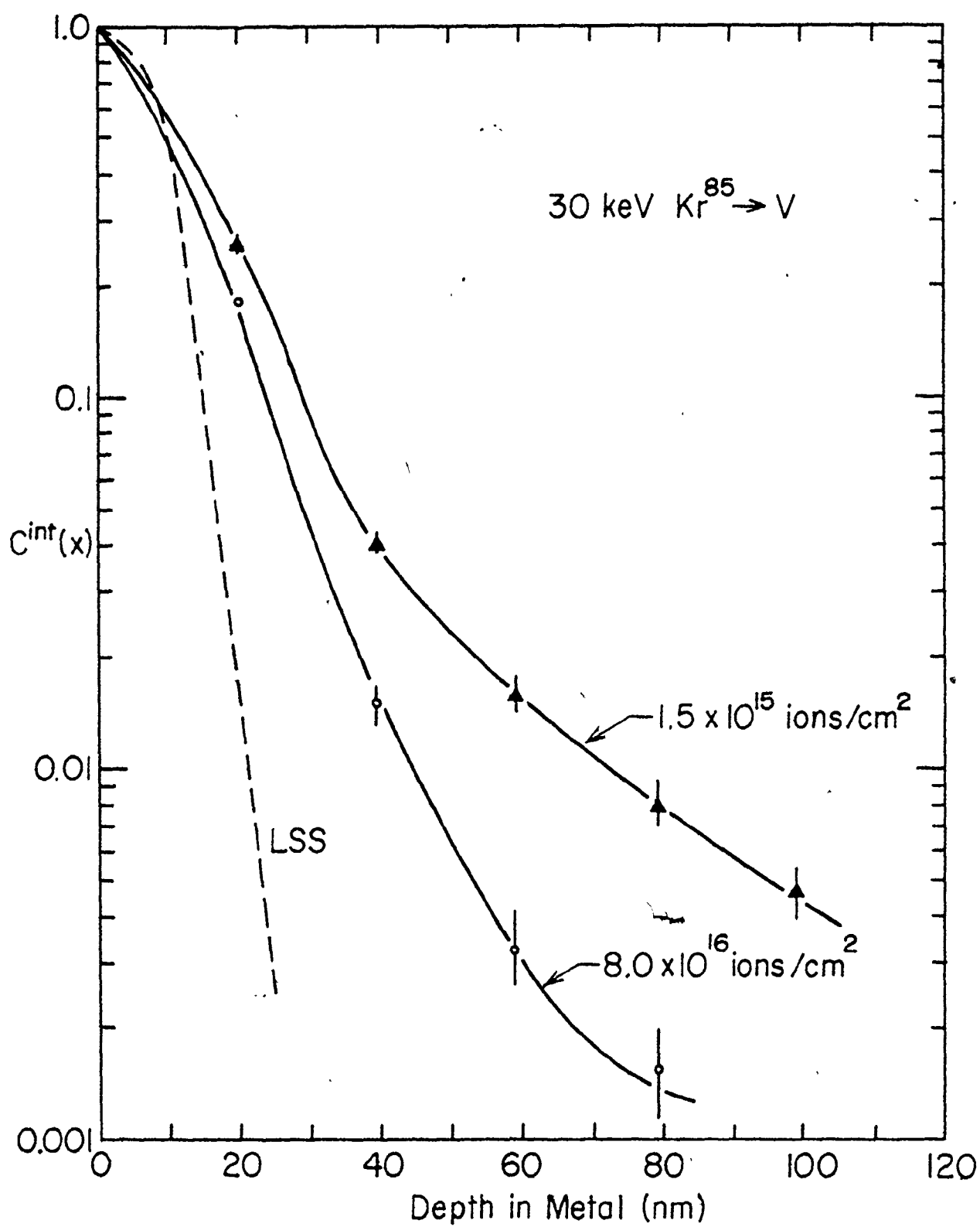


Figure 5.1. Experimental (solid) profiles of 30 keV Kr in V compared to the predicted distribution.

by diluting the krypton with its radioactive isotope Kr^{85} and subsequently counting the remaining activity in the sample. The plots in Fig. 5.1 show the effect of crystallinity on the depth of penetration. Channels between low index strings and planes in the crystal provide unobstructed paths for the ions to travel down giving rise to large penetration depths. As the dose is increased, however, the distributions tend towards the calculated amorphous profile (eq. 3.5) since the implanted Kr itself is beginning to block the channels.

An alternative explanation may also contribute to the greater penetration with respect to eq. 3.5. The Kr may in part be interstitials and therefore have very high mobilities even at room temperature. Thus, the room temperature profile may be deepened by anomalous Kr diffusion. In any case the initial room temperature distribution will be approximated as exponential, for purposes of the diffusion equation.

The isothermal annealing properties of such a profile are shown in Fig. 5.2. Here samples irradiated at room temperature were annealed for one hour under a vacuum of approximately 10^{-6} torr. As shown the profiles tend to be biased towards the surface with subsequent Kr volatilization.

Ideally these experimental distributions can be analyzed in terms of Ficks Diffusion equation

$$\frac{\partial}{\partial t} C(x,t) = D \frac{\partial^2}{\partial x^2} C(x,t) \quad (5.1)$$

with the initial condition

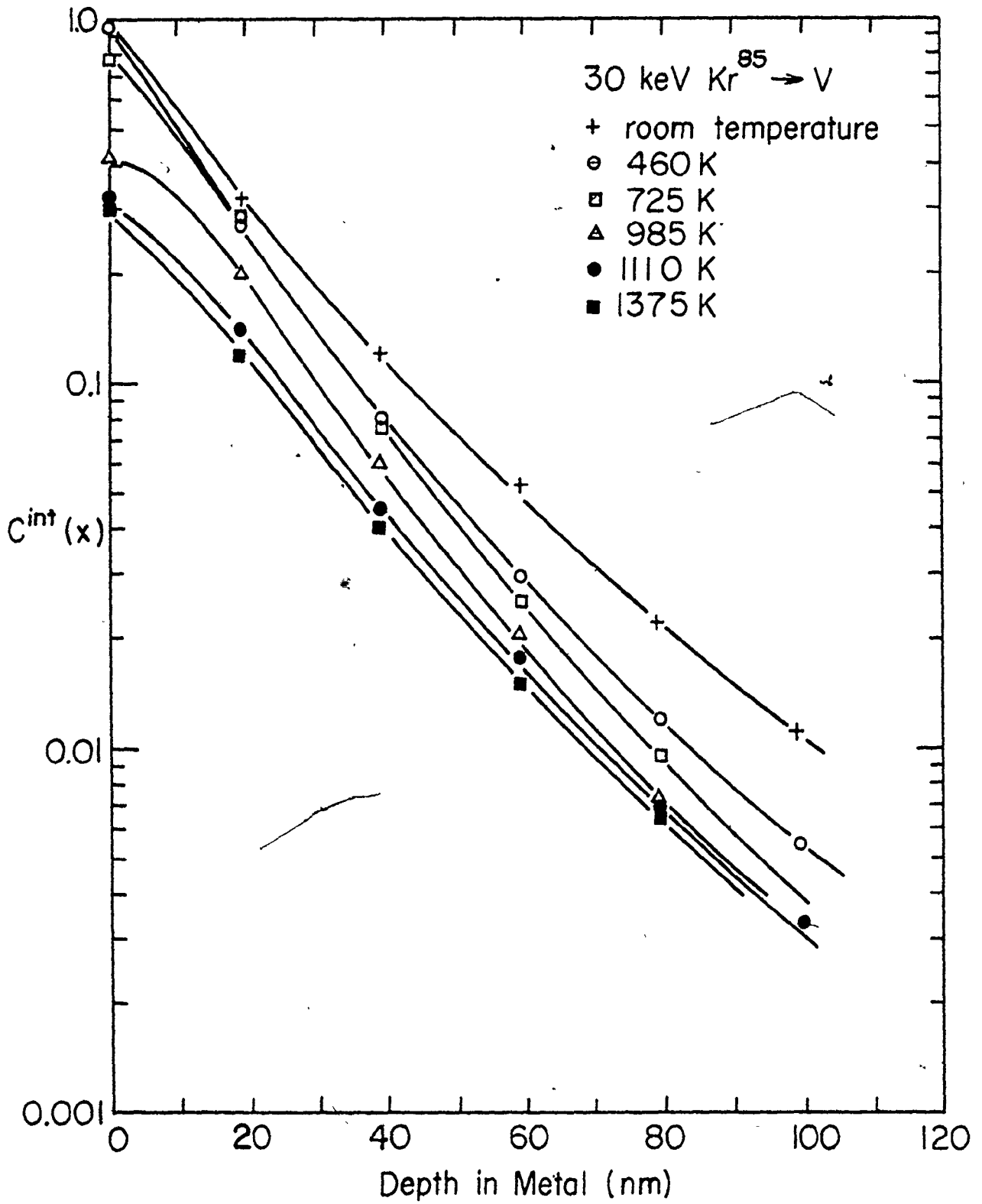


Figure 5.2. Integral diffusion profiles of Kr in V. Anneals were for 60 min.

$$C(x,0) = C_0 \exp(-x/R) \quad (5.2a)$$

and boundary condition

$$C(0,t) = C(\infty,t) = 0. \quad (5.2b)$$

The diffusion constant has been taken to be independent of any radiation damage effects. The solution to eq. (5.1) is

$$C^{int}(x,t) = \frac{1}{2} \exp(Dt/R^2) \{ \exp(-x/R) \operatorname{erfc}[(Dt/R^2)^{1/2} - x(4Dt)^{-1/2}] + \exp(x/R) \operatorname{erfc}[(Dt/R^2)^{1/2} + x(4Dt)^{-1/2}] \} \quad (5.3)$$

and is plotted in Fig. 5.3 for several values of the variable $0.240 Dt/R_m^2$. In eq. (5.3), R is the mean range and $R_m = R_m^2$ is the median or 50% range. The calculated profiles in Fig. 5.3 are seen to "rotate", i.e., diffusion occurs (as it must when the behavior is ideal) both inwards and outwards. Comparison with the measured distribution in Fig. 5.2 shows a dramatic absence of "rotation" and, in particular, a biased movement towards the surface. This forces us to the conclusion that the diffusion is significantly non-ideal. Perhaps the damage introduced by the accelerated ion, in the form of point defects or dislocation loops, is the cause of such surface directed motion.

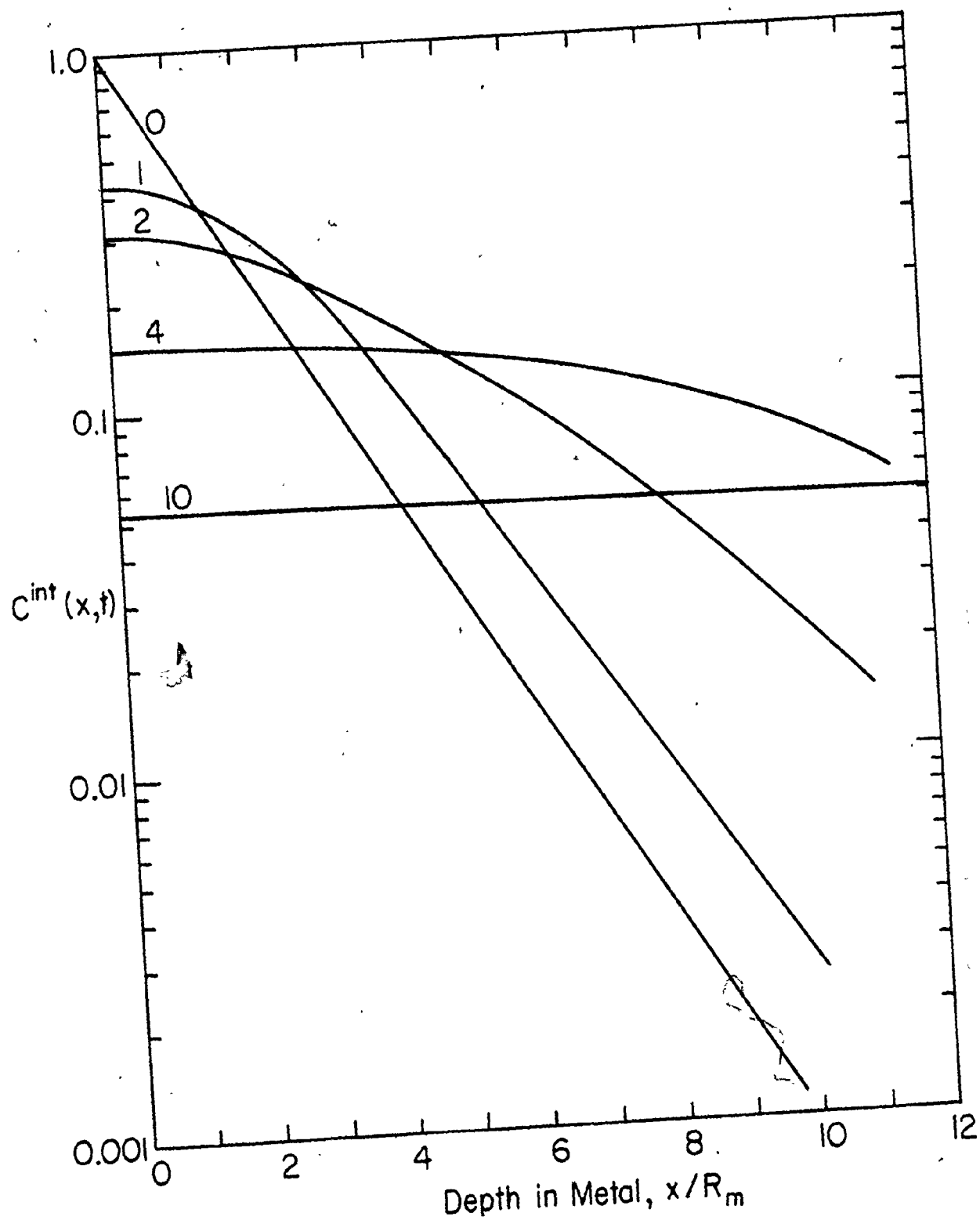


Figure 5.3. Solution to the diffusion equation. Curves are for $\frac{0.24 Dt}{R^2} = 0, 1, 2, 4, 10$.

To test such an hypothesis, 75% of the outer damaged zone was removed by a microsectioning prior to depth distribution analysis the results being shown in Fig. 5.4. The effect of this removal of the damaged zone, is to return the diffusion profile in part back to that predicted for an undamaged surface layer.

Of further interest concerning the release of implanted Kr is the cumulative release behavior at the surface.

5.3 CUMULATIVE RELEASE

By employing a dilute radioactive Kr mixture for implantation, the fractional cumulative release behavior is easily obtained by simply counting the activity remaining in the irradiated sample after each anneal. The fraction released at the surface, $x=0$ follows from eq. 5.3 as

$$\begin{aligned} F &= 1 - C^{\text{int.}}(0,t) \\ &= 1 - \exp(Dt/\bar{R}^2) \operatorname{erfc}\{(Dt/\bar{R}^2)^{1/2}\}. \end{aligned} \quad (5.4)$$

Figure 5.5 shows the observed release behavior of Kr in V both with damage retained and with damage removed. The rather narrow release curve for the damaged specimen suggests that release is being governed by a thermally activated desorption of the gas-atom from defect locations, while the broader temperature range for the damage-free specimen suggests a more normal volume diffusion behavior. At temperatures below approximately 470°C, the assumed gas-atom-defect interactions lead to much less Kr mobility than in the damage removed case.

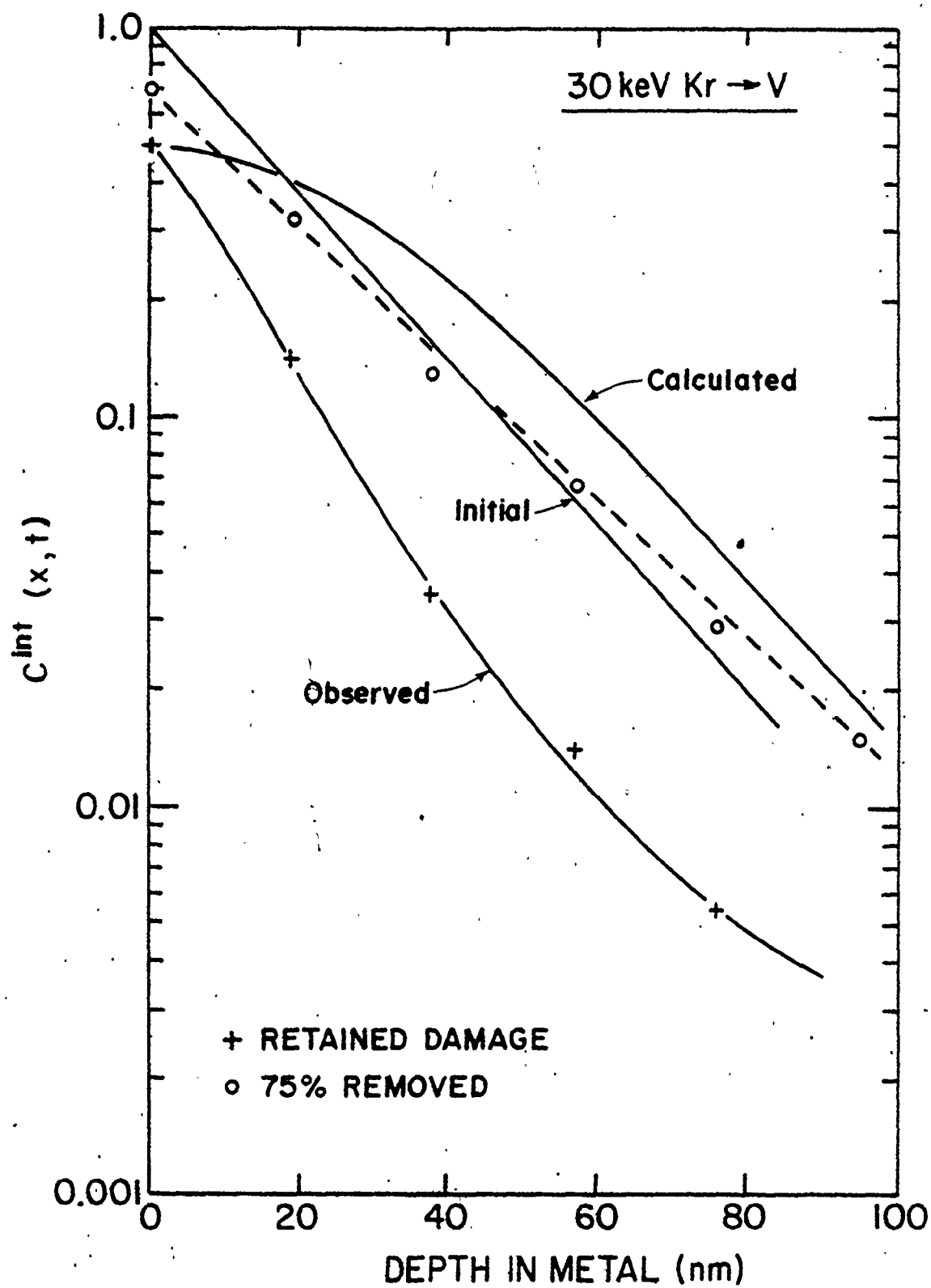


Figure 5.4. The effect of damage removal on the diffusion behavior of Kr in V. Annealed at 900 K for 60 min.

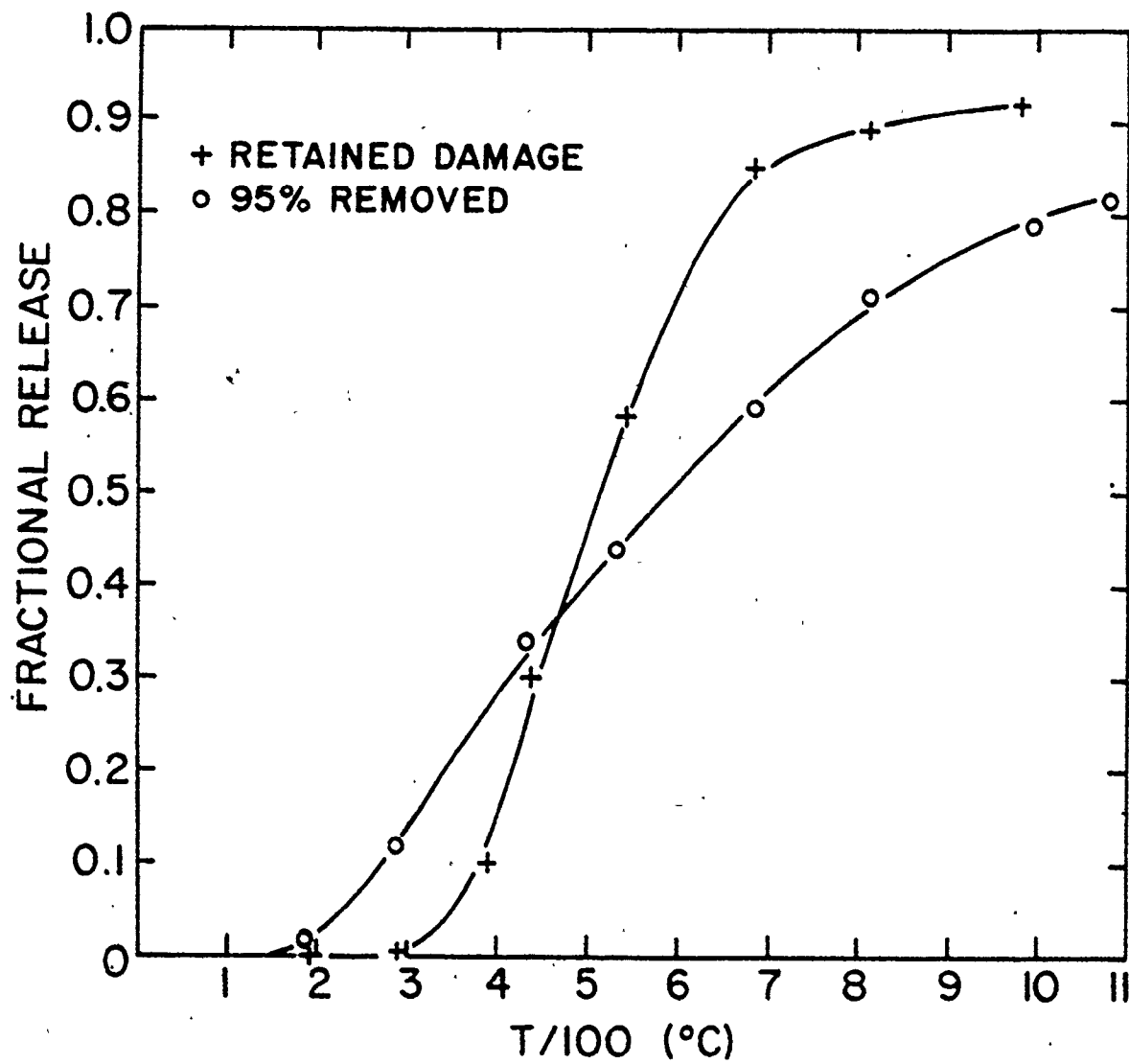


Figure 5.5. The effect of damage removal on the cumulative release of implanted Kr.

However, the release behavior is even more complicated by the fact that the temperature range of release in the damaged condition is about three times wider than it should be, according to a model developed by Redhead (7). In the damage-free condition the temperature ranges are still approximately two times wider than according to eq. 5.4.

As an aside, it is of interest to note that short circuit paths, for example dislocation loops do not become active high diffusion paths until the Kr is "detrapped" from its defect cluster. This defect core is in all likelihood a vacancy rich site since, as demonstrated by Gettings et. al. (2), using channeling techniques, the fraction of Kr sitting substitutionally in vanadium is approximately zero.

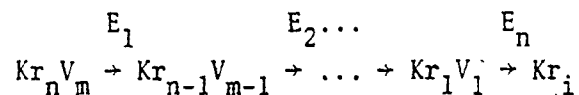
Though the cumulative release behavior can give information over a wide range of temperatures, specific details of the desorption process are lost. These details are, however, well resolved using a linear heating schedule and monitoring the release phenomenon as a function of temperature.

In particular, specimens were heated according to $T = T_0 + \beta t$ where T_0 is the initial temperature, β is the heating rate and t , the time. Observations were made on dF/dT , the release rate, and should reveal a single peak where $F(T)$ has its maximum slope. Kornelson (3) has used this technique extensively in detrapping studies of He from various targets. He has shown that at the peak temperature for a process involving detrapping rather than diffusion one has the following relation

$$T_m^2 \exp(-E/kT_m) = \beta E / \nu k, \quad (5.5)$$

from which the activation energy for detrapping, E can be deduced. In eq. 5.5, ν is a jump frequency, k is Boltzmann's constant and T_m the temperature of maximum release rate. Figure 5.6 plots the relation in eq. 5.5 for two values of the jump frequency, ν .

For example, Fig. 5.7, shows the release spectrum of Kr from Al, where the desorption of the inert gas takes place only upon the breakdown of the solid surface oxide. Figure 5.8 shows the spectra as from vanadium and we find the significant result that several release processes are occurring. Such multiplicity can be explained in terms of gas-atom-defect reactions of the form



where the notation refers to n Kr atoms in a cluster of m vacancies. The release of a trapped Kr atom is assumed to be by way of a thermally activated process of activation energy, E . The final result is proposed to be a Kr interstitial, Kr_i , which would be expected to have the lowest migration energy. Employing Fig. 5.6, activation energies can be deduced for these peaks and are listed in Table 5.1 along with results for other metals and literature data on some activation energies. It should be pointed out that the peak labelled II for V could be interpreted, on the basis of its temperature width as the normal volume diffusion of Kr in V.

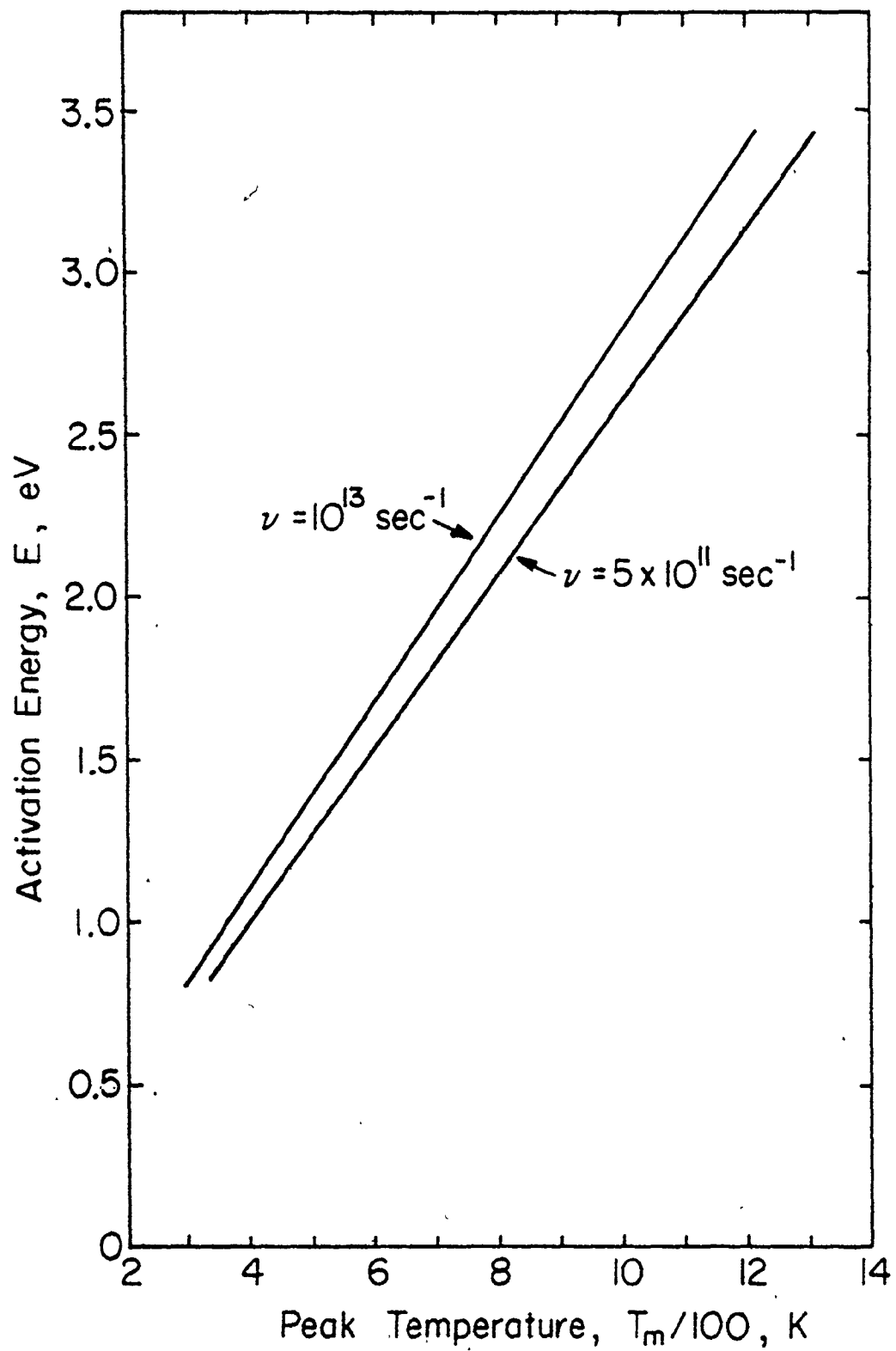


Figure 5.6. Activation energy versus temperature at which maximum release rate occurs. Two values of the jump frequency, ν , are given.

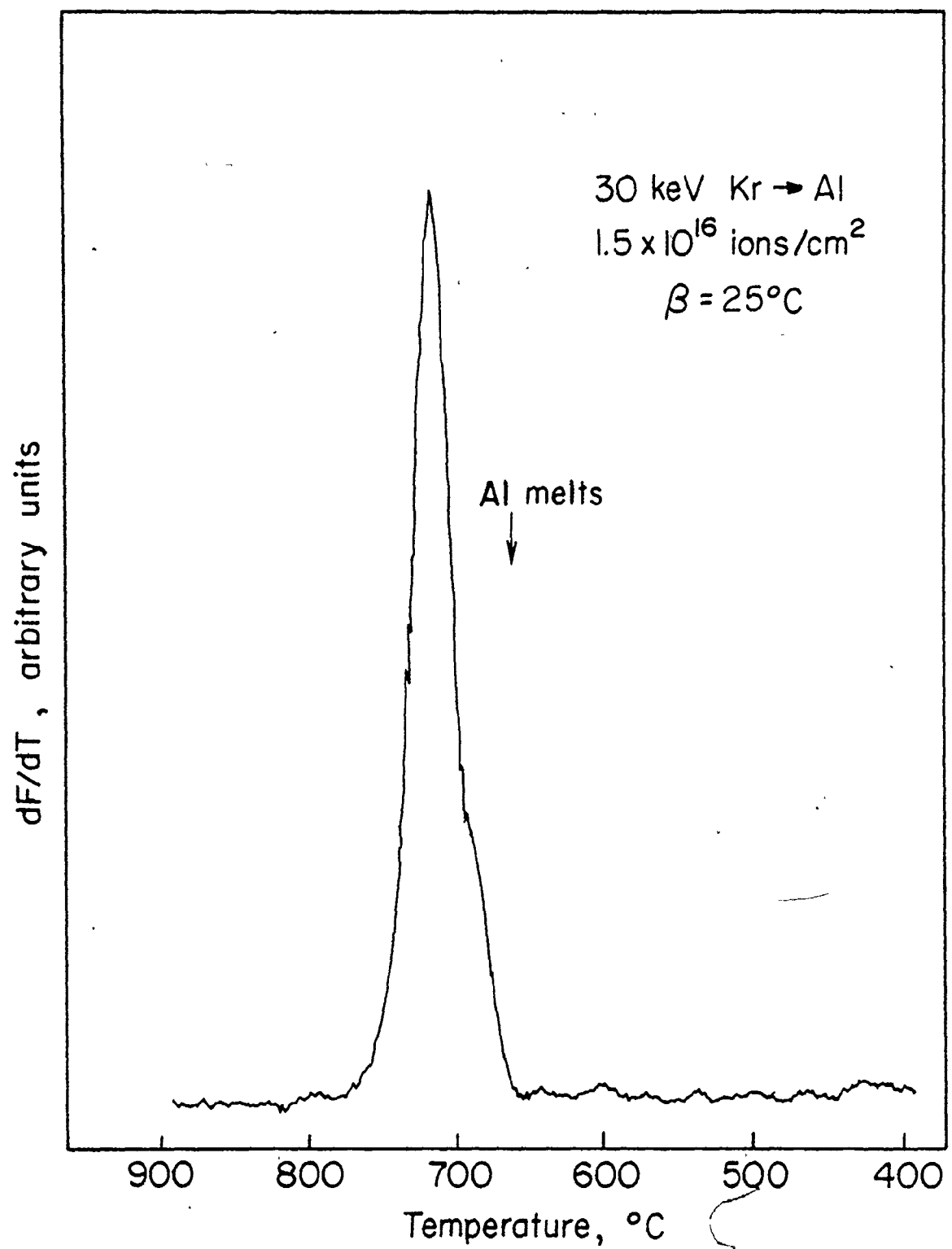


Figure 5.7. Release rate spectrum from Al.

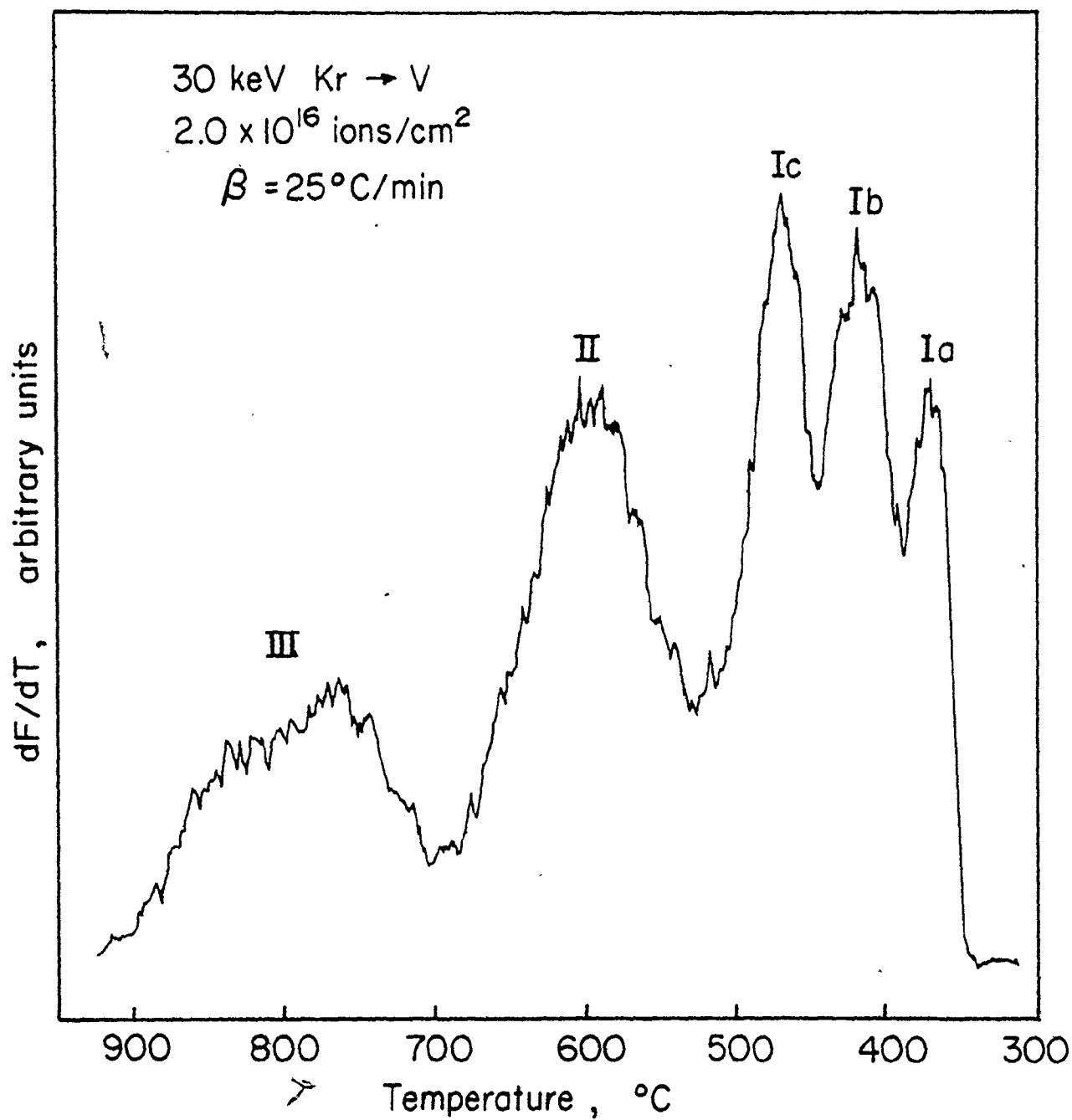


Figure 5.8. Release rate spectrum from V.

Table 5.1. Activation energy data for pure metals where E is energy for Kr gas-atom release E_m^V is migration energy of a single vacancy and E_{sd} , the energy for self diffusion.

Metal	Peak Number	T_m , °C	E, eV	E_m^V , eV Ref.	E_{sd} , eV From (4)
Cu	I	580	2.4	1.08 (6)	2.17
	II	620	2.5		
	III	810	3.1		
Zr	I	700	2.7	0.8 (5)	α Zr, 1.73, β Zr, 1.26
Al	I	715	2.8	0.63 (6)	1.48
V	Ia	370	1.8		3.33
	Ib	420	1.9		
	Ic	470	2.1		
	II	590	2.4		
	III	770	2.9		
Zn	I	280	1.6		0.99
	II	850	3.2		
Ti	I	600	2.5		α Ti, 1.27, β Ti, 1.47
Nb	I	830	3.1	1.9 (5)	4.52
Mo	I	650	2.6	1.26 (5)	4.58
Au	I	1005	3.6	0.83 (6)	1.89

Again to test the effect of heavy ion damage an irradiated specimen was vacuum annealed to 760°C prior to a release rate experiment. The results, as shown in Fig. 5.9, reveal presence of one defect type plus a peak at 550°C which we again interpret as due to normal volume diffusion.

We thus find that the diffusion behavior of implanted Kr in V is a complicated process involving up to five distinguishable components of which at least two persist after a preliminary annealing. It is therefore not surprising that the diffusion profiles of Fig. 5.2 and the cumulative release behavior of Fig. 5.5 have an excessively large temperature range. Even removing damaged surface layers fails to simplify the diffusion process.

5.4 CONCLUSIONS

Ion implantation of Kr in V yielded a distribution which exhibited a large penetration due in principle, to contributions of channeling effects and the mobility of interstitials. Upon subsequent vacuum annealing of the as irradiated specimens, the concentration profiles exhibited a clearly biased motion towards the surface. Removal of the damaged zone by anodic sectioning returns the diffusion behavior, in part, to normal.

Thermal release experiments, reveal a complicated defect structure, conceivably Kr atoms trapped at vacancy clusters which subsequently desorb with characteristic activation energies. By prior annealing, the damage is, in part, removed and the release behavior is somewhat returned to an ideal behavior.

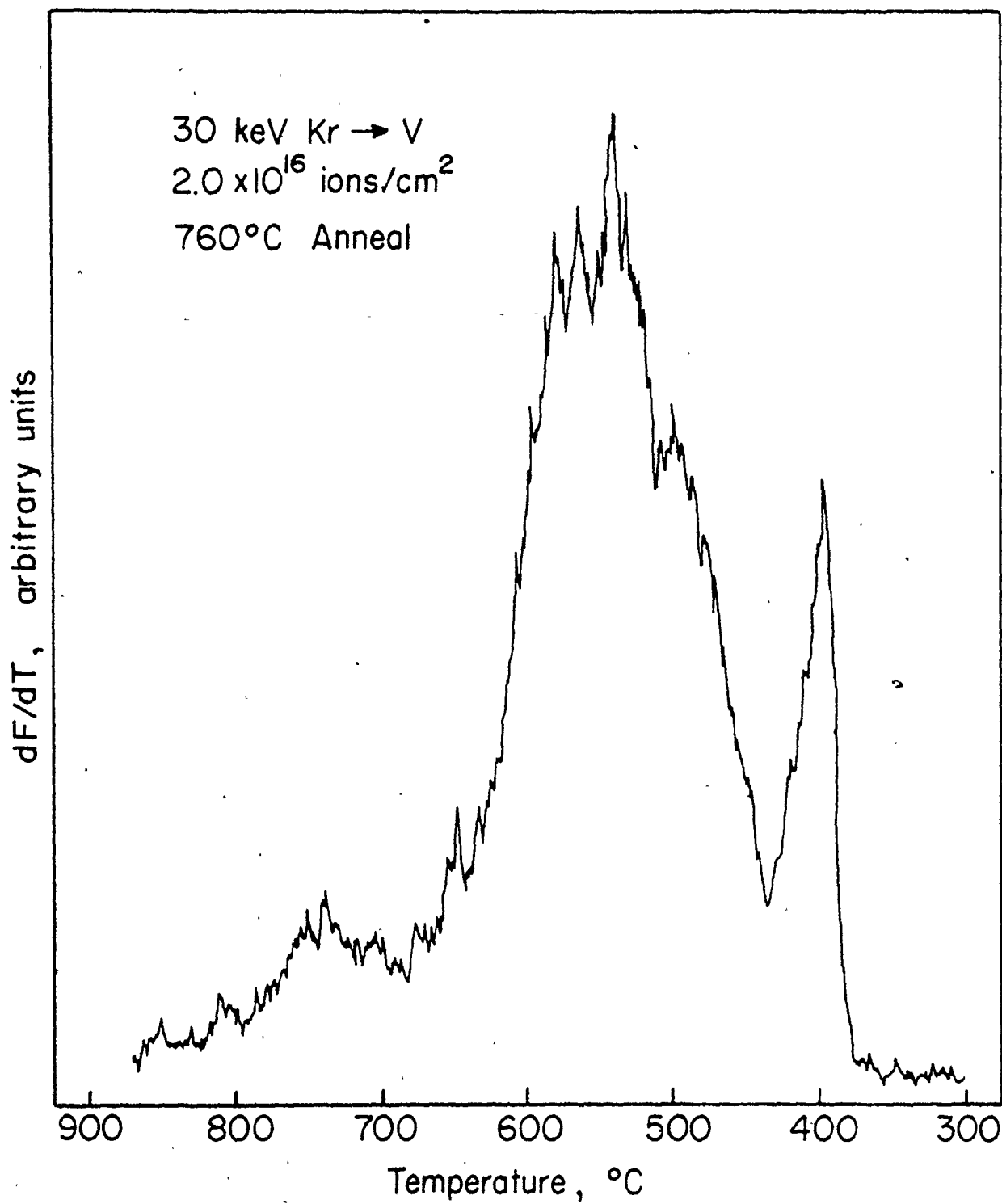


Figure 5.9. Effect of prior annealing on the release rate spectrum.

Further, the results show a definite complexity in terms of analysis which arise in particle-surface studies "in the solid" while the "face and isolated" species in the vacuum lend to a much simpler form of investigation.

REFERENCES TO CHAPTER 5

1. M.R. Arora and R. Kelly, J. Elec. Soc., 120 (1973) 128.
2. M. Gettings, O. Meyer and G. Linker, Rad. Effects, 21 (1974) 51.
3. E. Kornelson, Can. J. of Physics, 48 (1970) 2812.
4. J. Askill, Tracer Diffusion Data for Metals, Alloys and Simple Oxides, Plenum Press, 1970.
5. L.C. Feldman and J.W. Rodgers, J. Appl. Phys., 41 (1970) 3776.
6. K. Schmid, Rad. Effects, 17 (1973) 201.
7. P.A. Redhead, Vacuum, 12 (1962) 203.

CHAPTER 6

OVERVIEW

This work has attempted to investigate high energy sputtered particles as a result of inert gas ion impact. For normally incident ions, secondary particles, namely target atoms, ions and molecules are ejected from the solid surface in ground states or in varying degrees of excitation. Provided these sputtered particles survive non-radiative transitions, for example Auger or tunneling transitions, there is a finite probability that they will decay back to their ground state by emitting a photon. These secondary photons have been analyzed in terms of their wavelengths, intensities and spatial extents in front of the target surface.

A model has been developed which describes the intensity distribution of light as a function of perpendicular distance from the target which can give information about the velocity of the sputtered excited species. This model is based on proposing a threshold type behavior for excitation. In particular, four cases for this probability were investigated leading to estimates of the threshold kinetic energy, E^* . The model also takes into account the energy distribution of sputtered atoms along with the assumption of an isotropic angular distribution. By experimentally determining the light intensity distribution a linearization can be constructed whose slope gives the postulated threshold energy, E^* .

The experimentally determined distributions varied in their overall extension from the surface depending upon the values of the decay rate constant, γ_i , of that particular transition. For example, one finds that for $\gamma_i > 0.4 \times 10^8 \text{ s}^{-1}$ the decay occurs mainly within 1.5 mm of the target surface while for γ_i in the range $0.02 - 0.2 \times 10^8 \text{ s}^{-1}$ it occurs 3-10 mm from the target.

From the raw data, plots of the variable z vs distance are constructed with the result that sputtered energies of excited atoms and ions are in the region $10^1 - 10^3 \text{ eV}$ for 12 keV Kr^+ bombardments. These relatively high energies, compared with those from the cascade sputtering model or the thermal sputtering model, indicate that secondary photon emission results from collisions involving large energy transfers as would be the case for surface recoils. This argument is further substantiated by the fact that the Rydberg radii of excited atoms is much greater than the interatomic separation. This means that the excited species if at all created within the solid could not survive an excursion to the surface.

A comparison to the kinetic energies of secondary ions shows that excited atom velocities are much higher.

Given that the yield of secondary photons follows an expression of the form $(2E^* E_b + E_b)/(E^* + E_b)^2$ excited atoms/sputtered atom, then yields of the order 10^{-2} to 10^{-1} are obtained which are in agreement with the absolute yields measured by other workers.

These basic results indicate that the origins of secondary photons and secondary ions is different. In particular that excited species are created at the outer most surface as recoils while secondary ions

can be created in a typical collision cascade. However, the yield response to the presence of oxygen enhances both the secondary photon and secondary ion yields.

Also, the collisional mechanism for excitation follows as being one of a potential energy curve crossing nature. This mechanism has the feature of a threshold phenomena.

These conclusions lead us to believe that excitation in sputtered atoms is the result of high energy sputtered recoils.

To this end, a model has been developed which gives the yield and mean energy per sputtered recoil. The yield of sputtered recoils is in the range 0.02 to 0.26 recoils/incident ion with energies in the region 10^2 - 10^3 eV. This recoil yield is an order of magnitude greater than the high energy yield from the cascade and, therefore, should provide a larger source of secondary photons. In addition, this yield should be considered as additive to the cascade yield.

As a corollary to recoil sputtering, solutions for recoil implantation distributions have been developed. These profiles are characterized by a very shallow depth of penetration and a non-peaked distribution. Again, the yield of recoil implanted atoms has been calculated and by comparing this to the sputtered yield it has been shown that a compound target is enriched in the heavier component when irradiated. However, it must be emphasized that such a preferential effect may have many origins, among them: surface binding energy effects and diffusional effects.

Finally, we have shown that the release of the primary ion from

the solid, subject to thermal annealing, is a very complicated process involving up to five distinct detrapping events. The release behavior can, to some extent be modified by removing the damage caused by the primary ion either through annealing or stripping the damaged zone off.